CRANFIELD UNIVERSITY

School of Aerospace, Transport and Manufacturing

M.Sc. Thesis

Academic Year: 2014-2015

Bernat Font Garcia

High-Order Shock-Capturing Schemes for Micro Shock Tubes

Supervisor(s):

Dr. László Könözsy

Except where acknowledged in the customary manner, the material presented in this thesis is, to the best of my knowledge, original and has not been submitted in whole or part for a degree in any university.

Bernat Font Garcia

Abstract

Microfluidics has recently become a popular fluid dynamics branch [1]. Technology advances have facilitated the manufacturing of micro-scale devices and, because of this, a parallel interest from the fluid dynamics modelling standpoint has risen. The present thesis investigates the shock tube test case for the millimetre and micrometre scales. At these length scales, non-continuum effects and wall effects dominate the flow physics associated to the shock wave propagation phenomena.

The Minitube2D FORTRAN in-house code has been further developed to solve the fully compressible Navier-Stokes (N-S) equations in different coordinate systems. The advective fluxes are computed using (very) high-order shock wave-capturing schemes together with approximate Riemann solvers under the Godunov-type methods umbrella with a cell-centred FVM approach. The viscous fluxes are computed using a forwards-backwards FDM discretisation. Different high-order Runge-Kutta (RK) time integration methods are considered as well. The Maxwell's slip and the temperature jump boundary conditions have been implemented to account for the rarefaction effects present in small-scale problems. The performance of the MUSCL2 scheme and the WENO5, MPWENO7, MPWENO9 and MPWENO11 schemes is investigated for the Sod shock tube (inviscid) test case. It is found that WENO schemes present a tiny oscillatory behaviour as the order increases even though they fulfil the TVD properties. However, the use of TVD RK methods together with very high-order WENO schemes provided very accurate profiles as well as a reduction of the oscillatory behaviour close to discontinuities. Experimental results from E. P. Muntz *et al.* [2] are used to validate the 1D N-S equations. A correct propagation and dissipation of the shock wave can be observed. The 2D N-S equations for the Cartesian and axisymmetric coordinate system are validated with numerical data from D. E. Zeitoun *et al.* [3] and A. R. Kumar *et al.* [4] respectively. For Zeitoun's case, a very accurate agreement of different profiles is shown. The use of the slip and the temperature jump boundary conditions proves the applicability of continuum approaches (N-S) for slip flows. Some flows features are also correctly captured in the transitional regime using kinetic models as reference data. Besides, a decoupled temperature transport equation is solved showing a good agreement with the temperature field provided by the energy and the state equations. Thus, the correct implementation of a scalar transport equation introduced to the equations system is validated. For Kumar's case, a similar temperature profile is obtained along the symmetry axis, even though an offset is appreciated. The turbulence model used by Kumar might introduce additional numerical dissipation resulting into a more attenuated distribution. Finally, scale effects are investigated using Zeitoun's set-up as the baseline case. The influence of the Knudsen number is studied by reducing the initial pressures of the shock tube and the height of the channel. It is found that both actions yield to a severe attenuation of shock wave propagation distance. This decay is more severe under the no-slip boundary condition with respect to the Maxwell's slip one. The influence of the initial pressure ratio is studied as well. As expected, high pressure ratios generate faster shock waves. Hence, the shock propagation attenuation (eventually becoming a compression wave) is more important for low pressure ratios.

Acknowledgements

Firstly I would like to express my most sincere gratitude to my supervisor, Dr. László Könözsy. His support and passionate dedication to science have encouraged me, not only during the thesis, but the whole year. Additionally, I thank him for his guidance with respect to my future in academia.

I am also truly grateful to Prof. Carlos-David Pérez-Segarra for letting me discover the beauty of computational fluid dynamics during his amazing lectures at the Universitat Politècnica de Catalunya (UPC). I would also like to thank him for his patience and support with regard to my PhD applications.

I would like to thank my friends in Cranfield; Èric, Neys, Pietro and Arpit for making this year an unforgettable one. In the long distance, Oriol, Sergi, Isaac, Marc, Albert and Laura have always showed me their unconditional support, for which I am sincerely grateful.

My parents, Àngel Font and Gemma Garcia, and my sister, Marta Font, have been my greatest source of motivation and they have taught me that nothing comes without hard work and sacrifice. Because of this and their overwhelming love, I would like to dedicate this Master's thesis to my family and express to them my deepest gratitude.

Bernat Font Garcia

Contents

List of Figures

List of Tables

Nomenclature

Symbol	**Unit**	**Description**
a	m/s	Speed of sound
$\mathbf{B}$	–	Vector of extra terms vector for the axisymmetric formulation
C_1	–	Sutherland’s constant
c_p	J/(kgK)	Specific heat capacity at constant pressure
c_v	J/(kgK)	Specific heat capacity at constant volume
D	m	Diameter of the shock tube
E	kg/(ms^2)	Total energy per unit volume
e	m^2/s^2	Specific internal energy
$\mathbf{f}$	m/s^2	Mass forces per unit volume vector
$\mathbf{F}_a$	–	Advective flux in the x direction
$\mathbf{F}_v$	–	Viscous flux in the x direction
$\mathbf{G}_a$	–	Advective flux in the y direction
$\mathbf{G}_v$	–	Viscous flux in the y direction
$\mathbf{H}_a$	–	Advective flux in the z direction
$\mathbf{H}_v$	–	Viscous flux in the z direction
k	m^2/s^2	Specific kinetic energy
$\mathbf{L}$	–	Spatial operator
M	–	Mach number
M_s	–	Shock wave Mach number
M_{th}	–	Theoretical Mach number
p	Pa	Pressure field
Pr	–	Prandtl number
R	J/(kgK)	Specific gas constant
Re	–	Reynolds number
$\mathbf{S}$	–	Source terms
S	K	Sutherland’s temperature
$S^{\pm}$	m/s	Wave speed
$\underline{\underline{S}}$	m/s^2	Symmetric tensor

T	–	Temperature field
T_0	K	Sutherland's reference temperature
$\mathbf{U}$	–	Vector of conservative variables
t	s	Time
$\mathbf{u}$	m/s	Velocity field
u, v, w	m/s	Velocity components
x, y, z	m	Cartesian coordinates
x_0	m	Diaphragm position
x_s	m	Shock position

α	m^2/s	Thermal diffusivity
α_{sl}	–	Runge-Kutta non-negative coefficient
β	–	Duff boundary layer parameter
β_{sl}	–	Runge-Kutta non-negative coefficient
γ	–	Ratio of specific heats
Δ_i	–	Slope of the MUSCL reconstruction procedure
$\overline{\Delta}_i$	–	Limited slope of the MUSCL reconstruction procedure
Δt	s	Time step
Δx	m	Horizontal grid spacing
Δy	m	Vertical grid spacing
Δz	m	Lateral grid spacing
ζ	s	Pseudo-time
ϑ	K	Temperature field of the temperature transport equation
κ	W/(mK)	Thermal conductivity
λ	m	Mean free path
μ	kg/(ms)	Dynamic viscosity
μ_0	kg/(ms)	Sutherland's reference dynamic viscosity
ξ_i	–	Limiter function
ρ	kg/m^3	Fluid density
$\underline{\underline{\sigma}}$	Pa	Stress tensor
σ_v	–	Tangential momentum accommodation coefficient
σ_t	–	Tangential energy accommodation coefficient
$\underline{\underline{\tau}}$	Pa	Viscous stress tensor
ϕ_i	–	Arbitrary discretised quantity
ψ	–	Scalar quantity
ω	–	Wind coefficient to select a certain scheme

Abbreviations

BC	Boundary Condition
BGKS	Bhatnagar-Gross-Krook-Shakhov
CFD	Computational Fluid Dynamics
CFL	Courant–Friedrichs–Lewy number
CS	Contact Surface
DSMC	Direct Simulation Monte Carlo
ENO	Essentially Non-Oscillatory
EW	Expansion Wave
FCT	Flux-Corrected Transport
FDM	Finite Difference Method
FVM	Finite Volume Method
IVP	Initial Value Problem
MD	Molecular Dynamics
MEMS	Micro-electro-mechanical Systems
MFP	Mean Free Path
MUSCL	Monotonic Upstream-centred Scheme for Conservation Laws
N-S	Navier-Stokes
ODE	Ordinary Differential Equation
PDE	Partial Differential Equation
RANS	Reynolds-averaged Navier-Stokes
RK	Runge-Kutta
RP	Riemann Problem
SW	Shock Wave
TMAC	Tangential Momentum Accommodation Coefficient
TV	Total Variation
TVD	Total Variation Diminishing
TVNI	Total Variation Non-Increasing
UDF	User Defined Function
WENO	Weighted Essentially Non-Oscillatory

Chapter 1

Introduction

Microfluidics has recently become a popular fluid dynamics branch [1]. Technology advances have facilitated the manufacturing of micro-scale devices and, because of this, a parallel interest from the fluid dynamics modelling standpoint has risen. Micro-electro-mechanical systems (MEMS) is the common name used to refer to micro-scale devices. The interest of the present work is focused on MEMS involving fluid flows. These can be found in many different fields from industrial to medical applications. Micropumps, microducts, microtubes, microchannels, microvavles, micronozzles, microturbines, microfluidic sensors, microengines and microfilters are some examples of MEMS associated to the flow of liquids and gases [10, 11]. Practical applications of MEMS fluidic devices are the cooling of integrated circuits, microflows control, drug delivery for medical systems, ink jet printing, micro-propulsion systems for aerospace industry among many others. The proper understanding of the physics latent in microfluidics is required for the design of such devices. Flow phenomena behind micro-scale fluid dynamics is notably more complex than in macro-scales. As described by G. Karniadakis *et al.* [5], the major difference between microfluidics and macrofluidics can be decomposed into

- Non-continuum effects,
- Surface-dominated effects,
- Low Reynolds number effects,
- Multiscale and multiphysics effects,

where the non-continuum effects includes rarefaction, compressibility, viscous heat and thermal creeping effects.

The Knudsen number (Kn) is a dimensionless parameter that characterises the non-continuum effects present in a certain flow. Thus, it determines the applicability limit of continuum approaches in fluid dynamics. It is defined as the ratio between the mean free path (MFP, average distance that molecules travel between collisions) and the characteristic length of the system. It is written as

$$Kn = \frac{\lambda}{L}. \tag{1.1}$$

The Knudsen number can also be related to the Mach and the Reynolds number. Therefore, compressibility effects in micro-flows are generally coupled with rarefaction effects. Given the following relation

$$Kn = \frac{M}{Re}\sqrt{\frac{\pi\gamma}{2}}, \tag{1.2}$$

for high Knudsen number flows, the compressibility effects ($M > 0.2$) can only be neglected at very low Reynolds numbers. On the other hand, for low Knudsen number flows, the compressibility effects can be neglected within a large range of the Reynolds number.

In the literature are found several studies regarding the influence of the Knudsen number and the applicability limit of continuum approaches. The continuum hypothesis assumes that quantities of interest related to fluid mechanics (density, velocity, pressure and temperature) have a continuous variation from one point to another point of the flow. However, this assumption is only valid when microfluidic fluctuations can be averaged in a representative control volume, so the molecular discontinuities vanish from a macroscopic point of view. In micro-scales, the control volume is often too small to perform a fair average of the microfluidic fluctuations or too big to capture continuous gradients of the quantities of interest [12]. Additionally, the control volume must be in thermodynamic equilibrium, according to the continuum theory. To achieve the thermodynamic equilibrium, the inter-molecular collisions inside the representative control volume must be high enough [12]. In other words, the molecular MFP must be smaller than the characteristic length of the representative control volume, what is often not applicable in micro-scales thus refuting the continuum theory.

Outstanding experimental investigations were performed by E. B. Arkilic *et al.* [13] proving that the no-slip boundary condition at the wall used in continuum models breaks down for high Knudsen number flows. Figure 1.1 displays different types of flows classified in the entire Knudsen regime.

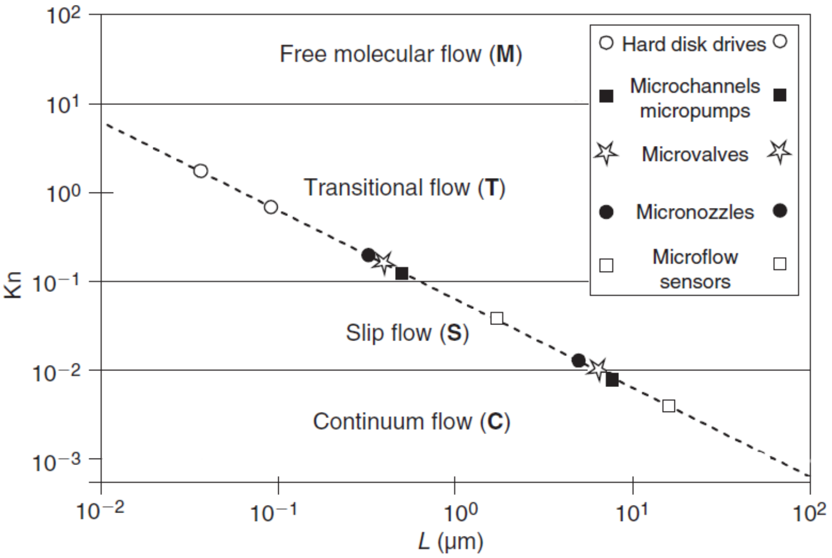

Figure 1.1: Knudsen regime. Flows are classified in function of the Knudsen number and the characteristic length. The location in the regime of different microfluidic devices is displayed [5].

For $Kn < 0.01$, the flow is considered to be in the continuum regime, where the non-continuum effects are negligible and for which the continuum hypothesis and the thermodynamic equilibrium are satisfied. For $0.01 > Kn > 0.1$, the flow is classified in the slip regime. Within this regime, the non-equilibrium effects must be taken into account near the walls. Usually the no-slip condition is not valid and the Maxwell's slip condition must be imposed at the walls. However, the continuum conservation equations are still valid. For $0.1 > Kn > 10$, the transitional regime takes place. Rarefaction effects become dominant at every point of the flow. Thus, the continuum hypothesis and the thermodynamic equilibrium assumption break down. The use of continuum approaches is no longer valid. Statistical models such as the Direct Simulation Monte Carlo (DSMC) are used for flows within this regime. Finally, flows within the $Kn > 10$ regime are classified as free molecular flows. Now, the number of molecules colliding with the wall is higher than the inter-molecular collisions and Molecular Dynamics (MD) models must be applied. Nevertheless, this is a general classification relying on empirical data that depends on the geometry of the problem. A wider explanation of the flow physics latent in microfluidics can be found in [5, 10, 12, 14].

1.1 Background and Motivation

A novel investigation within microfluidics is the propagation of shock waves in wall-bounded microflows. Miro-propulsion technology and micro-heat engines are some of the main micro-scale devices comprising shock waves. Shock waves generated with a micro shock tube are used there to accelerate the combustion process. Wall effects and rarefaction effects have a strong impact on the propagation of shock waves altering different flow features such as the shock wave strength and the shock wave propagation distance.

The present work intents to study the transport phenomena associated to the propagation of shock waves in micro-scales using a continuum approach. Therefore, the applicability limit of the continuum conservation equations is of main interest since most of the current microfluidic devices are comprised within the slip and the transitional regimes. For these regimes, specific boundary conditions are considered to take into account the rarefaction effects arising in the vicinities of the wall. Since statistical models used for transitional flows and the MD models used in the free molecular regime are computationally very expensive, there is an strong interest on exploiting the use of continuum equations.

From a numerical standpoint, continuum approaches related to shock wave-capturing schemes are also an active research field. The Godunov-type methods are a popular choice in this matter. These methods solve the conservation equations in the conservative form within a FVM framework. The Riemann Problem is solved at each cell interface thus maintaining the wave propagation physics. Under the Godunov-type methods umbrella, high-order schemes are used to achieve very accurate solutions, what is also a point of interest of the present work. The behaviour of different (very) high-order shock-capturing schemes together with approximate Riemann solvers and Runge-Kutta time discretisation methods is investigated.

A well-known shock wave-related test case is the shock tube. Several experimental studies have been performed for macro shock tubes. However, experimental works of micro shock tubes are much more complex to perform. As exposed in [15, 16], there are severe difficulties associated on selecting the diaphragm or valves required for micro shock tubes. Also, measurements are hard to perform at these scales. Therefore, computational fluid dynamics (CFD) has a very strong impact on this field.

1.2 Problem Statement

The main outcome of this Master's thesis is to investigate miniaturised shock tubes by solving the fully compressible Navier-Stokes (N-S) equations using very high-order shock wave-capturing schemes in the Godunov-type methods framework. The applicability of the N-S equations for small-scales is therefore assessed. The Minitube2D FORTRAN in-house code is further developed to perform such study.

The aims and objectives are summarised next,

- Solve the 1D Euler equations for the Sod shock tube problem using different shock-capturing schemes, approximate Riemann solvers and Runge-Kutta time integration methods.
- Solve the fully compressible 1D N-S equations and validate them using experimental data from E. P. Muntz *et al.* [2].
- Solve the fully compressible 2D Cartesian N-S equations and them validate using numerical data from D. E. Zeitoun *et al.* [3].
- Correctly predict flows under rarefied conditions near the wall (slip flows) using the N-S equations as a continuum approach and capture as many flow features as possible for transitional flows. To do so, the Maxwell's slip and the temperature jump boundary conditions are used at walls.
- Solve the fully compressible 2D axisymmetric N-S equations and validate them using numerical data from A. R. Kumar *et al.* [4].
- Investigate the small-scale effects by studying the influence of the Knudsen number and the pressure ratio on the shock wave propagation in small-scale shock tubes.

1.3 Structure of the M.Sc. Thesis

The thesis is divided into five chapters.

Chapter 1 presents an introduction to the present work explaining the background and the justification of the thesis.

Chapter 2 provides a literature survey of topics treated during the thesis. A general approach to the shock tube problem is presented. The Godunov-type methods are reviewed together with high-order shock wave-capturing schemes. The last section of the chapter describes the scale effects present in miniaturised shock tubes as reported by different authors.

Chapter 3 introduces the governing equations and the numerical methods to solve them.

Chapter 4 presents the results of the 1D Euler, 1D N-S, 2D Cartesian N-S and 2D axisymmetric N-S test cases. Experimental and numerical data is used to validate these simulations.

Chapter 5 summarises the present thesis reporting the main findings and achievements. Additionally, the future work is explained.

Chapter 2

Literature Review

2.1 The Shock Tube Problem

Isentropic flows are those for which the entropy is conserved during the process they are exposed to. These flows are characterised by smooth changes of the flow variables and, because of the second law of thermodynamics, the entropy is assumed to remain constant while performing such changes. In other words, the process is adiabatic and reversible, as described by R. Courant *et al.* [17, p. 18]. However, isentropic flows do not exist since, in the nature, flows always experience friction or thermal conduction, which are irreversible processes indeed. Therefore, a flow is usually considered isentropic when the entropy increment is negligible, *e.g.* the generation of sound waves or isentropic expansions. Under this assumption, the isentropic relations can be applied.

Fluids flowing at very low velocities compared to the velocity at which sound propagates through them can be considered incompressible. The sound velocity of a fluid is very important since it provide the velocity at which perturbations travel across the fluid. As the velocity of the flow increases getting closer to the sound velocity, compressibility effects have to be taken into account. If the velocity of the flow is further increased and the sound speed barrier is overcome, the flow becomes supersonic. Still at this regime a flow can perform processes with minimum entropy generation and thus be considered an isentropic flow. An example is the isentropic expansion of a supersonic flow. However, the flow can also experience processes that are not entropy-conserving and for which the isentropic relations break down. A classic example is a shock wave. A shock wave is a perturbation that travels faster than the speed of sound generating sharp discontinuities of the flow variables as it propagates. This happens because of the perturbation travelling faster than the wave that informs of its existence, which travels at the speed of sound. These sharp discontinuities (or sudden changes) of the flow variables yield to a non-isentropic process. One can consider a shock wave as a non-isentropic process since, even though there is no heat addition neither output work (thus the temperature and total enthalpy are conserved), there is a total pressure loss across the shock wave (the total pressure of the shocked flow is lower than the total pressure of the non-perturbed flow) [17, p. 116]. In fact, the energy is dissipated into heat and sound becoming an irreversible process. The Rankine-Hugoniot relations are used to describe shock waves. The fluid is compressed as the shock wave propagates and its analogous isentropic process is the Prandtl-Meyer compression.

There are many applications where shock waves have a critic role, from aerospace applications to medical devices, and the study of the shock waves propagation through a tube or a channel has always been a primordial shock wave problem. For the present work, the generation and propagation of shock waves in a tube is studied. This classic case study, also known as the shock tube problem, has been relevant for the investigation of shock waves for both experimental and numerical purposes in fluid dynamics since it allows one to generate repeatable and controlled shock waves [15]. From an historical point of view (see [18]), the first experimental study of a shock tube was developed by the French physicist P. Vieille in 1899 to demonstrate that shock waves generated by an explosion propagate in the same way as they do in a tube. Later on, these experiments were further investigated by K. Kobes and F. Hildebrand in order to improve air suction breaks on trains using shock waves. During the World War II, a big interest was also focused on shock tubes because of its relation to high-velocity wall-bounded gases such as chemical processes in combustors. More recently, experimental shock tube studies are performed in order to understand more complex phenomena, *e.g.* the interaction of shock waves and the boundary layer or the turbulence phenomena associated to high-Reynolds shock tubes.

From a mathematical standpoint, a shock tube can be treated as a Riemann Problem. The Riemann Problem (RP) is an Initial Value Problem (IVP) consisting of a discontinuity separating two different states (left L and right R) and its solution consists of finding the value at the interface between both states arising from the particular wave pattern generated, which is not unique. The described situation is exactly the mechanism used for generating shocks in a shock tube. Two different steady states of the flow are separated by a membrane (or diaphragm). After its sudden burst, a concrete wave pattern arises as a result of the initial pressure difference (usually defined as a pressure ratio). Particularly, for the case containing a high-pressure (and high-density) state at the left of the membrane and a low-pressure (and low-density) state at the right, an expansion wave (EW) is propagated to the left and a shock wave (SW) and a contact surface (CS) are propagated to the right [19], as shown in figure 2.1.

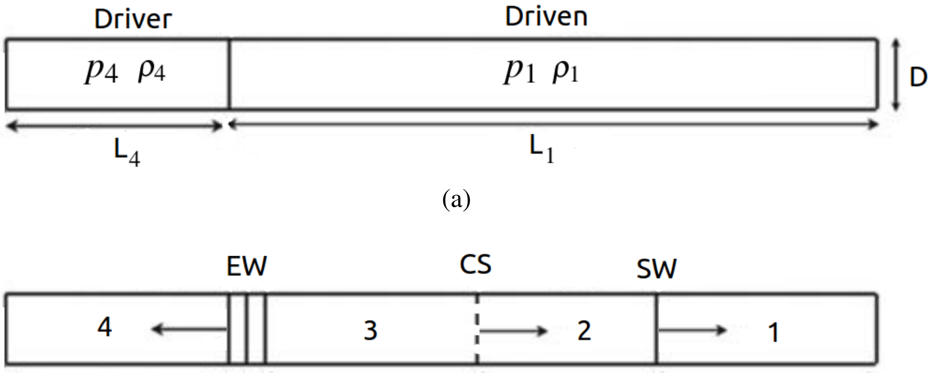

(a)

(b)

Figure 2.1: Schematic diagram of a shock tube. a) Initial states. b) Wave pattern developed after the rupture of the diaphragm.

The ideal shock tube theory predicts the required pressure ratio for a given shock wave Mach number without the presence of the viscous effects as given by the following relation

$$p_{41} = \frac{p_4}{p_1} = \left[1 + \frac{2\gamma_1}{\gamma_1+1}\left(M_s^2 - 1\right)\right]\left[1 - \frac{\gamma_4 - 1}{\gamma_1 + 1}\left(\frac{a_1}{a_4}\right)\left(M_s - \frac{1}{M_s}\right)\right]^{\frac{-2\gamma_4}{\gamma_4 - 1}}, \qquad (2.1)$$

where γ is the specific heats ratio, M_s is the shock wave Mach number and a is the speed of sound. Subscripts refer to the driver (4) or driven (1) sections of the shock tube. Eq. 2.1 can also be used for real macro shock tubes, where viscous dissipation effects play a minor role. However, this relation does not apply for small-scale shock tube where viscous effects cannot be neglected, as explained in Section 2.3.

G. A. Sod [20] investigated several finite difference numerical methods for the shock tube problem in 1978 involving the Godunov, Hyman, Glimm, Lax and Wendroff (two-step), MacCormack, upwind scheme and Rusanov methods (among others) proving that the Godunov's method and the Glimm's method provide the most accurate solutions for this test case. For the present work, a Godunov-type method is considered. The Navier-Stokes (N-S) equations in a conservative form can be used to model this case study since they allow discontinuous solutions (being shocks a suitable problem). Note that the non-conservative form of the N-S equations is only valid for smooth flows, hence inappropriate for shock waves treatment [6, p. 174]. As an easier case, one could use the Euler equations which are a simplification of the N-S able describe the motion of compressible fluids neglecting the viscous forces, the body forces and the heat transfer. Hopefully, an analytical solution exists for the 1D Euler equations in a shock tube. This fact is of main importance when developing computational methods for compressible flows.

2.2 Numerical Methods for Compressible Flows

S. K. Godunov [21] presented a conservative method in 1959 in order to solve the Euler equations which included the solution of the Initial Value Problem (IVP) for discontinuous initial conditions, the classic Riemann Problem (RP). Using a Finite Volume Method (FVM) and solving the exact RP at the interface between cells (thus computing the inter-cell flux), the Godunov's method provided accurate solutions of the Euler equations. The FVM ensure that transport properties are conserved locally, therefore it is a relevant tool for solving partial differential equations (PDEs) in the fluid dynamics field (*e.g.* parabolic, hyperbolic and elliptic PDEs). The main idea behind the Godunov's method is that the wave propagation physics are taken into account within the numerical method by solving the RP yielding to physically meaningful solutions.

The method developed by Godunov was only 1st-order accurate since an integral average in cell resulting from the solution of the local RP at each side of the cell yields to the well-known 1st-order upwind scheme. However, a higher accuracy is usually required and B. van Leer proposed an alternative to the piece-wise constant cell data presented by Godunov. By reconstructing the cell data with high-order schemes (*i.e.* piece-wise linear instead of piece-wise constant data), a more accurate solution can be achieved [6].

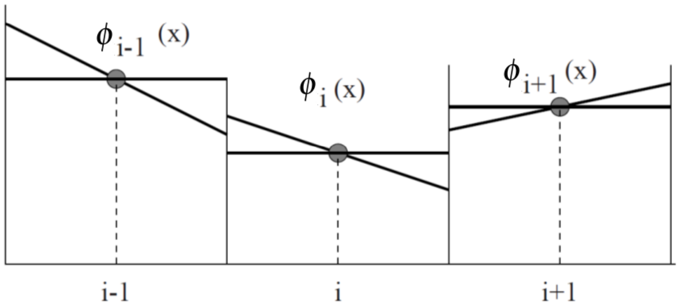

Figure 2.2: Piece-wise linear cell data reconstruction [6].

In fact, using specific high-order schemes for the reconstruction procedure aims to diminish the spurious oscillations that are generated near sharp discontinuities (as shock waves) while they provide high accuracy for the smooth parts of the solution, as stated by V. A. Titarev *et al.* in [22]. B. van Leer presented in series of five paper [23, 24, 25, 26, 27] a 2nd-order Godunov-type method based on a linear data reconstruction including monotonicity algorithms to ensure the stability of the scheme. From the Godunov theorem, it is known that a monotone numerical scheme can be at most 1st-order accurate. So, B. van Leer used the Monotonic Upstream-centred Scheme for Conservation Laws (MUSCL) developed by P. Colella and P. R. Woodward [28, 29] to construct a 2nd-order monotone

Godunov-type method, also known as MUSCL-type method. Nowadays, MUSCL-type methods are a wide-spread technique to deal with the Euler equations or the convective term of the N-S equations, and its accuracy is usually 2$^{\text{nd}}$-order or higher .

It is important to remark the *monotone* concept of the MUSLC-type method. As mentioned, shock waves are sharp changes of the flow variables thus presenting very high gradients. Because of the Godunov theorem, high-order schemes would generate spurious oscillations when exposed to shock waves, eventually yielding to an unstable computation. Hence, it is very important to include monotonicity algorithms when using high-order schemes. Previously to B. van Leer, D. L. Boris published a series of papers [30, 31, 32, 33] describing the Flux-Corrected Transport (FCT) methods which are based on a predictor-corrector procedure using a 1$^{\text{st}}$-order non-oscillatory scheme at the predictor step and a high-order scheme at the corrector step. Later on, A. Harten [34] presented the Total Variation Non-Increasing schemes (TVNI), or Total Variation Diminishing (TVD), by defining the Total Variation (TV) as a measurement of the oscillatory behaviour for a certain numerical scheme. A TVD scheme ensures a monotonic interpolation which is of main importance for the data reconstruction step in high-order Godunov-type methods. R. LeVeque *et al.* [35] proved that TVD schemes cannot be used for multi-dimensional purposes and, because of this, Harten developed again a high-order non-oscillatory scheme based on a monotonic interpolation, the Essentially Non-Oscillatory (ENO) scheme, which can be used for multi-dimensional problems. Basically, the idea behind the ENO scheme is to analyse different discrete stencils and to select the smoothest one. More recently, Weighted ENO schemes (WENO) have been popularised. They rely on a weighted (convex) mixture of the stencils considered by the ENO procedure yielding to high-order schemes for smooth regions of the solution and to the standard ENO scheme for sharp discontinuities [36]. Further details of high-resolution non-oscillatory schemes that have also been implemented under the Godunov-type method umbrella are described by B. van Leer in [37].

The exact solution of the RP was considered for the original Godunov's method. However, it has been stated by different authors that such solution involves unnecessary amount of information for most of the studied problems and that it is too expensive in computational terms. Hence, approximate solvers of the RP arose in order to overcome this issue [38]. Harten, Lax and van Leer [39] developed a well-known approximate Riemann solver called the HLL Riemann solver. Instead of considering all the possible wave patterns of the exact RP solution, a two-wave pattern models an approximate solution. These two waves separate the space-time domain into three different (and constant) states. Further investigation by E. F. Toro *et al.* [40] regarding the HLL yielded to another approximate Riemann solver denoted as HLLC (C stands for Contact) which recovers the contact and shear waves from the exact solution. These solvers are contained within the HLL-type Riemann solvers and present stability, robustness and efficiency [6], what makes them an attractive choice for solving the RP within the Godunov-type methods.

2.3 Small-Scale Shock Tubes

Over the last decades, several authors have extensively studied and discussed relevant phenomena related to small-scale fluid flows. An important part of this work has been recently compiled and further developed by G. Karniadakis [5] and S. G. Kandlikar [12]. However, the generation and propagation of shock waves within microfludics applications is a very novel branch which has already proved to be challenging for both experimental and mathematical approaches. Currently, we are aware of very few scientific groups working within this field. The main leading groups are located in Marseille (France); J. Giordano, J-D. Parisse, D. E. Zeitoun, and Quebec (Canada); G. Mirsheraki and M. Brouillette. Furthermore, other groups from Andong (Korea); A. R. Kumar, and Bangalore (India); S. Janardhanraj have also strongly contributed to this field.

Based on the ideal shock tube theory, the shock wave and the contact surface propagate at a constant speed through the tube. However, when the viscous effects are considered, a boundary layer develops behind the shock wave, as shown in Figure 2.3. This causes the contact surface to accelerate, the shock wave to decelerate and the flow between these waves to be non-uniform [41]. In fact, the shock tube pressure ratio p_{41} is no longer expressed as in eq. 2.1. Instead, the viscous effects are now considered and the pressure ratio is now written as [42]

$$p_{41}^{*} = p_{41} + \Delta p_{visc} = \frac{p_4}{p_1} + \frac{\Delta p_{4visc}}{p_1}, \tag{2.2}$$

where

$$\frac{\Delta p_{4visc}}{p_1} = \frac{32 a_1 \mu_4}{D p_1} \frac{L^*}{D} M_s. \tag{2.3}$$

Therefore, the pressure ratio including the viscous effects is expressed as

$$p_{41}^{*} = \left[1 + \frac{2\gamma_1}{\gamma_1 + 1}\left(M_s^2 - 1\right)\right]\left[1 - \frac{\gamma_4 - 1}{\gamma_1 + 1}\left(\frac{a_1}{a_4}\right)\left(M_s - \frac{1}{M_s}\right)\right]^{\frac{-2\gamma_4}{\gamma_4 - 1}} + \frac{32 a_1 \mu_4}{D p_1} \frac{L^*}{D} M_s, \tag{2.4}$$

where D is the tube diameter, μ is the dynamic viscosity of the fluids and L^* is the distance between measuring position and high pressure chamber.

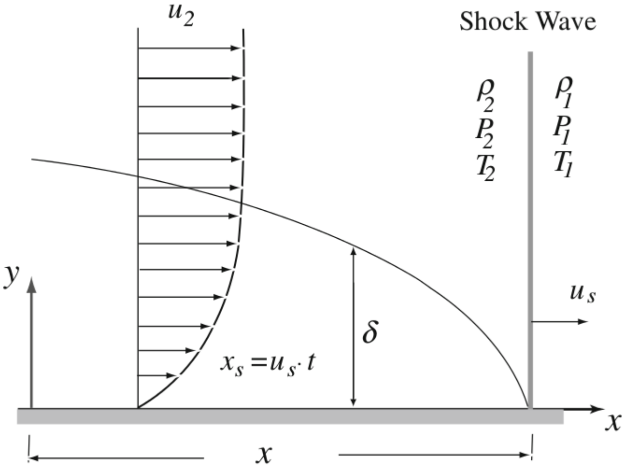

Figure 2.3: Boundary layer formation behind the propagated shock wave [7].

A pioneer experimental study of shock waves propagating in a low-pressure small-scale tube was carried by R. E. Duff [43] in 1959. Using an electron beam densitometer, a non-linear attenuation of the shock wave propagation for a certain diaphragm pressure ratio was observed. Note that in a macro shock tube, one would find a linear attenuation behaviour. Because of this, the required pressure ratio to generate a certain shock wave was proposed to be

$$p_{41}|_{Duff} = p_{41} + \left[1 + \frac{M_s^2 + \beta - 1}{(\beta - 1)\left[M_s^2(\beta + 1) - 1\right]}\right]^{\frac{\beta+1}{2}}, \tag{2.5}$$

where $\beta \equiv (\gamma + 1)/(\gamma - 1)$ and it intents to include the boundary layer effects. Regarding the contact surface propagating behind the shock wave, an acceleration was found, contrary to the shock wave deceleration. With this, a decay of the flow duration (defined by Duff as the time interval between the shock wave and the contact surface) was captured which could eventually become steady, defining a constant length between both waves. Such phenomenon was received with surprise since the macro shock tube theory predicts an increment of the flow duration even taking into account viscous effects. He stated that the decay of the flow duration was produced by the leakage of shocked gas through the contact surface mainly caused by the boundary layer developing behind the shock wave (this region is also known as hot gas). Duff also found that the boundary layer had an stronger effect on the shock wave attenuation by reducing the tube diameter, what was attributed to an increment of the viscous effects. As expected, dissipative effects become more important for high surface-to-volume ratios. Eventually, it was found that Duff's model tends to over-predict the required pressure ratio in eq. 2.5. Since scaling effects were not included either, the model was finally dropped.

In 1960, A. Roshko [44] came up with an analytical (and experimental) study of low-pressure shock tubes aiming to predict the flow duration phenomena observed by Duff. By taking into account an analytical solution of the mass flow in shock tubes developed by H. Mirels, he reformulated the β boundary layer parameter which intended to take into account the attenuation phenomena captured in Duff's experiment. Fixing the coordinate system in the contact surface, the boundary layer was assumed to be laminar and thin compared to the tube diameter, the shock wave speed was considered constant (do not confuse with the shock wave - contact surface relative velocity) and the flow between the shock wave and the contact surface was treated as uniform. Even though, Duff's experimental results regarding the flow duration leakage theory could be fairly described.

H. Mirels [41] proposed an analytical model in 1963 to predict the boundary layer effects on the shock waves propagation based on the method of characteristics intending to assess Duff's boundary layer parameter. Almost same considerations as Roshko's work were made. However, instead of assuming the flow to be uniform between the shock wave and the contact surface, he developed a laminar boundary layer theory to account for the non-uniform phenomena that take place in this region. He found that the analytical value of β was under-predicted, being this disagreement more significant for low shock wave speeds. Yet, Mirels's analytical model provided very similar results to Roshko's regarding the flow duration, since the shock wave speed was considered constant as well.

From the previous authors onwards, just over the last decade the interest for shock waves in small-scale tubes has been recovered. A significant contribution was presented by M. Brouillette [45] in 2003. He investigated the scale effects in a narrow tube by developing a model based on the modified Rayleigh line and the modified Hugoniot curve. Using a control volume that contains both the shock wave and the contact surface, he proposed the scaling parameter S that accounts for the diffusive transport phenomena (friction and heat transfer to the walls, mass transfer to the walls was not considered) present in small-scale tubes. Experimentally, a shock tube based on the classic diaphragm technique was constructed to validate the model, which resulted in a good agreement. Also, it was shown that Duff's model over-predicted the required diaphragm pressure ratio to generate a certain shock wave, as mentioned before. He stated that his model was able to predict rarefaction effects (since the scaling parameter is related to the Knudsen number) even though a correct value of the distance between the shock wave and the contact surface might be difficult to obtain. Finally, the flow was predicted to be isothermal and the minimum wave speed to be subsonic for small-scale shock tubes.

D. E. Zeitoun *et al.* [46] numerically studied the microscale shock tube using the 2D compressible N-S equations with the slip boundary condition and the temperature jump at the walls assuming a laminar flow. The numerical code used is named CARBUR and was developed by the CFD division of Marseille research group (see Y. Burtschell *et al.* [47]). This software uses a Godunov-type method with a 2$^{\text{nd}}$-order MUSCL extrapolation scheme for convective fluxes and a central difference scheme for the viscous terms. The time discretisation is performed by a 2$^{\text{nd}}$-order Runge-Kutta scheme and an exact Riemann solver is used as well. Zeitoun studied several scaling factors values based on Brouillette's work involving large Knudsen numbers (where rarefaction effects have to be considered). It was observed that the shock wave attenuation was stronger for a lower initial pressure or/and smaller tube diameters which could eventually become a compression wave for small scaling parameters (when more rarefaction effects take place). Also, the shock wave propagation speed increased with the slip boundary condition when compared to the no-slip one. After this work, D. E. Zeitoun *et al.* [3] studied the micro shock tube under stronger rarefied conditions. The compressible N-S equations (resolved using CARBUR and ITAM [48]) with no-slip and slip boundary conditions were compared to statistical models such as the Direct Simulation Monte Carlo (DSMC) and to Molecular Dynamics (MD) models. It was observed that for low Knudsen number flows (less than 0.01), the no-slip boundary condition was still a valid approach. However, for more rarefied flows, the slip and the temperature jump boundary conditions performed much more accurately than the no-slip one. With this, very similar results to the ones obtained through the kinetic approaches were captured. Therefore, it was justified the usage of the compressible N-S equations for micro shock tubes under rarefied conditions. This is a key finding that justifies the model that will be used in the present work.

J. Giordano *et al.* [49] designed an experimental small-scale shock tube by using a solenoid valve separating a high-pressure chamber from a intermediate-scale shock tube attached to the small-scale one. Although shock waves could successfully be generated, further development of the experiment was need in order to propagate them cleanly to the microtube. Later on J. Giordano *et al.* [16] carried another experiment in which the microscale tube was connected to a classic shock tube (using the diaphragm technique), so shock waves were easily transmitted to the microtube. It was claimed that until a Reynolds number close to 5000, the boundary layer developing behind the shock wave could be considered laminar, but for higher Reynolds numbers turbulence models shall be used. In fact, it is the first solid statement regarding turbulence in micro shock tubes that has been found and which provides a very useful information. His results were validated using the CARBUR code for which adiabatic walls with no-slip boundary conditions was considered. Therefore, rarefaction effects have not been treated together with a turbulent boundary layer approach yet in small-scale shock tubes. However, the shock attenuation described by previous authors (again accentuated for small diameters and low-pressures of the driven gas) was correctly captured.

W. Garen *et al.* [42] used a deformable quick-opening valve (instead of a diaphragm) separating an external high-pressure chamber from a microtube. Brouillette results regarding the scaling parameter where aimed to be reproduced. It was found that two different pressure ratios could provide a concrete shock wave speed. Also, as the shock wave was transmitted to the microtube, a brief acceleration was observed followed by the attenuation.

G. Mirsheraki *et al.* [7] proposed a 1D model of the conservation equations with added source terms to take into account the lateral transport effects. The two-step Lax-Wendroff - MacCormack method together with a FCT scheme were used to achieve a numerical solution. It has been an important contribution since recent authors are using this model to validate CFD and experimental analysis of shock waves propagation in small-scale tubes. However, this model does not consider rarefaction effects and the boundary layer is assumed to be laminar (as in Mirels's model), even though the boundary layer thickness is not neglected. With this, the shock wave attenuation is accurately captured for small Knudsen number flows. For the smallest scale simulated (10 μm) is shown that at a sufficient low-pressure ratio, the shock wave could eventually disappear. Mirsheraki stated that when strong rarefaction effects take place, it is a challenging task to develop theoretical even numerical models. D. Ngomo *et al.* [50] introduced a more sophisticated 1D model achieving results through a high-order WENO interpolation scheme as a numerical integration method. It was found that friction effects (diffusive shear stresses) and heat losses near the wall are one of the main reasons for the shock attenuation in narrow tubes (apart from the boundary layer interaction).

J. D. Parisse *et al.* [51] numerically investigated the generation of shock waves in small-sale tubes using the CARBUR code to solve the compressible N-S equations. Isothermal and adiabatic boundary conditions were considered as well low-Reynolds (laminar) flows. The connection of a classical shock tube with a small-scale tube was studied, eventually yielding to its real construction [16]. The same tube diameter effect regarding the shock wave attenuation was found and the unsteady flow between the contact surface and the shock wave was noted as well.

G. V. Shoev *et al.* [52] studied the entry and propagation of a shock wave in a microchannel from a numerical standpoint. Using a 5th-order WENO reconstruction scheme for the convective fluxes and a 4th-order central scheme for the dissipative terms, the fully compressible 2D N-S equations set was solved and compared to the DSMC results. A shock wave amplification as it enters the microchannel was observed (as found W. Garen *et al.* in [42]) and the consecutive shock wave attenuation was captured as well. Even though rarefaction effects were considered by implementing the slip and temperature jump conditions at the walls, the simulation was performed for a Knudsen number of 0.001, so such effects played a negligible role and could not be properly studied.

D. S. Watsvive *et al.* [53] used a DSMC simulation to study shock tubes at different sizes and rarefied conditions. In the slip flow regime, a shock wave deceleration and a contact surface acceleration was observed. Also, the shock wave could become a subsonic (compressible) wave even disappear for a Knudsen number higher than 0.1 due to severe wall effects, as noted in [46, 7]. Finally, it was stated that the the Tangential Momentum Accommodation Coefficient (TMAC) regarding the Maxwell's slip boundary condition is a key parameter for rarefied shock tubes and should be properly selected by performing multiple simulations with different values and choosing the one that eventually matches experimental reference data.

A. R. Kumar *et al.* [54, 55, 4] investigated a low-pressure rarefied shock tube for different tube diameters, wall boundary conditions and diaphragm pressure ratios. The simulations were performed by FLUENT-ANSYS software using a 3^{rd}-order MUSCL scheme and 1^{st}-order Maxwell's slip boundary condition implemented through a User Defined Function (UDF). The fully compressible axysimmetric N-S equations were solved and turbulence was accounted using the RANS $k-\omega$ SST turbulence model. The attenuation of the shock wave appeared to be more significant for small tube diameters and/or pressure ratios, as pointed out by other authors. It was also observed that the no-slip condition yielded to a more attenuated shock wave for rarefied flows in comparison to the slip condition since the latter reduced the viscous dissipation effects of the boundary layer developing behind the shock wave. Furthermore, the flow duration appeared to be shorter for large Knudsen number flows. As in [53], he found an eventual transformation of the shock wave into a compression wave for highly rarefied flows.

G. Mirsheraki *et al.* [56] presented the smallest fully instrumented shock tube fabricated at the moment. Their experimental results were compared to different analytical [41, 7, 50] and numerical [47] models. However, scale effects were not reproduced since the scaling parameter of the experiment was very high yielding to a Knudsen number around 0.002.

G. Zhang *et al.* [57] used FLUENT-ANSYS software to model a micro shock tube using the 2D axysimmetric N-S equations and including turbulence through the RANS $k-\omega$ SST model. Again, rarefaction effects were not included in this study. A high-Reynolds flow was simulated, which developed a turbulent boundary layer behind the shock wave resulting in a turbulent driver and driven sections. It was observed that a turbulent boundary layer yields to larger energy and momentum losses provoking a stronger attenuation of the shock wave.

Other authors that have contributed to the study of shock waves in small-scale tubes can be found in [15, 58, 59].

In conclusion, note that rarefaction effects in micro shock tubes have not been extensively studied. Just a few authors have dealt with large-Knudsen number flows and it has been pointed out the difficulty of performing such simulations. Furthermore, turbulence has been rarely included. Finally, high-order numerical schemes have not been implemented and studied in-depth yet in micro shock tube problems.

2.4 Perspectives of the Present Thesis

In the present thesis, a small-scale shock tube is numerically investigated through a shock wave-capturing Godunov-type method using high-resolution non-oscillatory schemes and approximate Riemann solvers. A continuum approach, the fully compressible N-S equations, together with the Maxwell's slip and the temperature jump boundary conditions at walls is considered. On one hand, a thorough investigation of multiple (very) high-order schemes is performed for an inviscid case. On the other hand, these schemes are used to capture the flow physics behind the shock wave propagation in small-scale shock tubes for slip and transitional flows. Altogether makes this work a state-of-the-art investigation in compressible microfludics that is not performed (to the best of our knowledge) by any other research groups.

Chapter 3

Governing Equations and Methodology

3.1 Governing Equations

The conservation of mass, momentum and energy describe the motion of fluids for continuum models. They can be written respectively as

$$\frac{\partial \rho}{\partial t} + \nabla \cdot (\rho \mathbf{u}) = 0, \tag{3.1}$$

$$\frac{\partial (\rho \mathbf{u})}{\partial t} + \nabla \cdot (\rho \mathbf{u} \otimes \mathbf{u}) = \nabla \cdot \underline{\underline{\sigma}} + \rho \mathbf{f}, \tag{3.2}$$

$$\frac{\partial E}{\partial t} + \nabla \cdot (E \mathbf{u}) = \nabla \cdot \left(\underline{\underline{\sigma}} \cdot \mathbf{u} \right) + \nabla \cdot (\kappa \nabla T) + \rho \mathbf{f} \cdot \mathbf{u}, \tag{3.3}$$

where E is the total energy and is decomposed into the internal energy e and the kinetic energy k as follows

$$E = \rho (e + k) = \frac{p}{\gamma - 1} + \frac{1}{2} \rho \left| \mathbf{u} \right|^2 = \frac{p}{\gamma - 1} + \frac{1}{2} \rho \left(u^2 + v^2 + w^2 \right). \tag{3.4}$$

For compressible flows, the system is closed with the equation of state that can be written as

$$p = \rho R T. \tag{3.5}$$

Additionally, a passive scalar transport equation has been introduced to the system which is expressed as

$$\frac{\partial \psi}{\partial t} + \nabla \cdot (\psi \mathbf{u}) = 0. \tag{3.6}$$

This equation has been implemented in the code as a temperature transport equation in order to validate it. The temperature transport equation is expressed as

$$\frac{\partial \vartheta}{\partial t} + (\mathbf{u}\cdot\nabla)\,\vartheta = -\frac{p}{\rho c_v}\nabla\cdot\mathbf{u} + \nabla\cdot(\alpha\nabla\vartheta) + \frac{1}{\rho c_v}\underline{\underline{\tau}} : \nabla\otimes\mathbf{u} + \frac{1}{\rho c_v} S_\vartheta. \tag{3.7}$$

Because of the data structure of the code, the equation that has been actually implemented is written as

$$\frac{\partial \vartheta}{\partial t} + \nabla\cdot(\vartheta\mathbf{u}) = -\frac{p}{\rho c_v}\nabla\cdot\mathbf{u} + \nabla\cdot(\alpha\nabla\vartheta) + \frac{1}{\rho c_v}\underline{\underline{\tau}} : \nabla\otimes\mathbf{u} + \frac{1}{\rho c_v} S_\vartheta + \vartheta\nabla\cdot\mathbf{u}, \tag{3.8}$$

where ϑ is a temperature field independent from the temperature field obtained through the energy equation and the state equation (T) and α is the thermal diffusivity computed as $\alpha = \frac{\kappa}{\rho c_v}$. With this, a scalar transport equation is considered and validated which can be used *e.g.* for species transport purposes. Note that in some formulations of this equation, the heat capacity at constant pressure c_p is used instead of the heat capacity at constant volume c_v. However the results of the present work yielded to the latter option, so the following relation prevails

$$e = c_V T. \tag{3.9}$$

By solving the temperature transport equation, one can validate the correct implementation of the general scalar transport equation by comparing the solution of the original temperature field and the one obtained through the temperature transport equation.

Now, let us move into the derivation of the viscous terms of the Navier-Stokes equations. Even though the code has been implemented in a 2D coordinate system, the 3D formulation is detailed next in order to see a more generalised derivation of the equations. With this, the fluid stresses are considered by the stress tensor $\underline{\underline{\sigma}}$ which can be decomposed as

$$\underline{\underline{\sigma}} = -p\underline{\underline{I}} + \underline{\underline{\tau}}, \tag{3.10}$$

where $\underline{\underline{\tau}}$ is the viscous stress tensor and $\underline{\underline{I}}$ is an identity matrix. They can be expressed as follows

$$\underline{\underline{\tau}} = \begin{pmatrix} \tau_{xx} & \tau_{xy} & \tau_{xz} \\ \tau_{yx} & \tau_{yy} & \tau_{yz} \\ \tau_{zx} & \tau_{zy} & \tau_{zz} \end{pmatrix} \qquad \underline{\underline{I}} = \begin{bmatrix} 1 & 0 & 0 \\ 0 & 1 & 0 \\ 0 & 0 & 1 \end{bmatrix}. \tag{3.11}$$

Hence, the stress tensor is written as

$$\underline{\underline{\sigma}} = -\begin{pmatrix} p & 0 & 0 \\ 0 & p & 0 \\ 0 & 0 & p \end{pmatrix} + \begin{pmatrix} \tau_{xx} & \tau_{xy} & \tau_{xz} \\ \tau_{yx} & \tau_{yy} & \tau_{yz} \\ \tau_{zx} & \tau_{zy} & \tau_{zz} \end{pmatrix}, \tag{3.12}$$

and the divergence of the stress tensor is therefore,

$$\nabla \cdot \underline{\underline{\sigma}} = -\underline{\underline{I}} \cdot \nabla p - p \nabla \cdot \underline{\underline{I}} + \nabla \cdot \underline{\underline{\tau}}. \tag{3.13}$$

Since $\nabla \cdot \underline{\underline{I}} = 0$ and $\underline{\underline{I}} \cdot \nabla p = \nabla p$, one can obtain the following relation

$$\nabla \cdot \underline{\underline{\sigma}} = -\nabla p + \nabla \cdot \underline{\underline{\tau}}, \tag{3.14}$$

for which each term is written as

$$\nabla p = \begin{pmatrix} \frac{\partial p}{\partial x} \\ \frac{\partial p}{\partial y} \\ \frac{\partial p}{\partial z} \end{pmatrix}, \tag{3.15}$$

$$\nabla \cdot \underline{\underline{\tau}} = \begin{pmatrix} \frac{\partial \tau_{xx}}{\partial x} + \frac{\partial \tau_{yx}}{\partial y} + \frac{\partial \tau_{zx}}{\partial z} \\ \frac{\partial \tau_{xy}}{\partial x} + \frac{\partial \tau_{yy}}{\partial y} + \frac{\partial \tau_{zy}}{\partial z} \\ \frac{\partial \tau_{xz}}{\partial x} + \frac{\partial \tau_{yz}}{\partial y} + \frac{\partial \tau_{zz}}{\partial z} \end{pmatrix}, \tag{3.16}$$

yielding to the following equation,

$$\nabla \cdot \underline{\underline{\sigma}} = -\begin{pmatrix} \frac{\partial p}{\partial x} \\ \frac{\partial p}{\partial y} \\ \frac{\partial p}{\partial z} \end{pmatrix} + \begin{pmatrix} \frac{\partial \tau_{xx}}{\partial x} + \frac{\partial \tau_{yx}}{\partial y} + \frac{\partial \tau_{zx}}{\partial z} \\ \frac{\partial \tau_{xy}}{\partial x} + \frac{\partial \tau_{yy}}{\partial y} + \frac{\partial \tau_{zy}}{\partial z} \\ \frac{\partial \tau_{xz}}{\partial x} + \frac{\partial \tau_{yz}}{\partial y} + \frac{\partial \tau_{zz}}{\partial z} \end{pmatrix}. \tag{3.17}$$

Regarding the stress tensor of the energy conservation equation, this can be derived as

$$\nabla \cdot \left(\underline{\underline{\sigma}} \cdot \mathbf{u} \right) = -\nabla \cdot (p\mathbf{u}) + \nabla \cdot \left(\underline{\underline{\tau}} \cdot \mathbf{u} \right), \tag{3.18}$$

$$\nabla \cdot (p\mathbf{u}) = \frac{\partial (pu)}{\partial x} + \frac{\partial (pv)}{\partial y} + \frac{\partial (pz)}{\partial z}, \tag{3.19}$$

$$\nabla \cdot \left(\underline{\underline{\tau}} \cdot \mathbf{u} \right) = \mathbf{u} \cdot \left(\nabla \cdot \underline{\underline{\tau}} \right) + \underline{\underline{\tau}} : \nabla \otimes \mathbf{u}, \tag{3.20}$$

where,

$$\mathbf{u}\cdot\left(\nabla\cdot\underline{\underline{\tau}}\right)=u\left(\frac{\partial\tau_{xx}}{\partial x}+\frac{\partial\tau_{yx}}{\partial y}+\frac{\partial\tau_{zx}}{\partial z}\right)+v\left(\frac{\partial\tau_{xy}}{\partial x}+\frac{\partial\tau_{yy}}{\partial y}+\frac{\partial\tau_{zy}}{\partial z}\right)+$$
$$+w\left(\frac{\partial\tau_{xz}}{\partial x}+\frac{\partial\tau_{yz}}{\partial y}+\frac{\partial\tau_{zz}}{\partial z}\right), \tag{3.21}$$

$$\underline{\underline{\tau}}:\nabla\otimes\mathbf{u}=\tau_{xx}\frac{\partial u}{\partial x}+\tau_{xy}\frac{\partial u}{\partial y}+\tau_{xz}\frac{\partial u}{\partial z}+\tau_{yx}\frac{\partial v}{\partial x}+\tau_{yy}\frac{\partial v}{\partial y}+\tau_{yz}\frac{\partial v}{\partial z}+$$
$$+\tau_{zx}\frac{\partial w}{\partial x}+\tau_{zy}\frac{\partial w}{\partial y}+\tau_{zz}\frac{\partial w}{\partial z}. \tag{3.22}$$

The $\underline{\underline{\tau}}:\nabla\otimes\mathbf{u}$ term above is the so called viscous dissipation function (φ_D), inherent in the energy equation. With this, the conservation equations can be expressed as

$$\frac{\partial\rho}{\partial t}+\nabla\cdot(\rho\mathbf{u})=0, \tag{3.23}$$

$$\frac{\partial(\rho\mathbf{u})}{\partial t}+\nabla\cdot(\rho\mathbf{u}\otimes\mathbf{u})=-\nabla p+\nabla\cdot\underline{\underline{\tau}}+\rho\mathbf{f}, \tag{3.24}$$

$$\frac{\partial E}{\partial t}+\nabla\cdot(E\mathbf{u})=-\nabla\cdot(p\mathbf{u})+\mathbf{u}\cdot\left(\nabla\cdot\underline{\underline{\tau}}\right)+\underline{\underline{\tau}}:\nabla\otimes\mathbf{u}+\nabla\cdot(\kappa\nabla T)+\rho\mathbf{f}\cdot\mathbf{u}, \tag{3.25}$$

Now recovering the original form of the viscous term in the energy equation $\nabla\cdot\left(\underline{\underline{\tau}}\cdot\mathbf{u}\right)$, let us rewrite the conservation equations plus the passive scalar transport equation in its scalar form as follows

$$\frac{\partial\rho}{\partial t}+\frac{\partial(\rho u)}{\partial x}+\frac{\partial(\rho v)}{\partial y}+\frac{\partial(\rho w)}{\partial z}=0, \tag{3.26}$$

$$\frac{\partial(\rho u)}{\partial t}+\frac{\partial\left(\rho u^2\right)}{\partial x}+\frac{\partial(\rho uv)}{\partial y}+\frac{\partial(\rho uw)}{\partial z}=-\frac{\partial p}{\partial x}+\frac{\partial\tau_{xx}}{\partial x}+\frac{\partial\tau_{yx}}{\partial y}+\frac{\partial\tau_{zx}}{\partial z}+\rho f_x, \tag{3.27}$$

$$\frac{\partial(\rho v)}{\partial t}+\frac{\partial(\rho vu)}{\partial x}+\frac{\partial\left(\rho v^2\right)}{\partial y}+\frac{\partial(\rho vw)}{\partial z}=-\frac{\partial p}{\partial y}+\frac{\partial\tau_{xy}}{\partial x}+\frac{\partial\tau_{yy}}{\partial y}+\frac{\partial\tau_{zy}}{\partial z}+\rho f_y, \tag{3.28}$$

$$\frac{\partial(\rho w)}{\partial t}+\frac{\partial(\rho wu)}{\partial x}+\frac{\partial(\rho wv)}{\partial y}+\frac{\partial\left(\rho w^2\right)}{\partial z}=-\frac{\partial p}{\partial z}+\frac{\partial\tau_{xz}}{\partial x}+\frac{\partial\tau_{yz}}{\partial y}+\frac{\partial\tau_{zz}}{\partial z}+\rho f_z, \tag{3.29}$$

$$\frac{\partial E}{\partial t}+\frac{\partial(Eu)}{\partial x}+\frac{\partial(Ev)}{\partial y}+\frac{\partial(Ew)}{\partial z}=-\frac{\partial(pu)}{\partial x}-\frac{\partial(pv)}{\partial y}-\frac{\partial(pw)}{\partial z}+$$
$$+\frac{\partial(\tau_{xx}u)}{\partial x}+\frac{\partial(\tau_{yx}u)}{\partial y}+\frac{\partial(\tau_{zx}u)}{\partial z}+\frac{\partial(\tau_{xy}v)}{\partial x}+\frac{\partial(\tau_{yy}v)}{\partial y}+\frac{\partial(\tau_{zy}v)}{\partial z}+$$

$$+\frac{\partial\left(\tau_{xz}w\right)}{\partial x}+\frac{\partial\left(\tau_{yz}w\right)}{\partial y}+\frac{\partial\left(\tau_{zz}w\right)}{\partial z}+\frac{\partial}{\partial x}\left(\kappa\frac{\partial T}{\partial x}\right)+\frac{\partial}{\partial y}\left(\kappa\frac{\partial T}{\partial y}\right)+\frac{\partial}{\partial z}\left(\kappa\frac{\partial T}{\partial z}\right)+$$

$$+\rho\left(f_x u+f_y v+f_z w\right), \tag{3.30}$$

$$\frac{\partial\psi}{\partial t}+\frac{\partial\left(\rho\psi\right)}{\partial x}+\frac{\partial\left(\rho\psi\right)}{\partial y}+\frac{\partial\left(\rho\psi\right)}{\partial z}=0. \tag{3.31}$$

The temperature transport equation (eq. 3.8) in its scalar form is written as

$$\frac{\partial\vartheta}{\partial t}+\frac{\partial\left(\vartheta u\right)}{\partial x}+\frac{\partial\left(\vartheta v\right)}{\partial y}+\frac{\partial\left(\vartheta w\right)}{\partial z}=-\frac{p}{\rho c_v}\left(\frac{\partial u}{\partial x}+\frac{\partial v}{\partial y}+\frac{\partial w}{\partial z}\right)+\frac{\partial}{\partial x}\left(\alpha\frac{\partial\vartheta}{\partial x}\right)+$$

$$+\frac{\partial}{\partial y}\left(\alpha\frac{\partial\vartheta}{\partial y}\right)+\frac{\partial}{\partial z}\left(\alpha\frac{\partial\vartheta}{\partial z}\right)+\frac{1}{\rho c_v}\left(\tau_{xx}\frac{\partial u}{\partial x}+\tau_{xy}\frac{\partial u}{\partial y}+\tau_{xz}\frac{\partial u}{\partial z}+\tau_{yx}\frac{\partial v}{\partial x}+\tau_{yy}\frac{\partial v}{\partial y}+\right.$$

$$\left.+\tau_{yz}\frac{\partial v}{\partial z}+\tau_{zx}\frac{\partial w}{\partial x}+\tau_{zy}\frac{\partial w}{\partial y}+\tau_{zz}\frac{\partial w}{\partial z}\right)+\frac{1}{\rho c_v}S_\vartheta+\vartheta\left(\frac{\partial u}{\partial x}+\frac{\partial v}{\partial y}+\frac{\partial w}{\partial z}\right). \tag{3.32}$$

In order to compute the components of the viscous stress tensor $\underline{\underline{\tau}}$, the following decomposition is presented

$$\underline{\underline{\tau}}=2\mu\underline{\underline{S}}-\frac{2}{3}\mu\nabla\cdot\mathbf{u}\underline{\underline{I}}, \tag{3.33}$$

where $\underline{\underline{S}}$ is the symmetric tensor written as

$$\underline{\underline{S}}=\frac{1}{2}\left[\nabla\otimes\mathbf{u}+\left(\nabla\otimes\mathbf{u}\right)^T\right], \tag{3.34}$$

being $\nabla\otimes\mathbf{u}$ the velocity gradient tensor which is expressed as

$$\nabla\otimes\mathbf{u}=\begin{pmatrix}\frac{\partial u}{\partial x} & \frac{\partial u}{\partial y} & \frac{\partial u}{\partial z}\\ \frac{\partial v}{\partial x} & \frac{\partial v}{\partial y} & \frac{\partial v}{\partial z}\\ \frac{\partial w}{\partial x} & \frac{\partial w}{\partial y} & \frac{\partial w}{\partial z}\end{pmatrix}. \tag{3.35}$$

With this, the symmetric tensor can be written as

$$\underline{\underline{S}}=\frac{1}{2}\begin{pmatrix}2\frac{\partial u}{\partial x} & \frac{\partial u}{\partial y}+\frac{\partial v}{\partial x} & \frac{\partial u}{\partial z}+\frac{\partial w}{\partial x}\\ \frac{\partial v}{\partial x}+\frac{\partial u}{\partial y} & 2\frac{\partial v}{\partial y} & \frac{\partial v}{\partial z}+\frac{\partial w}{\partial y}\\ \frac{\partial w}{\partial x}+\frac{\partial u}{\partial z} & \frac{\partial w}{\partial y}+\frac{\partial v}{\partial z} & 2\frac{\partial w}{\partial z}\end{pmatrix}. \tag{3.36}$$

The divergence of the velocity field (vector) times an identity matrix gives the following equation

$$\nabla\cdot\mathbf{u}\underline{\underline{I}} = \begin{pmatrix} \frac{\partial u}{\partial x}+\frac{\partial v}{\partial y}+\frac{\partial w}{\partial z} & 0 & 0 \\ 0 & \frac{\partial u}{\partial x}+\frac{\partial v}{\partial y}+\frac{\partial w}{\partial z} & 0 \\ 0 & 0 & \frac{\partial u}{\partial x}+\frac{\partial v}{\partial y}+\frac{\partial w}{\partial z} \end{pmatrix}. \tag{3.37}$$

Taking into account eq. 3.36 and eq. 3.37, the viscous stress tensor $\underline{\underline{\tau}}$ can be written as

$$\underline{\underline{\tau}} = \begin{pmatrix} 2\mu\frac{\partial u}{\partial x}-\frac{2}{3}\mu\nabla\cdot\mathbf{u} & \mu\left(\frac{\partial u}{\partial y}+\frac{\partial v}{\partial x}\right) & \mu\left(\frac{\partial u}{\partial z}+\frac{\partial w}{\partial x}\right) \\ \mu\left(\frac{\partial v}{\partial x}+\frac{\partial u}{\partial y}\right) & 2\mu\frac{\partial v}{\partial y}-\frac{2}{3}\mu\nabla\cdot\mathbf{u} & \mu\left(\frac{\partial v}{\partial z}+\frac{\partial w}{\partial y}\right) \\ \mu\left(\frac{\partial w}{\partial x}+\frac{\partial u}{\partial z}\right) & \mu\left(\frac{\partial w}{\partial y}+\frac{\partial v}{\partial z}\right) & 2\mu\frac{\partial w}{\partial z}-\frac{2}{3}\mu\nabla\cdot\mathbf{u} \end{pmatrix}. \tag{3.38}$$

Therefore, the components of the viscous stress tensor are written as follows

$$\tau_{xx} = 2\mu\frac{\partial u}{\partial x}-\frac{2}{3}\mu\left(\frac{\partial u}{\partial x}+\frac{\partial v}{\partial y}+\frac{\partial w}{\partial z}\right), \tag{3.39}$$

$$\tau_{yy} = 2\mu\frac{\partial v}{\partial y}-\frac{2}{3}\mu\left(\frac{\partial u}{\partial x}+\frac{\partial v}{\partial y}+\frac{\partial w}{\partial z}\right), \tag{3.40}$$

$$\tau_{zz} = 2\mu\frac{\partial w}{\partial z}-\frac{2}{3}\mu\left(\frac{\partial u}{\partial x}+\frac{\partial v}{\partial y}+\frac{\partial w}{\partial z}\right), \tag{3.41}$$

$$\tau_{xy} = \tau_{yx} = \mu\left(\frac{\partial u}{\partial y}+\frac{\partial v}{\partial x}\right), \tag{3.42}$$

$$\tau_{xz} = \tau_{zx} = \mu\left(\frac{\partial u}{\partial z}+\frac{\partial w}{\partial x}\right), \tag{3.43}$$

$$\tau_{yw} = \tau_{wy} = \mu\left(\frac{\partial v}{\partial z}+\frac{\partial w}{\partial y}\right). \tag{3.44}$$

With this, the viscous term of the Navier-Stokes equations (eq.3.16) is expressed as

$$\begin{aligned} \nabla\cdot\underline{\underline{\tau}} = & \left[\frac{\partial}{\partial x}\left(2\mu\frac{\partial u}{\partial x}-\frac{2}{3}\mu\left(\frac{\partial u}{\partial x}+\frac{\partial v}{\partial y}+\frac{\partial w}{\partial z}\right)\right)+\frac{\partial}{\partial y}\left(\mu\left(\frac{\partial u}{\partial y}+\frac{\partial v}{\partial x}\right)\right)+\right. \\ & \left.+\frac{\partial}{\partial z}\left(\mu\left(\frac{\partial u}{\partial z}+\frac{\partial w}{\partial x}\right)\right)\right]\overrightarrow{\imath}+\left[\frac{\partial}{\partial x}\left(\mu\left(\frac{\partial u}{\partial y}+\frac{\partial v}{\partial x}\right)\right)+\right. \\ & \left.+\frac{\partial}{\partial y}\left(2\mu\frac{\partial v}{\partial y}-\frac{2}{3}\mu\left(\frac{\partial u}{\partial x}+\frac{\partial v}{\partial y}+\frac{\partial w}{\partial z}\right)\right)+\frac{\partial}{\partial z}\left(\mu\left(\frac{\partial v}{\partial z}+\frac{\partial w}{\partial y}\right)\right)\right]\overrightarrow{\jmath}+ \end{aligned}$$

$$+\left[\frac{\partial}{\partial x}\left(\mu\left(\frac{\partial u}{\partial z}+\frac{\partial w}{\partial x}\right)\right)+\frac{\partial}{\partial y}\left(\mu\left(\frac{\partial v}{\partial z}+\frac{\partial w}{\partial y}\right)\right)+\right.$$
$$\left.+\frac{\partial}{\partial z}\left(2\mu\frac{\partial w}{\partial z}-\frac{2}{3}\mu\left(\frac{\partial u}{\partial x}+\frac{\partial v}{\partial y}+\frac{\partial w}{\partial z}\right)\right)\right]\overrightarrow{k}. \tag{3.45}$$

And the viscous dissipation function takes the following form (after some algebraic manipulation)

$$\varphi_D=\underline{\underline{\tau}}:\nabla\otimes\mathbf{u}=\mu\left[2\left(\left(\frac{\partial u}{\partial x}\right)^2+\left(\frac{\partial v}{\partial y}\right)^2+\left(\frac{\partial w}{\partial z}\right)^2\right)+\left(\frac{\partial u}{\partial y}+\frac{\partial v}{\partial x}\right)^2+\right.$$
$$\left.+\left(\frac{\partial u}{\partial z}+\frac{\partial w}{\partial x}\right)^2+\left(\frac{\partial v}{\partial z}+\frac{\partial w}{\partial y}\right)^2\right]. \tag{3.46}$$

The governing equations are summarised next in the vectorial form (including the passive scalar transport equation)

$$\frac{\partial\mathbf{U}}{\partial t}+\frac{\partial\mathbf{F_a}}{\partial x}+\frac{\partial\mathbf{G_a}}{\partial y}+\frac{\partial\mathbf{H_a}}{\partial z}=\frac{\partial\mathbf{F_v}}{\partial x}+\frac{\partial\mathbf{G_v}}{\partial y}+\frac{\partial\mathbf{H_v}}{\partial z}+\mathbf{S}, \tag{3.47}$$

where $\mathbf{U}$ stands for the conserved variables, $\mathbf{F_a},\mathbf{G_a},\mathbf{H_a}$ are the advective fluxes, $\mathbf{F_v},\mathbf{G_v},\mathbf{H_v}$ are the viscous fluxes and $\mathbf{S}$ are the source terms. Each vector is detailed below

$$\mathbf{U}=\begin{bmatrix}\rho\\ \rho u\\ \rho v\\ \rho w\\ E\\ \psi\end{bmatrix},\qquad \mathbf{S}=\begin{bmatrix}0\\ \rho f_x\\ \rho f_y\\ \rho f_z\\ \rho\left(f_x u+f_y v+f_z w\right)\\ 0\end{bmatrix}, \tag{3.48}$$

$$\mathbf{F_a}=\begin{bmatrix}\rho u\\ \rho u^2+p\\ \rho vu\\ \rho wu\\ (E+p)u\\ \psi u\end{bmatrix},\qquad \mathbf{G_a}=\begin{bmatrix}\rho v\\ \rho uv\\ \rho v^2+p\\ \rho wv\\ (E+p)v\\ \psi v\end{bmatrix},\qquad \mathbf{H_a}=\begin{bmatrix}\rho w\\ \rho uw\\ \rho vw\\ \rho w^2+p\\ (E+p)w\\ \psi w\end{bmatrix}, \tag{3.49}$$

$$\mathbf{F_v} = \begin{bmatrix} 0 \\ \tau_{xx} \\ \tau_{xy} \\ \tau_{xz} \\ \tau_{xx}u + \tau_{xy}v + \tau_{xz}w + \kappa\frac{\partial T}{\partial x} \\ 0 \end{bmatrix}, \quad \mathbf{G_v} = \begin{bmatrix} 0 \\ \tau_{yx} \\ \tau_{yy} \\ \tau_{yz} \\ \tau_{yx}u + \tau_{yy}v + \tau_{yz}w + \kappa\frac{\partial T}{\partial y} \\ 0 \end{bmatrix},$$

$$\mathbf{H_v} = \begin{bmatrix} 0 \\ \tau_{zx} \\ \tau_{zy} \\ \tau_{zz} \\ \tau_{zx}u + \tau_{zy}v + \tau_{zz}w + \kappa\frac{\partial T}{\partial z} \\ 0 \end{bmatrix}. \tag{3.50}$$

Besides the 2D Cartesian coordinate system, the 2D axisymmetric coordinate system has been implemented as well. It is a coordinate system widely used in tube-related applications and, therefore, worth to be included in the Minitube2D in-house code. Skipping now the derivation of the conservation equations (which can be consulted in [60]), the scalar form of the system of equations can be written as

$$\frac{\partial \rho}{\partial t} + \frac{\partial (\rho u)}{\partial z} + \frac{\partial (\rho v)}{\partial r} + \frac{\rho v}{r} = 0, \tag{3.51}$$

$$\frac{\partial (\rho u)}{\partial t} + \frac{\partial \left(\rho u^2\right)}{\partial z} + \frac{\partial (\rho u v)}{\partial r} + \frac{\rho u v}{r} = -\frac{\partial p}{\partial z} + \frac{\partial \tau_{zz}}{\partial z} + \frac{\partial \tau_{rz}}{\partial r} + \frac{\tau_{rz}}{r} + \rho f_z, \tag{3.52}$$

$$\frac{\partial (\rho v)}{\partial t} + \frac{\partial (\rho v u)}{\partial z} + \frac{\partial \left(\rho v^2\right)}{\partial r} + \frac{\rho v^2}{r} = -\frac{\partial p}{\partial r} + \frac{\partial \tau_{zr}}{\partial z} + \frac{\partial \tau_{rr}}{\partial r} + \frac{\tau_{rr}}{r} - \frac{\tau_{\theta\theta}}{r} + \rho f_r, \tag{3.53}$$

$$\begin{aligned} &\frac{\partial E}{\partial t} + \frac{\partial (E u)}{\partial z} + \frac{\partial (E v)}{\partial r} + \frac{E v}{r} = -\frac{\partial (p u)}{\partial z} - \frac{\partial (p v)}{\partial r} - \frac{p v}{r} + \\ &+ u\left(\frac{\partial \tau_{zz}}{\partial z} + \frac{\partial \tau_{rz}}{\partial r} + \frac{\tau_{rz}}{r}\right) + v\left(\frac{\partial \tau_{zr}}{\partial z} + \frac{\partial \tau_{rr}}{\partial r} + \frac{\tau_{rr}}{r} - \frac{\tau_{\theta\theta}}{r}\right) + \\ &+ \tau_{zz}\frac{\partial u}{\partial z} + \tau_{zr}\frac{\partial u}{\partial r} + \tau_{rz}\frac{\partial v}{\partial r} + \tau_{rr}\frac{\partial v}{\partial r} + \tau_{\theta\theta}\frac{v}{r} + \\ &+ \frac{\partial}{\partial z}\left(\kappa\frac{\partial T}{\partial z}\right) + \frac{\partial}{\partial r}\left(\kappa\frac{\partial T}{\partial r}\right) + \frac{1}{r}\left(\kappa\frac{\partial T}{\partial r}\right) + \rho\left(f_z u + f_r v\right), \end{aligned} \tag{3.54}$$

$$\frac{\partial \psi}{\partial t} + \frac{\partial (\psi u)}{\partial z} + \frac{\partial (\psi v)}{\partial r} + \frac{\psi v}{r} = 0. \tag{3.55}$$

The temperature transport equation is written as

$$\frac{\partial \vartheta}{\partial t}+\frac{\partial(\vartheta u)}{\partial z}+\frac{\partial(\vartheta v)}{\partial r}=-\frac{p}{\rho c_v}\left(\frac{\partial u}{\partial z}+\frac{\partial v}{\partial r}+\frac{v}{r}\right)+\frac{\partial}{\partial z}\left(\alpha\frac{\partial \vartheta}{\partial z}\right)+\frac{\partial}{\partial r}\left(\alpha\frac{\partial \vartheta}{\partial r}\right)+$$
$$+\frac{1}{r}\left(\alpha\frac{\partial \vartheta}{\partial r}\right)+\frac{1}{\rho c_v}\left(\tau_{zz}\frac{\partial u}{\partial z}+\tau_{zr}\frac{\partial u}{\partial r}+\tau_{rz}\frac{\partial v}{\partial r}+\tau_{rr}\frac{\partial v}{\partial r}+\tau_{\theta\theta}\frac{v}{r}\right)+$$
$$+\frac{1}{\rho c_v}S_\vartheta+\vartheta\left(\frac{\partial u}{\partial z}+\frac{\partial v}{\partial r}+\frac{v}{r}\right), \tag{3.56}$$

where z is the axial (horizontal) direction, r is the radial (vertical) direction, θ is the angle, u is the velocity component in the axial direction and v is the velocity component in the radial direction. The viscous stress tensor terms are expressed as

$$\tau_{zz}=2\mu\frac{\partial u}{\partial z}-\frac{2}{3}\mu\left(\frac{\partial u}{\partial z}+\frac{\partial v}{\partial r}+\frac{v}{r}\right), \tag{3.57}$$

$$\tau_{zr}=\tau_{rz}=\mu\left(\frac{\partial u}{\partial r}+\frac{\partial v}{\partial z}\right), \tag{3.58}$$

$$\tau_{rr}=2\mu\frac{\partial v}{\partial r}-\frac{2}{3}\mu\left(\frac{\partial u}{\partial z}+\frac{\partial v}{\partial r}+\frac{v}{r}\right), \tag{3.59}$$

$$\tau_{\theta\theta}=2\mu\frac{v}{r}-\frac{2}{3}\mu\left(\frac{\partial u}{\partial z}+\frac{\partial v}{\partial r}+\frac{v}{r}\right), \tag{3.60}$$

while the other terms of the tensor are 0 for the 2D case. Finally, the vectorial form of the 2D axisymmetric coordinate system is written as

$$\frac{\partial \mathbf{U}}{\partial t}+\frac{\partial \mathbf{F_a}}{\partial z}+\frac{\partial \mathbf{G_a}}{\partial r}+\frac{1}{r}\mathbf{B}=\frac{\partial \mathbf{F_v}}{\partial z}+\frac{\partial \mathbf{G_v}}{\partial r}+\mathbf{S}, \tag{3.61}$$

$$\mathbf{U}=\begin{bmatrix}\rho\\ \rho u\\ \rho v\\ E\\ \psi\end{bmatrix},\qquad \mathbf{S}=\begin{bmatrix}0\\ \rho f_z\\ \rho f_r\\ \rho\left(f_z u+f_r v\right)\\ 0\end{bmatrix},\qquad \mathbf{B}=\begin{bmatrix}\rho v\\ \rho uv-\tau_{rz}\\ \rho v^2-\tau_{rr}+\tau_{\theta\theta}\\ (E+p)v-u\tau_{rz}-v\tau_{rr}\\ \psi v\end{bmatrix}, \tag{3.62}$$

$$\mathbf{F_a} = \begin{bmatrix} \rho u \\ \rho u^2 + p \\ \rho v u \\ (E+p)u \\ \psi u \end{bmatrix}, \qquad \mathbf{G_a} = \begin{bmatrix} \rho v \\ \rho u v \\ \rho v^2 + p \\ (E+p)v \\ \psi v \end{bmatrix}, \tag{3.63}$$

$$\mathbf{F_v} = \begin{bmatrix} 0 \\ \tau_{zz} \\ \tau_{zr} \\ \tau_{zz}u + \tau_{zr}v + \kappa\frac{\partial T}{\partial z} \\ 0 \end{bmatrix}, \qquad \mathbf{G_v} = \begin{bmatrix} 0 \\ \tau_{rz} \\ \tau_{rr} \\ \tau_{rz}u + \tau_{rr}v + \kappa\frac{\partial T}{\partial r} \\ 0 \end{bmatrix}. \tag{3.64}$$

3.1.1 Boundary Conditions

On one hand, the boundary conditions (BCs) at the left and the right sides of the tube are defined as a Dirichlet-type BC by imposing the initial state values of the conserved variables at such boundaries. On the other hand, the solid boundaries that define the tube are treated as stationary walls with either the no-slip BC or the Maxwell's slip BC depending on the Knudsen number of the given case. The temperature BC at the walls also depends on the Knudsen number and the temperature jump BC is implemented for slip and transitional flows. For the no-slip BC, the velocity field is considered 0 at the wall whereas for the Maxwell's slip BC, the stream-wise velocity component at the wall is defined as

$$u_s - u_{wall} = \frac{2-\sigma_v}{\sigma_v}\lambda\left(\frac{\partial u}{\partial n}\right)_{wall} + \frac{3}{4}\frac{\mu}{\rho T}\left(\frac{\partial T}{\partial s}\right)_{wall}, \tag{3.65}$$

where u_s is the slip velocity, u_{wall} is the velocity of the wall (0 for stationary walls), σ_v is the tangential momentum accommodation coefficient (TMAC), λ is the mean free path (MFP), $\left(\frac{\partial u}{\partial n}\right)_{wall}$ is the normal derivative of the stream-wise velocity component at the wall and $\left(\frac{\partial T}{\partial s}\right)_{wall}$ is the stream-wise derivative of the temperature at the wall. The MFP can be written as

$$\lambda = \sqrt{\frac{\pi}{2}}\frac{\mu}{\sqrt{\rho p}}. \tag{3.66}$$

The TMAC defines the stream-wise momentum ratio transferred to the walls upon collisions [61]. It is defined as follows

$$\sigma_v = \frac{u_r - u_i}{u_w - u_i}, \tag{3.67}$$

where u_i is the average stream-wise velocity of the molecules colliding with the wall (incident), u_r is the average stream-wise velocity of the molecules reflected from the wall and u_w is the wall velocity. The fraction of molecules that are perfectly reflected from the wall is the defined as $1-\sigma_v$. Therefore, for $\sigma_v = 0$ all molecules colliding with the wall are perfectly reflected (specular reflection, no momentum is transferred to the wall) whereas for $\sigma_v = 1$ all molecules are diffusely reflected thus transferring their momentum to the wall. In practical terms, for most of the microchannels operating with slip flows a value of the TMAC between 0.8 and 1.0 is found [12]. In fact, modelling microfluidic applications with $\sigma_v = 1$ usually yields to a good correlation with experimental results. For example, M. H. Khadem *et al.* [62] found a TMAC value of 0.9 for microchannels after extensive experimental studies.

The temperature jump BC is defined as

$$T_s - T_{wall} = \frac{2-\sigma_T}{\sigma_T} \frac{2\gamma}{\gamma+1} \frac{\lambda}{Pr} \left(\frac{\partial T}{\partial n}\right)_{wall}, \tag{3.68}$$

where T_s is the temperature at the wall under rarefied conditions (the one aimed to be computed), T_{wall} is the reference wall temperature, σ_T is the tangential energy accommodation coefficient (TMAC), Pr is the Prandtl number and $\left(\frac{\partial T}{\partial n}\right)_{wall}$ is the normal derivative of the temperature at the wall.

3.1.2 Thermodynamics Transport Properties

The dynamic viscosity of the fluid, the heat capacity at constant pressure or volume and the thermal conductivity are referred as transport properties and they must be correctly defined in order to accurately compute the viscous fluxes. The dynamic viscosity is computed through the Sutherland's law which takes the viscosity as a function of the temperature and can be written as

$$\mu(T) = \frac{C_1 T^{3/2}}{T+S} \left[\frac{kg}{ms}\right], \tag{3.69}$$

$$C_1 = \frac{\mu_0}{T_0^{3/2}}(T_0+S), \tag{3.70}$$

where C_1 is the Sutherland's constant calculated with the reference viscosity μ_0, the reference temperature T_0 and the Sutherland's temperature S. Every material (gas) has different values for these constants.

The heat capacity at constant pressure and the thermal conductivity are taken as function of the temperature by using empirical formulations. As an example, these expressions are respectively shown below for dry air at a temperature between 100K and 1300K [63]

$$c_p(T) = 1034.09 - 2.849 \cdot 10^{-1} T + 7.817 \cdot 10^{-4} T^2 - 4.971 \cdot 10^{-7} T^3 +$$

$$+1.077 \cdot 10^{-10} T^4 \left[\frac{J}{kgK}\right], \tag{3.71}$$

$$\kappa(T) = \frac{6.648 \cdot 10^{-3} \sqrt{T}}{1 + (245.4/T) \cdot 10^{-12/T}} \left[\frac{W}{mK}\right]. \tag{3.72}$$

Finally, the heat capacity at constant volume is computed using the following thermodynamic relation

$$R = c_p - c_v. \tag{3.73}$$

For some of the simulated gases, the relation of the thermodynamic transport properties in function of the temperature could no be found and constant values were considered instead.

3.2 Numerical Methods

The micro shock tube physical domain is discretised into computational cells for which the governing equations are conserved. The data structure relies on the conservative form of the equations so the values stored at each cell are the conserved variables $\mathbf{U}$ of the equations system and these are updated at each time step. A cell-centred Godunov-type Finite Volume Method (FVM) is used to compute the advective fluxes whereas the viscous fluxes and the source terms are calculated through a Finite Difference Method (FDM) using the cell-centred points.

Figure 3.1 displays the location of the ghost cells (thin lines) out of the physical discretised domain (thick lines). The ghost cells are required when considering high-order stencils close to boundaries. The following sections detail the numerical method used for each term of the equations.

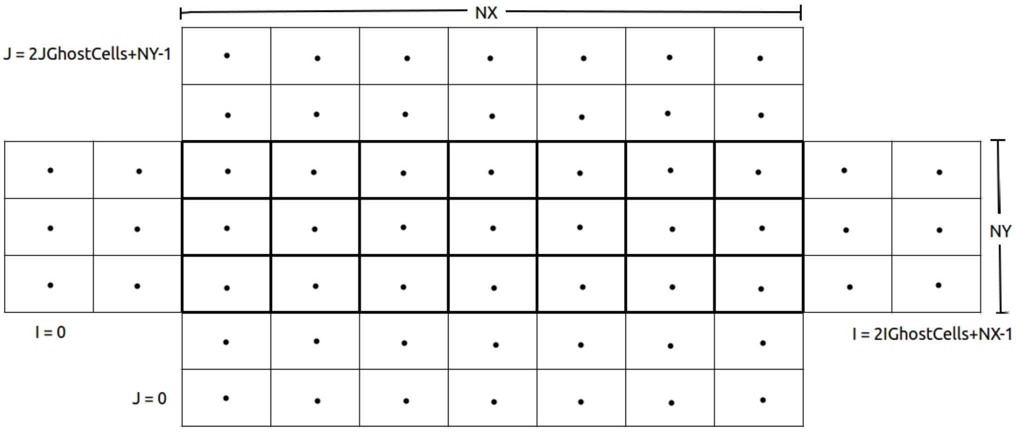

Figure 3.1: 2D Rectangular grid with ghost cells.

3.2.1 Advective Fluxes

As described in the previous chapter, the Godunov method is a very interesting approach to compute the advective fluxes for shock waves-related problems. Since it includes the solution of the RP at each cell interface, the wave propagation phenomena through the cells is correctly captured achieving a physical solution.

Let us considered a 3D Cartesian domain for which a computational cell is defined as: $I_i = \left[x_{i-1/2}, x_{i+1/2}\right] \times \left[y_{j-1/2}, y_{j+1/2}\right] \times \left[z_{k-1/2}, z_{k+1/2}\right]$ for $i = 1,...,N_x$, $j = 1,...,N_y$, $k = 1,...,N_z$. The time integration goes from t^n to t^{n+1} and therefore a control volume in space and time is defined as $V = I_i \times \left[t^n, t^{n+1}\right]$. With this, the integral form of the conservation equations (eq. 3.47) without considering the viscous terms and the source term is written in a semi-discrete form as [64, 22]

$$\frac{d}{dt}\mathbf{U}_{ijk}(t) = \frac{1}{\Delta x}\left[(\mathbf{F_a})_{i-1/2,jk} - (\mathbf{F_a})_{i+1/2,jk}\right] + \frac{1}{\Delta y}\left[(\mathbf{G_a})_{i,j-1/2,k} - (\mathbf{G_a})_{i,j+1/2,k}\right] +$$

$$+\frac{1}{\Delta z}\left[(\mathbf{H_a})_{ij,k-1/2} - (\mathbf{H_a})_{ij,k+1/2}\right], \tag{3.74}$$

where $\mathbf{U}_{ijk}(t)$ is the space average of the solution at time t in the I_{ijk} cell and is expressed as

$$\mathbf{U}_{ijk}(t) = \frac{1}{\Delta x \Delta y \Delta z}\int_{x_{i-1/2}}^{x_{i+1/2}}\int_{y_{j-1/2}}^{y_{j+1/2}}\int_{z_{k-1/2}}^{z_{k+1/2}} \mathbf{U}(x,y,x,t)\, dz dy dx, \tag{3.75}$$

and $(\mathbf{F_a})_{i\pm1/2,jk}$, $(\mathbf{G_a})_{i,j\pm1/2,k}$, $(\mathbf{H_a})_{ij,k\pm1/2}$ are the physical fluxes averaged in space at time t over intercell faces and can be written as

$$(\mathbf{F_a})_{i\pm1/2,jk} = \frac{1}{\Delta y \Delta z} \int_{y_{j-1/2}}^{y_{j+1/2}} \int_{z_{k-1/2}}^{z_{k+1/2}} \mathbf{F_a}\left(\mathbf{U}\left(x_{i\pm1/2}, y, z, t\right)\right) dzdy, \tag{3.76}$$

$$(\mathbf{G_a})_{i,j\pm1/2,k} = \frac{1}{\Delta x \Delta z} \int_{x_{i-1/2}}^{x_{i+1/2}} \int_{z_{k-1/2}}^{z_{k+1/2}} \mathbf{G_a}\left(\mathbf{U}\left(x, y_{j\pm1/2}, z, t\right)\right) dzdx, \tag{3.77}$$

$$(\mathbf{H_a})_{ij,k\pm1/2} = \frac{1}{\Delta x \Delta y} \int_{x_{i-1/2}}^{x_{i+1/2}} \int_{y_{j-1/2}}^{y_{j+1/2}} \mathbf{H_a}\left(\mathbf{U}\left(x, y, z_{k\pm1/2}, t\right)\right) dzdy. \tag{3.78}$$

We have defined a left and a right advective flux (in each direction) for each computational cell that, together with an explicit time integration method, allow us to compute the conservative variables at each time step $\Delta t = t^{n+1} - t^{n}$. The original Godunov method takes a constant value of the conserved variable for the whole computational cell defining a local Riemann Problem at each intercell boundary. Note that, down to this point, the scheme is still purely mathematical and no numerical approximations have been performed. The advective fluxes require the solution of the local RP defined as $RP\left(\mathbf{U}_i^n, \mathbf{U}_{i+1}^n\right)$ for the $\overrightarrow{i}$ direction which can be written as

$$\mathbf{U}_{i+1/2}^n\left(x/t\right), \tag{3.79}$$

where $x/t = 0$. For a constant cell data distribution, the local RP is defined as shown in Figure 3.2.

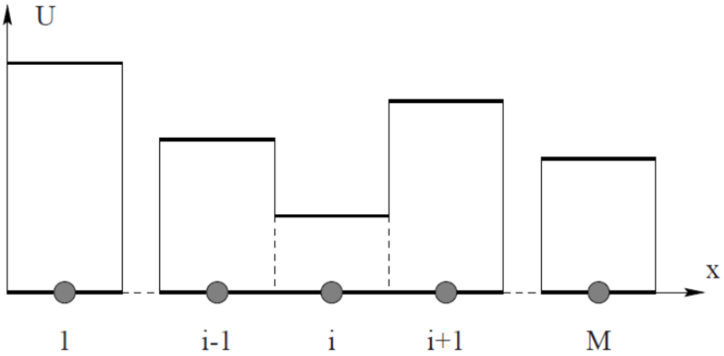

Figure 3.2: Constant cell data distribution defining the local RP at the each cell interface [6].

3.2.1.1 Riemann Solvers

The method developed by Godunov accounted for the exact solution of the local RP. As can be observed in Figure 3.3, the exact solution is composed by many possible wave patterns.

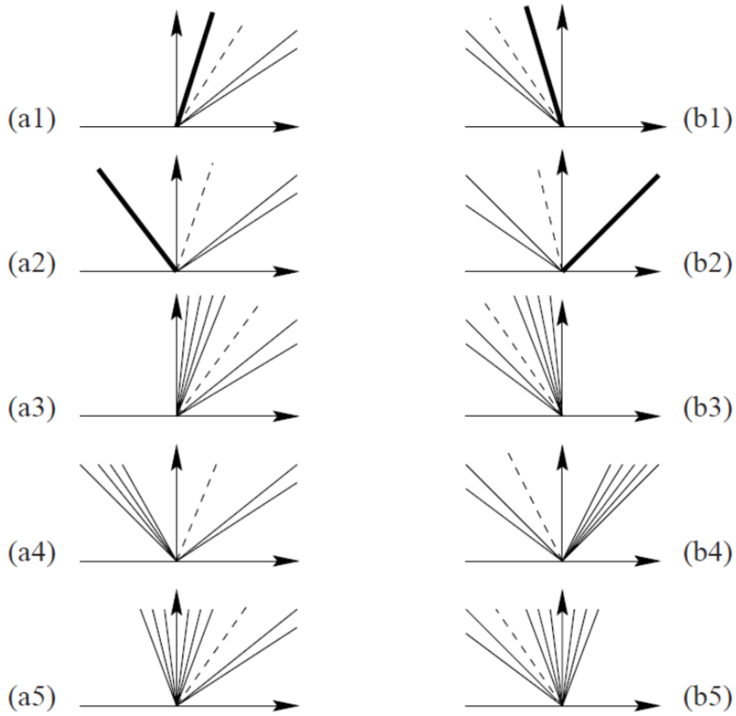

Figure 3.3: Exact RP possible wave pattern solutions arising at each cell interface. a) Positive wave speeds. b) Negative wave speeds [6].

In the figure above, the fan expansion represents a rarefaction expansion wave (EW), the discontinuous line is a contact surface (CS), the continuous highlighted line is a shock wave (SW) and, finally, a pair of two rays is an unknown wave type. The exact RP solution can be computationally expensive and, for most applications, an approximate solution can yield to very accurate results as well.

For the present study, the HLL, the Rusanov and HLLC approximate Riemann solvers have been considered. The following information has been extracted from reference [6].

HLL

The HLL solver approximates the solution into a two-wave pattern (SW-SW) which separates the space-time domain in 3 different states and allows to directly compute the numerical intercell flux for a given wave speed of the shock waves. These states are the Left region (L), the Start region (*) (or the HLL region for this solver) and the Right region (R).

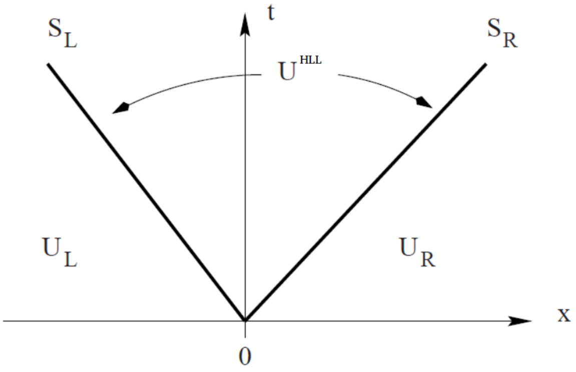

Figure 3.4: HLL approximate wave pattern solution [6].

The solution of the local RP in the $\overrightarrow{i}$ direction is given by

$$\mathbf{U}^n_{i+1/2}(0) = \begin{cases} \mathbf{U}_L & 0 < S_L \\ \mathbf{U}^{HLL} & S_L < 0 < S_R \\ \mathbf{U}_R & S_R < 0 \end{cases}, \tag{3.80}$$

and the numerical intercell flux can be computed as

$$\mathbf{F}^{HLL}_{i+1/2} = \begin{cases} \mathbf{F}_L & 0 < S_L \\ \mathbf{F}^{HLL} & S_L < 0 < S_R \\ \mathbf{F}_R & S_R < 0 \end{cases}, \tag{3.81}$$

where,

$$\mathbf{F}^{HLL} = \frac{S_R \mathbf{F}_L - S_L \mathbf{F}_R + S_L S_R (\mathbf{U}_R - \mathbf{U}_L)}{S_R - S_L}. \tag{3.82}$$

This relation above is derived from the Rankine-Hugoniot condition across any of the SW and the *consistency condition* as derived in [6, p. 319]. Finally, the left and the right wave speeds are given by the following relations

$$S_L = \min\left(u_L - a_L, u_R - a_R\right), \qquad S_R = \max\left(u_L + a_L, u_R + a_R\right). \tag{3.83}$$

Note that more complex relations involving average of the eigenvalues can be used as well, although they have not been implemented for the present study.

Rusanov

The Rusanov approximate Riemann solver is a particular case of the HLL solver for which a positive wave speed is captured beforehand as

$$S^+ = \max\left(\left|u_L - a_L\right|, \left|u_R - a_R\right|, \left|u_L + a_L\right|, \left|u_R + a_R\right|\right), \tag{3.84}$$

and the numerical flux is then computed as

$$\mathbf{F}_{i+1/2}^{RUS} = \frac{1}{2}\left(\mathbf{F}_L + \mathbf{F}_R\right) - \frac{1}{2}S^+\left(\mathbf{U}_L - \mathbf{U}_R\right). \tag{3.85}$$

HLLC

The HLLC solver is an improved version of the HLL solver which introduces another wave that separates the Star region in two different states yielding to a solution of 4 possible states.

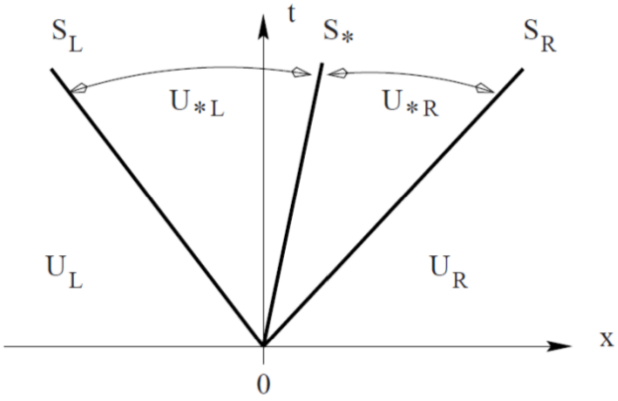

Figure 3.5: HLLC approximate wave pattern solution [6].

Mathematically, this is described as

$$\mathbf{U}_{i+1/2}^{n}(0) = \begin{cases} \mathbf{U}_L & 0 < S_L \\ \mathbf{U}_{*L} & S_L < 0 < S_* \\ \mathbf{U}_{*R} & S_* < 0 < S_R \\ \mathbf{U}_R & S_R < 0 \end{cases}. \tag{3.86}$$

The numerical intercell flux can be computed as

$$\mathbf{F}_{i+1/2}^{HLLC} = \begin{cases} \mathbf{F}_L & 0 < S_L \\ \mathbf{F}_{*L} & S_L < 0 < S_* \\ \mathbf{F}_{*R} & S_* < 0 < S_R \\ \mathbf{F}_R & S_R < 0 \end{cases}, \tag{3.87}$$

where the Left Star and the Right Star fluxes are computed using the intermediate vectors of conserved variables, $\mathbf{U}_{*L}$ and $\mathbf{U}_{*R}$, obtained again through the Rankine-Hugoniot condition written as

$$\mathbf{F}_{*K} = \mathbf{F}_K + S_K\left(\mathbf{U}_{*K} - \mathbf{U}_K\right), \tag{3.88}$$

and,

$$\mathbf{U}_{*K} = \rho_K\left(\frac{S_K - u_K}{S_K - S_*}\right)\begin{bmatrix} 1 \\ S_* \\ v_K \\ w_K \\ \frac{E_K}{\rho_K} + (S_* - u_K)\left[S_* + \frac{p_K}{\rho_K(S_K - u_K)}\right] \end{bmatrix}, \tag{3.89}$$

where K is the nomenclature for R or L, and S_* is the wave speed of the star region computed as

$$S_* = \frac{p_R - p_L + \rho_L u_L\left(S_L - u_L\right) - \rho_R u_R\left(S_R - u_R\right)}{\rho_L\left(S_L - u_L\right) - \rho_R\left(S_R - u_R\right)}. \tag{3.90}$$

The left and right wave speeds, S_L and S_R, are computed as in eq. 3.83. With this, the solution for problems involving contact surfaces is notably improved with respect to the HLL solver.

3.2.2 Reconstruction Schemes

In order to improve the accuracy of the Godunov-type method, different reconstruction schemes have been used. Considering an arbitrary discretised variable ϕ_i just for the stream-wise direction (i) (the procedure is analogous for other directions), the 1$^{\text{st}}$-order interpolation (as originally proposed by Godunov) of the left (L) and right (R) values at the intercell face $i+1/2$ is written as [65]

$$\phi^L_{i+1/2} = \phi_i, \qquad \phi^R_{i+1/2} = \phi_{i+1}. \tag{3.91}$$

The 2$^{\text{nd}}$-order interpolation is

$$\phi^L_{i+1/2} = \frac{3}{2}\phi_i - \frac{1}{2}\phi_{i-1}, \qquad \phi^R_{i+1/2} = \frac{3}{2}\phi_{i+1} - \frac{1}{2}\phi_{i+2}. \tag{3.92}$$

The 3$^{\text{rd}}$-order interpolation is

$$\phi^L_{i+1/2} = \frac{5}{6}\phi_i - \frac{1}{6}\phi_{i-1} + \frac{1}{3}\phi_{i+1}, \qquad \phi^R_{i+1/2} = \frac{5}{6}\phi_{i+1} - \frac{1}{6}\phi_{i+2} + \frac{1}{3}\phi_i. \tag{3.93}$$

Because of the well-known Godunov theorem, the previous high-order schemes will produce spurious oscillations close to sharp discontinuities. Therefore, different high-order TVD reconstruction schemes have been considered to increase the accuracy avoiding the oscillatory behaviour. TVD schemes ensure that no new local extrema is generated. So, being $\phi^n = \{\phi^n_i\}$ a mesh function, its Total Variation (TV) is

$$TV(u^n) = \sum_{-\infty}^{+\infty} \left|\phi^n_{i+1} - \phi^n_i\right|, \tag{3.94}$$

and a TVD scheme is

$$TV(\phi^{n+1}) \leq TV(\phi^n), \quad \forall n. \tag{3.95}$$

With this, the following properties are guaranteed when using high-order TVD schemes [64]:

- The smooth parts of the solution are at least 2$^{\text{nd}}$-order accurate,
- Sharp discontinuities are captured with a high resolution,
- Spurious oscillations are eliminated of the solution, even close to sharp discontinuities,
- Grid refinement yields to the true solution.

Therefore, high-order TVD schemes are a good choice for capturing shock waves, thus used in the present study.

3.2.2.1 MUSCL-type TVD Schemes

MUSCL-type reconstruction schemes using TVD procedures allow to obtain high-order schemes free of spurious oscillations. The interpolation of this method can be piece-wise linear as well as piece-wise quadratic among others. For the present study, the piece-wise linear approach is considered. The graphical representation of this scheme can be observed in the figures below,

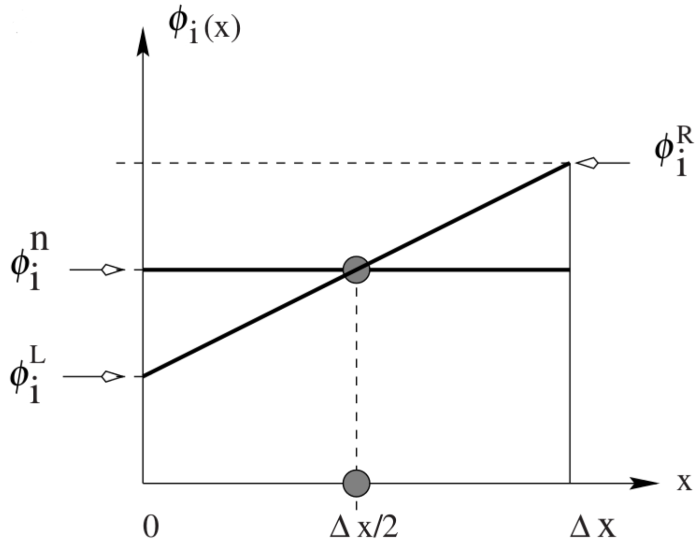

Figure 3.6: Piece-wise linear MUSCL reconstruction for a I_i cell. u_i^L and u_i^R are the values extrapolated at the left and right faces respectively of the I_i cell [6].

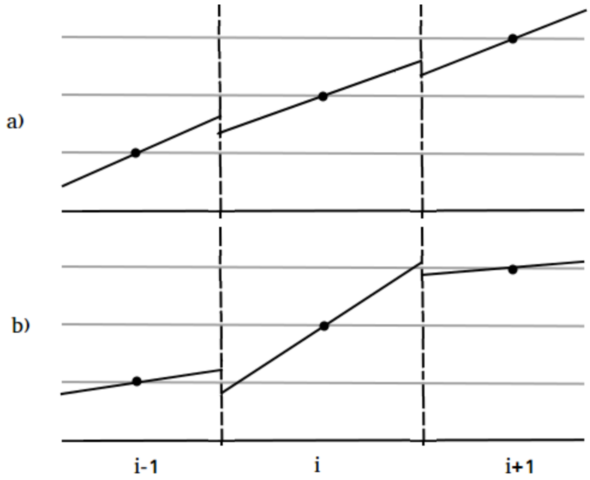

Figure 3.7: Piece-wise linear reconstruction using a monotone scheme (a) and a non-monotone scheme (b). Note that the monotone scheme keeps the interpolated values within the cell averaged values of the neighbour cells [8].

Mathematically, the left and the right values at the $i-1/2$ face are written as [6]

$$\phi_i^L = \phi_i^n - \frac{1}{2}\Delta_i, \qquad \phi_{i-1}^R = \phi_{i-1}^n + \frac{1}{2}\Delta_{i-1}, \tag{3.96}$$

where

$$\Delta_i = \frac{1}{2}(1+\omega)\Delta\phi_{i-1/2} + \frac{1}{2}(1-\omega)\Delta\phi_{i+1/2}, \tag{3.97}$$

$$\Delta_{i-1} = \frac{1}{2}(1+\omega)\Delta\phi_{i-3/2} + \frac{1}{2}(1-\omega)\Delta\phi_{i-1/2}, \tag{3.98}$$

where ω is a parameter contained between $[-1,1]$ that selects a backwards, central or forwards difference with $-1,0,1$ respectively and that can yield to a unique 3^{rd}-order scheme for $\omega = 1/3$. Jumps between neighbour cells are computed as

$$\Delta\phi_{i+1/2} = \phi_{i+1} - \phi_i, \tag{3.99}$$

$$\Delta\phi_{i-1/2} = \phi_i - \phi_{i-1}, \tag{3.100}$$

$$\Delta\phi_{i-3/2} = \phi_{i-2} - \phi_{i-1}. \tag{3.101}$$

The described reconstruction scheme is not TVD unless a slope limiter is incorporated as follows

$$\phi_i^L = \phi_i^n - \frac{1}{2}\bar{\Delta}_i, \qquad \phi_{i-1}^R = \phi_{i-1}^n + \frac{1}{2}\bar{\Delta}_{i-1}, \tag{3.102}$$

where

$$\overline{\Delta}_i = \xi_i \Delta_i, \qquad \overline{\Delta}_{i-1} = \xi_{i-1} \Delta_{i-1}, \tag{3.103}$$

being ξ_i the function defining the TVD region for the slope limiter.

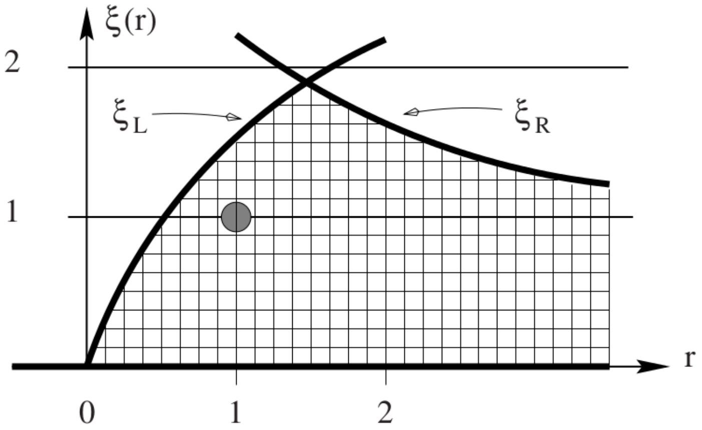

Figure 3.8: Slope limiters TVD region defined by $\xi\,(r)$ [6]

The $\xi_{i,L}\,(r)$ and $\xi_{i,R}\,(r)$ functions defining ξ_i are computed as

$$\xi_{i,L}\,(r) = \frac{2\beta_{i-1/2} r_i}{1-\omega+(1+\omega)\,r_i}, \tag{3.104}$$

$$\xi_{i,R}\,(r) = \frac{2\beta_{i+1/2}}{1-\omega+(1+\omega)\,r_i}, \tag{3.105}$$

where

$$r_i = \frac{\Delta\phi_{i-1/2}}{\Delta\phi_{i+1/2}}. \tag{3.106}$$

Different TVD slope limiters can be selected. Figure 3.9 illustrates the behaviour of some conventional slope limiters.

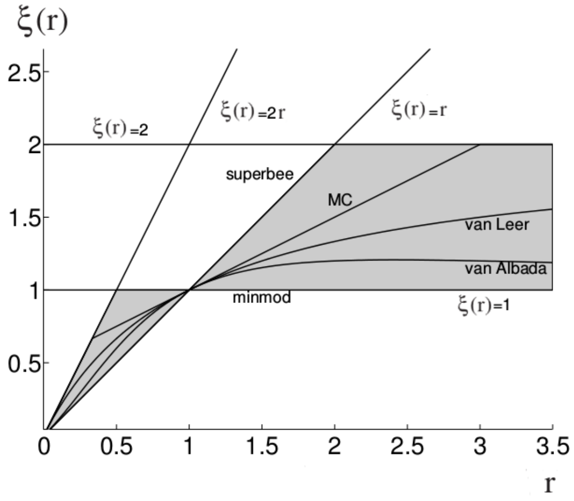

Figure 3.9: Conventional limiters functions (Sweby's diagram) [9].

For the present study, the following slope limiters have been considered:

- Minmod

$$\xi_i(r) = \begin{cases} 0 & r \leq 0 \\ r & 0 \leq r \leq 1 \\ \min\{1, \xi_{i,R}(r)\} & r \geq 1 \end{cases}, \tag{3.107}$$

- van Leer

$$\xi_i(r) = \begin{cases} 0 & r \leq 0 \\ \min\left\{\frac{2r}{1+r}, \xi_{i,R}(r)\right\} & r \geq 0 \end{cases}, \tag{3.108}$$

- van Albada

$$\xi_i(r) = \begin{cases} 0 & r \leq 0 \\ \min\left\{\frac{r(1+r)}{1+r^2}, \xi_{i,R}(r)\right\} & r \geq 0 \end{cases}, \tag{3.109}$$

- Superbee

$$\xi_i(r) = \begin{cases} 0 & r \leq 0 \\ 2r & 0 \leq r \leq 0.5 \\ 1 & 0.5 \leq r \leq 1 \\ \min\{r, \xi_{i,R}(r), 2\} & r \geq 1 \end{cases}. \tag{3.110}$$

3.2.2.2 WENO Schemes

Several finite-volume Weighted Essentially Non-Oscillatory (WENO) schemes have been considered from the 5th to the 11th-order of spatial accuracy. The WENO5 scheme has been implemented as proposed by V. A. Titarev *et al.* [22] whereas higher orders have been implemented as described by D. S. Balsara *et al.* [66]. In fact, schemes proposed by Balsara are monotonicity preserving WENO (MPWENO) since the monotonicity preserving bounds described by A. Suresh *et al.* [67] are incorporated. Summarising, the following schemes have been introduced to the in-house code: WENO5, MPWENO7, MPWENO9 and MPWENO11.

In general terms, high-order accuracy is reached at the smooth parts of the solution whereas close to sharp discontinuities the scheme switches to lower accurate interpolations in order to avoid generating spurious oscillations. WENO schemes are designed as follows. To construct a $(2r-1)^{\text{th}}$-order scheme, r stencils need to be considered which are referred as $S_{i,k}$ being $k = 0, ..., r-1$ and can be written as

$$S_{i,k} = (x_{i+k-r+1}, x_{i+k-r+2}, ..., x_{i+k}) \,. \tag{3.111}$$

Each stencil is defined with a smoothness indicator $\beta_k^{(r)}$ (note that for this entire section, the r superscript does not refer to a power but to the order of the scheme). When these indicators point out a smooth solution, a convex combination of each of the r stencils yield to the $(2r-1)^{\text{th}}$ interpolation order. The reconstruction of the left value at the $i+1/2$ face is given by the following expression

$$\phi_{i+1/2}^{L} = \sum_{k=0}^{r-1} \omega_k^{(r)} q_k^{(r)}, \tag{3.112}$$

where $\omega_k^{(r)}$ are the non-linear WENO weights and $q_k^{(r)}$ is the extrapolated average value from the k^{th} stencil in $S_{i,k}$. The $\omega_k^{(r)}$ term is defined as

$$\omega_k^{(r)} = \frac{\alpha_k^{(r)}}{\sum_{k=0}^{r-1} \alpha_k^{(r)}}, \tag{3.113}$$

$$\alpha_k^{(r)} = \frac{C_k^{(r)}}{\left(\varepsilon + \beta_k^{(r)}\right)^p}, \tag{3.114}$$

being $C_k^{(r)}$ the optimal weights, ε a very small parameter to avoid the denominator to be 0 and (usually) $p = 2$. The $q_k^{(r)}$ term is defined as

$$q_k^{(r)} = \sum_{n=1}^{r} a_{k,n}^{(r)} \phi_{i+k-r+n}, \tag{3.115}$$

where $a_{k,n}^{(r)}$ are the coefficients of each of the k^{th} stencil points $\phi_{i+k-r+n}$ in $S_{i,k}$. Next, the MPWENO7 ($r = 4$) scheme is detailed [66]. For the reconstruction of $\phi_{i+1/2}^{L}$, the smoothness indicators are defined as

$$\begin{aligned} \beta_0^{(4)} &= \phi_{i-3}\left(547\phi_{i-3} - 3882\phi_{i-2} + 4642\phi_{i-1} - 1854\phi_i\right) + \\ &+ \phi_{i-2}\left(7043\phi_{i-2} - 17246\phi_{i-1} + 7042\phi_i\right) + \\ &+ \phi_{i-1}\left(11003\phi_{i-1} - 9402\phi_i\right) + 2107\phi_i^2, \end{aligned} \tag{3.116}$$

$$\begin{aligned} \beta_1^{(4)} &= \phi_{i-2}\left(267\phi_{i-2} - 1642\phi_{i-1} + 1602\phi_i - 494\phi_{i+1}\right) + \\ &\phi_{i-1}\left(2843\phi_{i-1} - 5966\phi_i + 1922\phi_{i+1}\right) + \\ &+ \phi_i\left(3443\phi_i - 2522\phi_{i+1}\right) + 547\phi_{i+1}^2, \end{aligned} \tag{3.117}$$

$$\begin{aligned} \beta_2^{(4)} &= \phi_{i-1}\left(547\phi_{i-1} - 2522\phi_i + 1922\phi_{i+1} - 494\phi_{i+2}\right) + \\ &\phi_i\left(3443\phi_i - 5966\phi_{i+1} + 1602\phi_{i+2}\right) + \\ &+ \phi_{i+1}\left(2843\phi_{i+1} - 1642\phi_{i+2}\right) + 267\phi_{i+2}^2, \end{aligned} \tag{3.118}$$

$$\begin{aligned} \beta_3^{(4)} &= \phi_i\left(2107\phi_i - 9402\phi_{i+1} + 7042\phi_{i+2} - 1854\phi_{i+3}\right) + \\ &\phi_{i+1}\left(11003\phi_{i+1} - 17246\phi_{i+2} + 4642\phi_{i+3}\right) + \\ &+ \phi_{i+2}\left(7043\phi_{i+2} - 3882\phi_{i+3}\right) + 547\phi_{i+3}^2. \end{aligned} \tag{3.119}$$

The optimal weights are

$$C_0^{(4)} = \frac{1}{35}, \quad C_1^{(4)} = \frac{12}{35}, \quad C_2^{(4)} = \frac{18}{35}, \quad C_3^{(4)} = \frac{4}{35}. \tag{3.120}$$

The $\omega_k^{(r)}$ and $\alpha_k^{(r)}$ coefficients are computed as

$$\omega_0^{(4)} = \frac{\alpha_0^{(4)}}{\alpha_0^{(4)} + \alpha_1^{(4)} + \alpha_2^{(4)} + \alpha_3^{(4)}}, \tag{3.121}$$

$$\omega_1^{(4)} = \frac{\alpha_1^{(4)}}{\alpha_0^{(4)} + \alpha_1^{(4)} + \alpha_2^{(4)} + \alpha_3^{(4)}}, \tag{3.122}$$

$$\omega_2^{(4)} = \frac{\alpha_2^{(4)}}{\alpha_0^{(4)} + \alpha_1^{(4)} + \alpha_2^{(4)} + \alpha_3^{(4)}}, \tag{3.123}$$

$$\omega_3^{(4)} = \frac{\alpha_3^{(4)}}{\alpha_0^{(4)} + \alpha_1^{(4)} + \alpha_2^{(4)} + \alpha_3^{(4)}}, \tag{3.124}$$

$$\alpha_0^{(4)} = \frac{C_0^{(4)}}{\left(\varepsilon + \beta_0^{(4)}\right)^2}, \quad \alpha_1^{(4)} = \frac{C_1^{(4)}}{\left(\varepsilon + \beta_1^{(4)}\right)^2}, \tag{3.125}$$

$$\alpha_2^{(4)} = \frac{C_2^{(4)}}{\left(\varepsilon + \beta_2^{(4)}\right)^2}, \quad \alpha_3^{(4)} = \frac{C_3^{(4)}}{\left(\varepsilon + \beta_3^{(4)}\right)^2}. \tag{3.126}$$

The extrapolated average values are

$$q_0^{(4)} = a_{0,1}^{(4)}\phi_{i-3} + a_{0,2}^{(4)}\phi_{i-2} + a_{0,3}^{(4)}\phi_{i-1} + a_{0,4}^{(4)}\phi_i, \tag{3.127}$$

$$q_1^{(4)} = a_{1,1}^{(4)}\phi_{i-2} + a_{1,2}^{(4)}\phi_{i-1} + a_{1,3}^{(4)}\phi_i + a_{1,4}^{(4)}\phi_{i+1}, \tag{3.128}$$

$$q_2^{(4)} = a_{2,1}^{(4)}\phi_{i-1} + a_{2,2}^{(4)}\phi_i + a_{2,3}^{(4)}\phi_{i+1} + a_{2,4}^{(4)}\phi_{i+2}, \tag{3.129}$$

$$q_3^{(4)} = a_{3,1}^{(4)}\phi_i + a_{3,2}^{(4)}\phi_{i+1} + a_{3,3}^{(4)}\phi_{i+2} + a_{3,4}^{(4)}\phi_{i+3}, \tag{3.130}$$

where the $a_{k,n}^{(4)}$ coefficients are

$a_{k,n}^{(4)}$	$n=1$	$n=2$	$n=3$	$n=4$
$k=0$	-1/4	13/12	-23/12	25/12
$k=1$	1/12	-5/12	13/12	1/4
$k=2$	-1/12	7/12	7/12	-1/12
$k=3$	1/4	13/12	-5/12	1/12

Table 3.1: $a_{k,n}^{(r)}$ coefficients for $r=4$.

Finally, the left value at the $i+1/2$ face is written as

$$\phi_{i+1/2}^{L}=\omega_0^{(4)}q_0^{(4)}+\omega_1^{(4)}q_1^{(4)}+\omega_2^{(4)}q_2^{(4)}+\omega_3^{(4)}q_3^{(4)}. \tag{3.131}$$

The right value at the $i-1/2$ face, $u_{i-1/2}^{R}$, can be obtained by symmetry as showed in Appendix A.2.

3.2.3 Viscous Fluxes

The viscous fluxes have been computed by means of a FDM considering the averaged quantities at the cell-centred points. Therefore, the viscous terms of the N-S equations are added as a source terms when it comes to code implementation. Initially, a 2$^{\text{nd}}$-order central difference scheme was implemented. However, at a more advanced stage of the thesis, a forwards-backwards difference including the thermodynamic transport properties as a spatially dependent variables was considered (following [68]). The latter option avoids directly discretising 2$^{\text{nd}}$-order derivatives, proved to be computationally more stable and provided more accurate results than the 2$^{\text{nd}}$-order central difference scheme. For example, let us consider the following terms

$$\frac{\partial}{\partial x}\left(\kappa\frac{\partial T}{\partial x}\right), \tag{3.132}$$

$$\frac{\partial}{\partial x}\left[\mu\left(\frac{\partial u}{\partial y}+\frac{\partial v}{\partial x}\right)\right]. \tag{3.133}$$

A 2$^{\text{nd}}$-order central difference scheme excluding the thermal conductivity and the dynamic viscosity from the derivative yields to the discretisation below (in 2D Cartesian coordinates)

$$\frac{\partial}{\partial x}\left(\kappa\frac{\partial T}{\partial x}\right)\approx\kappa\frac{\partial^2 T}{\partial x^2}\approx\kappa_{ij}\frac{T_{i+1,j}-2T_{ij}+T_{i-1,j}}{\Delta x^2}, \tag{3.134}$$

$$\frac{\partial}{\partial x}\left[\mu\left(\frac{\partial u}{\partial y}+\frac{\partial v}{\partial x}\right)\right]\approx\mu\frac{\partial}{\partial x}\left(\frac{\partial u}{\partial y}+\frac{\partial v}{\partial x}\right)=\mu\left(\frac{\partial^2 u}{\partial x\partial y}+\frac{\partial^2 v}{\partial x^2}\right)\approx$$

$$\approx\mu_{ij}\frac{u_{i+1,j+1}-u_{i-1,j+1}-u_{i+1,j-1}+u_{i-1,j-1}}{4\Delta x\Delta y}+\mu_{ij}\frac{v_{i+1,j}-2v_{ij}+v_{i-1,j}}{\Delta x^2}. \tag{3.135}$$

Instead, the forwards-backwards difference including the thermodynamic properties in the derivative is written as

$$\frac{\partial}{\partial x}\left(\kappa\frac{\partial T}{\partial x}\right)\approx\frac{\kappa_{i+1,j}\frac{T_{i+1,j}-T_{ij}}{\Delta x}-\kappa_{i-1,j}\frac{T_{ij}-T_{i-1,j}}{\Delta x}}{\Delta x}=$$

$$=\frac{\kappa_{i+1,j}\left(T_{i+1,j}-T_{ij}\right)-\kappa_{i-1,j}\left(T_{ij}-T_{i-1,j}\right)}{\Delta x^2}, \tag{3.136}$$

$$\frac{\partial}{\partial x}\left[\mu\left(\frac{\partial u}{\partial y}+\frac{\partial v}{\partial x}\right)\right]=\frac{\partial}{\partial x}\left(\mu\frac{\partial u}{\partial y}\right)+\frac{\partial}{\partial x}\left(\mu\frac{\partial v}{\partial x}\right)\approx$$

$$\approx\frac{\mu_{i+1,j}\frac{u_{i+1,j+1}-u_{i+1,j}}{\Delta y}-\mu_{i-1,j}\frac{u_{i-1,j}-u_{i-1,j-1}}{\Delta y}}{\Delta x}+\frac{\mu_{i+1,j}\frac{v_{i+1,j}-v_{ij}}{\Delta x}-\mu_{i-1,j}\frac{v_{ij}-v_{i-1,j}}{\Delta x}}{\Delta x}=$$

$$=\frac{\mu_{i+1,j}\left(u_{i+1,j+1}-u_{i+1,j}\right)-\mu_{i-1,j}\left(u_{i-1,j}-u_{i-1,j-1}\right)}{\Delta x\Delta y}+$$

$$+\frac{\mu_{i+1,j}\left(v_{i+1,j}-v_{ij}\right)-\mu_{i-1,j}\left(v_{ij}-v_{i-1,j}\right)}{\Delta x^2}. \tag{3.137}$$

The remaining discretised viscous terms in the 2D Cartesian coordinate system can be consulted in Appendix A.1.

3.2.4 Time Integration Methods

Considering the Godunov scheme from eq. 3.74, let us rewrite it as an Ordinary Differential Equation (ODE) given as

$$\frac{d}{dt}\mathbf{U}_{ijk}(t)=\mathbf{L}\left(\mathbf{U}_{ijk}\right), \tag{3.138}$$

where $\mathbf{L}\left(\mathbf{U}_{ijk}\right)$ is an spatial operator applied to the advective fluxes, the viscous fluxes and the source terms, discretising them as described in the previous sections and can be expressed as

$$\mathbf{L}\left(\mathbf{U}_{ijk}\right)=\frac{1}{\Delta x}\left[\left(\mathbf{F_a}\right)_{i-1/2,jk}-\left(\mathbf{F_a}\right)_{i+1/2,jk}\right]+\frac{1}{\Delta y}\left[\left(\mathbf{G_a}\right)_{i,j-1/2,k}-\left(\mathbf{G_a}\right)_{i,j+1/2k}\right]+$$

$$+\frac{1}{\Delta z}\left[(\mathbf{H_a})_{ij,k-1/2}-(\mathbf{H_a})_{ij,k+1/2}\right]+(\mathbf{F_v})_{ijk}+(\mathbf{G_v})_{ijk}+(\mathbf{H_v})_{ijk}+\mathbf{S}_{ijk}. \tag{3.139}$$

With this, different explicit time stepping methods have been implemented. First, the well-known 1st-order forward Euler method is considered and can be written as

$$\mathbf{U}^{n+1}_{ijk}=\mathbf{U}^{n}_{ijk}+\Delta t\mathbf{L}\left(\mathbf{U}^{n}_{ijk}\right). \tag{3.140}$$

Second, Runge-Kutta -type (RK) methods are used as a high-order time integration schemes. The generalised form of this method to step from t^n to $t^{n+1}$is described below [69, 70, 71]

$$\begin{aligned}\mathbf{U}^{(0)}_{ijk}&=\mathbf{U}^{n}_{ijk}\\ \mathbf{U}^{(s)}_{ijk}&=\sum_{l=0}^{s-1}\left[\alpha_{sl}\mathbf{U}^{(l)}_{ijk}+\Delta t\beta_{sl}\mathbf{L}\left(\mathbf{U}^{(l)}_{ijk}\right)\right],\quad s=1,...,m,\\ \mathbf{U}^{n+1}_{ijk}&=\mathbf{U}^{(m)}_{ijk}\end{aligned} \tag{3.141}$$

where α_{sl} and β_{sl} are non-negative coefficients to obtain a convex combination of Euler forward operators. The scheme in eq. 3.141 is TVD (also known as Strong Stability preserving (SSP) to refer to time integration methods) only for the following CFL condition

$$c=\min_{sl}\frac{\alpha_{sl}}{\beta_{sl}}. \tag{3.142}$$

With this, the following optimal RK TVD methods are considered:

RK2TVD

$$\begin{aligned}\mathbf{U}^{(1)}_{ijk}&=\mathbf{U}^{n}_{ijk}+\Delta t\mathbf{L}\left(\mathbf{U}^{n}_{ijk}\right)\\ \mathbf{U}^{n+1}_{ijk}&=\frac{1}{2}\mathbf{U}^{n}_{ijk}+\frac{1}{2}\mathbf{U}^{(1)}_{ijk}+\frac{1}{2}\Delta t\mathbf{L}\left(\mathbf{U}^{(1)}_{ijk}\right).\end{aligned} \tag{3.143}$$

RK3TVD

$$\begin{aligned}\mathbf{U}^{(1)}_{ijk}&=\mathbf{U}^{n}_{ijk}+\Delta t\mathbf{L}\left(\mathbf{U}^{n}_{ijk}\right)\\ \mathbf{U}^{(2)}_{ijk}&=\frac{3}{4}\mathbf{U}^{n}_{ijk}+\frac{1}{4}\mathbf{U}^{(1)}_{ijk}+\frac{1}{4}\Delta t\mathbf{L}\left(\mathbf{U}^{(1)}_{ijk}\right).\\ \mathbf{U}^{n+1}_{ijk}&=\frac{1}{2}\mathbf{U}^{n}_{ijk}+\frac{2}{3}\mathbf{U}^{(1)}_{ijk}+\frac{2}{3}\Delta t\mathbf{L}\left(\mathbf{U}^{(2)}_{ijk}\right)\end{aligned} \tag{3.144}$$

Finally, a 4$^{\text{th}}$-order RK (non-TVD) method has been implemented as well and is written as follows

$$
\begin{aligned}
&\mathbf{U}_{ijk}^{(1)} = \mathbf{U}_{ijk}^{n} + 0.391752226571890\Delta t\mathbf{L}\left(\mathbf{U}_{ijk}^{n}\right)\\
&\mathbf{U}_{ijk}^{(2)} = 0.444370493651235\mathbf{U}_{ijk}^{n} + 0.555629506348765\mathbf{U}_{ijk}^{(1)} +\\
&+0.368410593050371\Delta t\mathbf{L}\left(\mathbf{U}_{ijk}^{(1)}\right)\\
&\mathbf{U}_{ijk}^{(3)} = 0.620101851488403\mathbf{U}_{ijk}^{n} + 0.379898148511597\mathbf{U}_{ijk}^{(2)} +\\
&+0.251891774271694\Delta t\mathbf{L}\left(\mathbf{U}_{ijk}^{(2)}\right)\\
&\mathbf{U}_{ijk}^{(4)} = 0.620101851488403\mathbf{U}_{ijk}^{n} + 0.379898148511597\mathbf{U}_{ijk}^{(3)} +\\
&+0.251891774271694\Delta t\mathbf{L}\left(\mathbf{U}_{ijk}^{(3)}\right)\\
&\mathbf{U}_{ijk}^{n+1} = 0.517231671970585\mathbf{U}_{ijk}^{(2)} + 0.096059710526147\mathbf{U}_{ijk}^{(3)} +\\
&+0.063692468666290\Delta t\mathbf{L}\left(\mathbf{U}_{ijk}^{(3)}\right) + 0.386708617503269\mathbf{U}_{ijk}^{(4)} +\\
&+0.226007483236906\Delta t\mathbf{L}\left(\mathbf{U}_{ijk}^{(4)}\right).
\end{aligned}
\tag{3.145}
$$

For the 4th TVD version with 4th stages, a negative value of β_{sl} is unavoidable. However, for 5th stages, a non-negative coefficient can be found. Both schemes can be found in [69] and [72] respectively.

3.2.4.1 Time Step

In order to compute a stable time step, the maximum wave speed present in the domain at a t^n time has to be taken into account. The time step is defined as [6]

$$
\Delta t = \min\left(\frac{c\Delta x}{S_{max,i}^{n}}, \frac{c\Delta y}{S_{max,j}^{n}}, \frac{c\Delta z}{S_{max,k}^{n}}\right), \tag{3.146}
$$

where c is the Courant number following the condition below

$$
0 < c \leq 1. \tag{3.147}
$$

The maximum wave speed can be computed as

$$
\begin{aligned}
S^n_{max,i} &= \min_i \left(\left| u^n_{ijk} \right| + a^n_{ijk} \right) \\
S^n_{max,j} &= \min_j \left(\left| v^n_{ijk} \right| + a^n_{ijk} \right), \\
S^n_{max,k} &= \min_k \left(\left| w^n_{ijk} \right| + a^n_{ijk} \right)
\end{aligned}
\tag{3.148}
$$

where a^n_{ijk} is the local speed of sound. Note that for cases as the shock tube problem, the maximum wave speed will account for the speed of sound at the initial state yielding to unstable time step values at the beginning of the simulation (since the initial velocities are 0). Because of this, it is recommended to use low Courant number values when running cases for which one is not well familiarised.

3.2.5 Boundary Conditions

Because of the FVM cell-centred data structure, values at boundaries cannot be directly enforced since no variables are stored there (on the contrary this would be possible for a node-centred FVM) . Therefore, storing a value at the boundary ghost cell ensures that an eventual extrapolation of the value at the physical boundary would yield to the correct boundary condition. By considering the following grid layout,

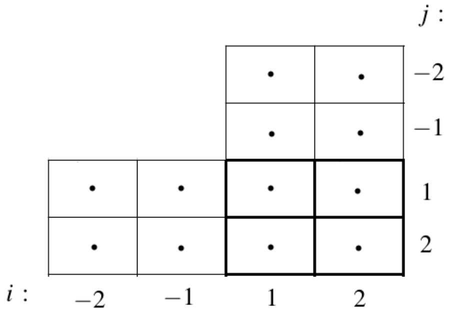

Figure 3.10: 2D cell-centred rectangular grid. Extrapolation of the boundary conditions.

The value at the left boundary is set extrapolating as

$$
\phi_{BC} = \frac{\phi_{-1} + \phi_1}{2}, \tag{3.149}
$$

$$
\phi_{-1} = 2\phi_{BC} - \phi_1, \tag{3.150}
$$

where ϕ_{BC} is the value of the boundary condition and ϕ_{-1} is the value that will be stored in the ghost cell. So, the previously described method to set the value at the boundary applies when a Dirichlet-type BC is required. For Neumann-type conditions, transmissive BCs are set copying the value of the physical cell to the ghost cell symmetrically.

With this, the boundary condition values at the left and right sides of the tube were taken from the initial states of the shock tube. An important question that arises here is how to enforce a temperature condition with in a data structure based in the conservative variables. This has been solved as follows. First, the temperature value required at the ghost cell that ensures the correct value at the boundary is computed as in eq. 3.150

$$T_{-1} = 2T_{wall} - T_1. \tag{3.151}$$

Then, the equation of state provides the correct value of the density at the ghost cell taking into account a transmissive behaviour of the pressure field at the ghost cells. This is can be expressed as

$$\rho_{-1} = \frac{p_1}{RT_{-1}}. \tag{3.152}$$

With this density, the conserved variables are computed as

$$\rho_{-1}u_{-1} = 2\left(\rho u\right)_{BC} - \rho_1 u_1, \tag{3.153}$$

$$\rho_{-1}v_{-1} = 2\left(\rho v\right)_{BC} - \rho_1 v_1, \tag{3.154}$$

$$\rho_{-1}w_{-1} = 2\left(\rho w\right)_{BC} - \rho_1 w_1, \tag{3.155}$$

$$E_{-1} = E_1. \tag{3.156}$$

One may note that this is not a totally consistent formulation. However, because of the data structure of the code, is a good solution to correctly set the BC of the temperature field at the walls. This was also a reason why the temperature transport equation was introduced to the equations system. With this equation, a correct definition of the temperature at the boundaries is achieved using 3.151.

To set a no-slip BC, the following terms are cancelled: $(\rho u)_{BC}$,$(\rho v)_{BC}$,$(\rho w)_{BC}$. For the slip BC (eq. 3.65), the BC value is computed as

$$\rho_{-1}u_{-1} = 2\rho_1 u_{slip} - \rho_1 u_1, \tag{3.157}$$

$$\rho_{-1}v_{-1} = -\rho_1 v_1, \tag{3.158}$$

$$\rho_{-1}w_{-1} = -\rho_1 w_1, \tag{3.159}$$

where the slip velocity is calculated as

$$u_{slip} = \frac{2-\sigma_v}{\sigma_v}\lambda_1\frac{u_2-u_1}{\Delta y}, \tag{3.160}$$

being λ_1 the local MFP defined as

$$\lambda_1 = \sqrt{\frac{\pi}{2}}\frac{\mu_1}{\sqrt{\rho_1 p_1}}. \tag{3.161}$$

Note that the stream-wise derivative of the temperature at the wall term in eq. 3.65 is neglected since an isothermal wall is considered. Regarding the temperature jump BC, now the T_{wall} in eq. 3.151 is substituted for the temperature obtained though the temperature jump BC, T_s, which can be written as

$$T_s = T_{wall} + \frac{2-\sigma_T}{\sigma_T}\frac{2\gamma}{\gamma+1}\frac{\lambda_1}{Pr_1}\frac{T_2-T_1}{\Delta y}, \tag{3.162}$$

being Pr_1 the local Prandtl number defined as

$$Pr_1 = \frac{(c_p)_1\,\mu_1}{\kappa_1}. \tag{3.163}$$

An analogous symmetrical procedure is carried for the remaining ghost cells (-2,...,-NGhostCells). As a final note, it is worth to mention that boundary conditions must be computed at each stage of the RK method, otherwise the simulation becomes unstable.

Chapter 4

Results and Discussions

4.1 One-Dimensional Euler Equations

The Sod shock tube test case has been used for validating the different numerical schemes implemented in the Minitube2D in-house code. This test case validates the Euler equations (no presence of viscous terms) for a 1D space. An analytical solution is possible under these condition which allows to check the behaviour of different Riemann solvers, reconstruction schemes and time integration methods for solutions containing sharp discontinuities. The Sod shock tube test case set up (initial state of both regions, output time and diaphragm position) is detailed below,

Sod Shock Tube	Driver (4)	Driven (1)
ρ	1.0	0.125
u	0.0	0.0
p	1.0	0.1
Output time	0.2	
Diaphragm position	0.5	
Dimensions	1.0	

Table 4.1: Sod shock tube test case details.

It should be noted that this is a dimensionless problem which only aims to assess the numerical methods, not the physics. Thus, the values of the variables seen in Table 4.1 are physically meaningless. Also, only the density profile is discussed since the three different waves (SW, CS and EW) can be observed and discussed for this flow variable.

4.1.1 Riemann Solvers

The Rusanov, HLL and HLLC approximate Riemann Solvers have been tested using the same grid size (100 cells) and time integration scheme (RK1) for a 1$^{\text{st}}$-order and a 3$^{\text{rd}}$-order reconstruction schemes.

The 1$^{\text{st}}$-order scheme results can be observed in Figure 4.1a. The discontinuities in the solution are not properly captured because of the high dissipation inherent in this scheme. Even tough, it is shown that all Riemann solvers perform in a similar way in the SW region but some differences arise on capturing the CS. The HLLC solver is the one that shows a better trend for the CS followed by the HLL solver and finally the Rusanov solver. These are in fact the expected results since the HLLC solver is actually an enhancement of the HLL solver for CS waves.

Regarding the 3$^{\text{rd}}$-order reconstruction scheme (4.1b), a better accuracy is observed in the smooth regions of the solution. However, spurious oscillations are appreciated at the vicinities of sharp discontinuities. As mentioned in previous chapters, using high-order non-TVD schemes generates these type of oscillations that can be observed in this figure. This is why MUSCL or WENO (and ENO) schemes are required if using high-order schemes in problems involving discontinuous solutions. Regarding the Riemann solvers, the HLL solver is the one showing more significant oscillations. Again, the HLLC solver is better than the other ones at capturing the CS and all of them perform in a similar way at the SW.

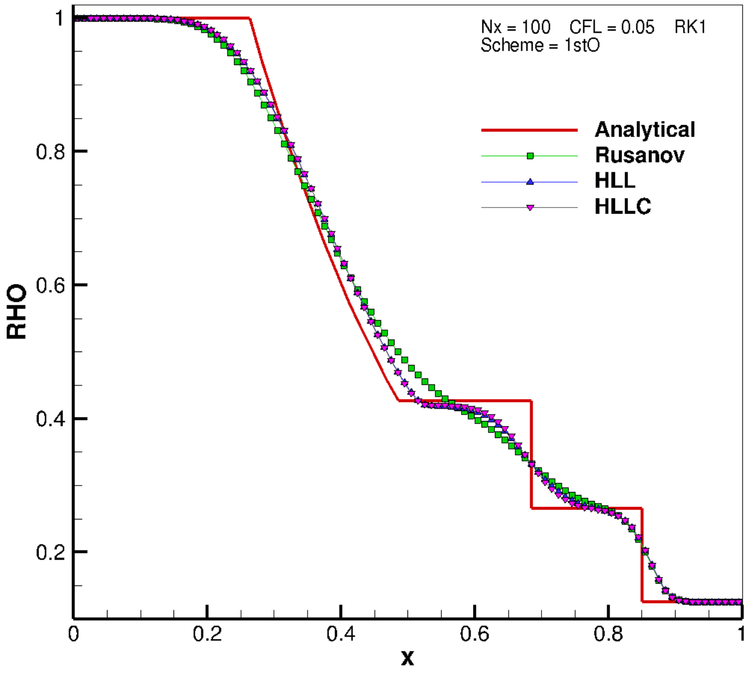

(a)

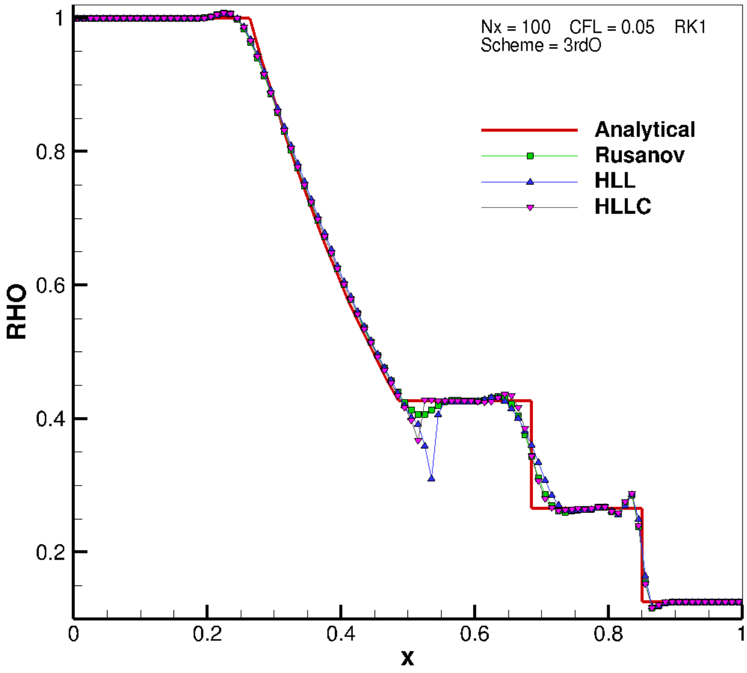

(b)

Figure 4.1: Riemann solvers performance using different reconstruction schemes. a) 1st-order. b) 3rd-order.

4.1.2 Reconstruction schemes

Once the HLLC Riemann solver has proved to be the better choice to capture the CS, different TVD high-order schemes are tested together with this Riemann solver using again 100 cells and the 1$^{\text{st}}$-order RK time integration method. First, the MUSCL2 scheme with different slope limiters can be observed at Figure 4.2a. Even though the spatial order of accuracy is lower than the 3$^{\text{rd}}$-order scheme, a notorious improvement can still be appreciated at the smooth part of the solution when compared to the 1$^{\text{st}}$-order scheme. Actually, this region is captured in a similar way as the 3$^{\text{rd}}$-order scheme does. The important fact comes close to the sharp discontinuities of the solution. It is shown a great improvement with respect to the 3$^{\text{rd}}$-order scheme by avoiding the oscillatory behaviour that high-order schemes generate close to sudden changes of the solution. The slope limiters implemented mitigate the oscillations by ensuring the TVD properties mentioned in the previous chapter. The superbee slope limiter is the one offering the best performance closely followed by the van Leer limiter. The van Albada and the minmod limiters are not as good as the previous ones for this solution since they are a bit more diffusive. The superbee limiter is known for sharpening the slopes too much since it applies the maximum steepening and the minimum limiting functions within the TVD region. Therefore, it performs better than the rest of the limiters since the analytical solution contains very sharp discontinuities.

The WENO reconstruction schemes (WENO5, MPWENO7, MPWENO9 and MPWENO11) analysis can be observed in Figure 4.2b. A very high accuracy can be appreciated at the smooth parts of the solution, being the MPWENO11 the more accurate scheme yielding to a remarkable difference with respect to the MUSCL2 scheme. Even though the solution is also less diffused at discontinuities, an important trend that can be observed is that as the scheme order increases it becomes more oscillatory in these regions. Regardless of the monotonicity preserving and the essentially non-oscillatory properties of the schemes, oscillations can be noted for the very high-order schemes. This fact is also observed in other works such as [73, p. 110]. As a matter of fact, it is important to highlight that these oscillations increase as the grid is refined. This can be observed at Figure 4.3, where the same simulation is performed now using 400 cells instead of 100. Note that at the vicinities of the CS, the overshoot is more significant than in Figure 4.2b. A way to overcome this issue is to increase the time discretisation order, since at the moment only the 1$^{\text{st}}$-order forward Euler method is used. Besides, Balsara [66] suggests that the reconstruction procedure should be performed for the primitive variables instead of the conservatives variables since the latter option might be unstable depending on the case. However, the data structure of the Minitube2D does not facilitate the reconstruction of primitives variables triggering, probably, part of the oscillatory behaviour.

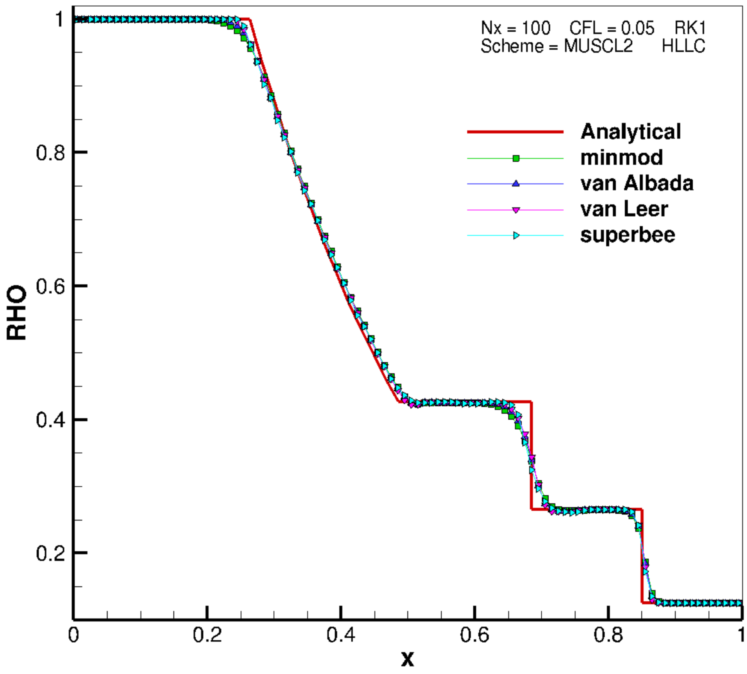

(a)

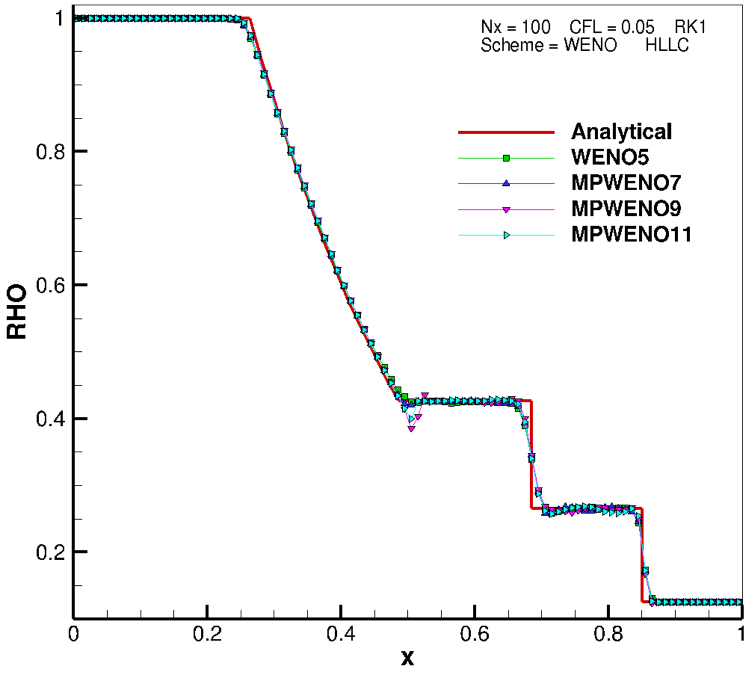

(b)

Figure 4.2: High-order TVD reconstruction schemes. a) MUSCL2. b) WENO.

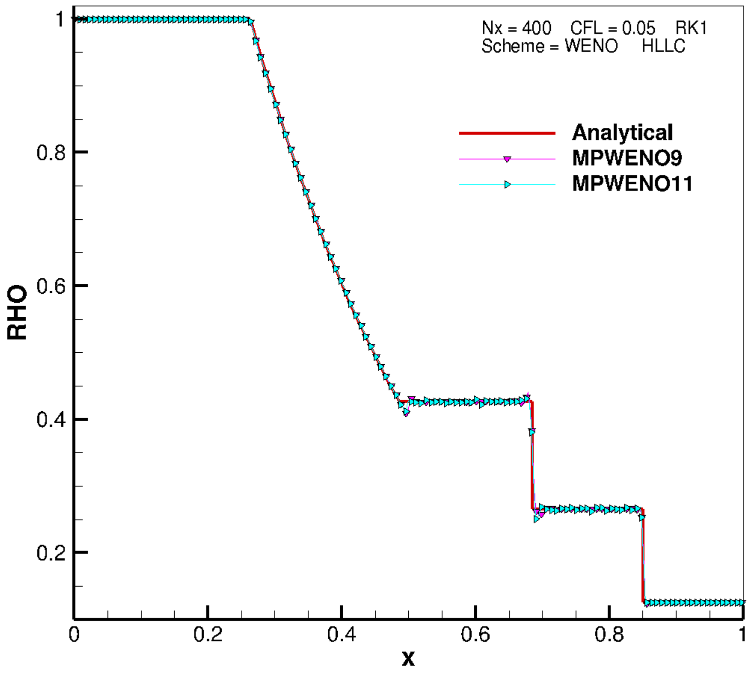

Figure 4.3: MPWENO9 and MPWENO11 in a 400 cells grid.

4.1.3 Time integration methods

In order to reduce the spurious oscillations of the very-high order schemes such as MPWENO9 and MPWENO11, different Runge-Kutta time integration methods have been implemented: RK2TVD, RK3TVD and RK4. The 2$^{\text{nd}}$ and 3$^{\text{rd}}$-order RK methods are TVD while the 4$^{\text{th}}$-order one is not. Results can be observed in Figure 4.4. Note that only the CS region of the solution is displayed, where most of the oscillations take place. It can be seen that high-order RK methods yield to reduced overshoots close to the CS being this the expected performance. However, no differences can be appreciated among the different high-order RK methods where a reduction of the oscillations should be noted at least from the RK2TVD to the RK3TVD method (not for RK4 since it is not TVD). The reason behind this trend is unclear.

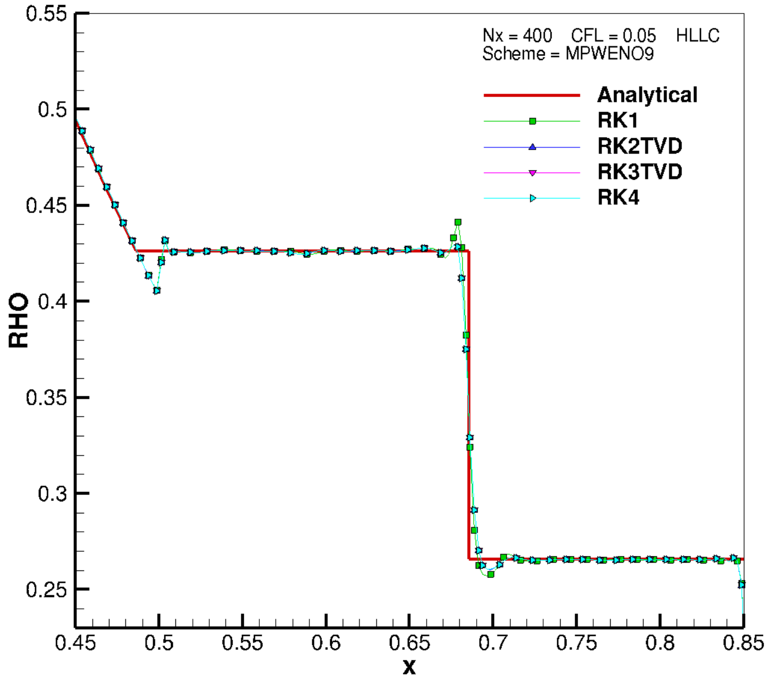

Figure 4.4: Several RK time integration methods using the MPWENO9 scheme in a 400 cells grid (CS region).

4.1.4 Grid convergence

The final validation for the 1D Euler equations consist of a grid convergence study. The WENO5 scheme together with the HLLC Riemann solver and the RK1 time integration method is used for different grid sizes, as can be shown in the Figure 4.5a. A grid refinement ratio of 2 is used from 50 to 800 cells. The grid convergence analysis of the MPWENO11 scheme using the RK3TVD method and the HLLC Riemann solver is performed as well in Figure 4.5b. For both schemes, a clear convergence to the true solution is appreciated as the grid gets refined, thus ensuring the last property of a TVD scheme exposed in the previous chapter. Note that the MPWENO11 reduced the oscillations with the grid refinement, contrary to what it has been previously stated. This is because now a high-order RK method is used thus reducing the spurious oscillations close to discontinuities. This allows the solution to converge easily to the analytical value as the grid is refined.

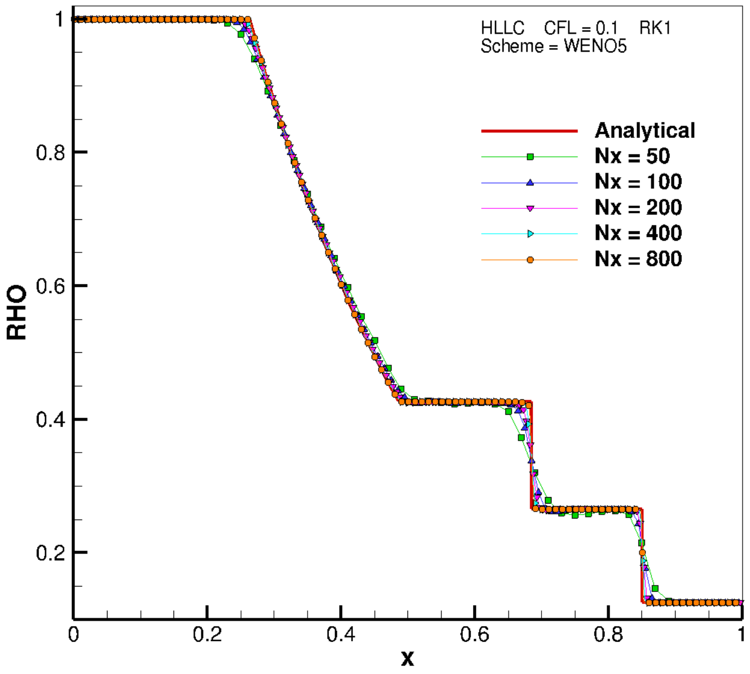

(a)

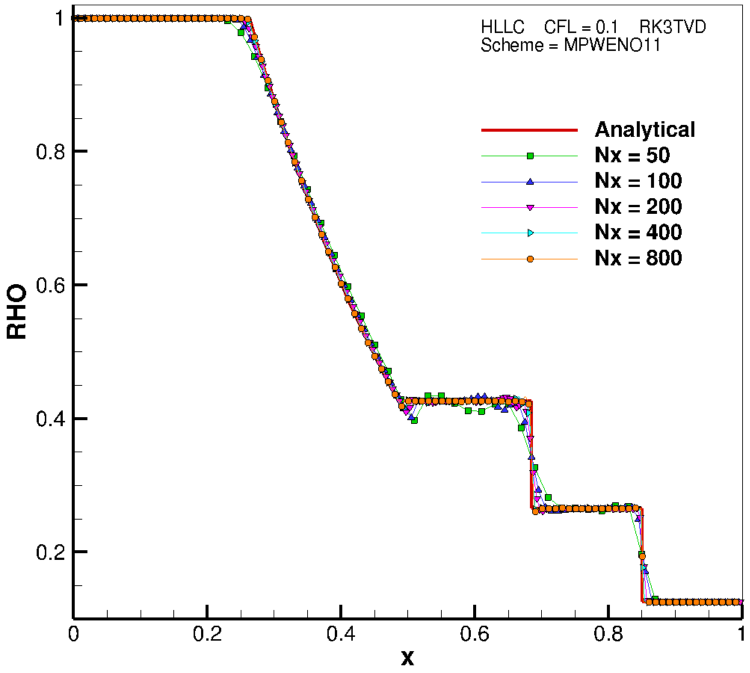

(b)

Figure 4.5: Grid convergence using 5 different grid sizes: 50, 100, 200, 400 and 800 cells. a) WENO5. b) MPWENO11.

4.2 One-Dimensional Navier-Stokes Equations

The experimental results from E. P. Muntz *et al.* [2] have been used as reference data to validate the 1D Navier-Stokes equations implemented in the Minitube2D in-house code. The experiment consists of an helium shock wave generated by a 8 cm shock holder in a low-density wind tunnel. The theoretical shock wave Mach number is $M_{th} = 1.59$. Using an electron beam fluorescent technique, the density and the temperature fields could be measured, the latter for both parallel and perpendicular directions of the flow. The set up of the experiment is detailed below,

	Driver (4)	Driven (1)
Material	Helium	Helium
ρ [kg/m^3]	3.50E-05	1.93E-05
u [m/s]	0.0	0.0
p [Pa]	18.46	6.43
Output time [μs]	4.0	
Dimensions [mm]	25.0×1.0	
Diaphragm position [mm]	13.875	

Table 4.2: Muntz's case experimental details.

The numerical results provided by Muntz are free from wall effects but retaining the diffusive terms generated by the axial gradient. This is why it can be used as a 1D N-S validation case. Also, since a weak shock is studied (thus developing a large shock thickness), the use of a continuum approach (N-S) shall be accurate enough even for micro scales [7]. The thermodynamic transport properties for the helium gas are shown in Table 4.3.

Specific gas constant, R [J/(kgK)]	2077.0
Specific heats ratio, γ [-]	1.667
Specific heat at constant pressure, c_p [J/(kgK)]	5188.0
Thermal conductivity, κ [W/(mK)]	see eq. 4.1
Sutherland's reference viscosity, μ_0 [kg/(ms)]	1.9E-05
Sutherland's reference temperature, T_0 [K]	273.15
Sutherland's temperature, S [K]	79.4

Table 4.3: Thermodynamic transport properties for Helium.

$$\kappa(T) = 0.0476 + 0.362 \cdot 10^{-3} T - 0.618 \cdot 10^{-7} T^2 + 0.718 \cdot 10^{-11} T^3. \tag{4.1}$$

With this, the Minitube2D in-house code has been used to simulate this experiment. The HLLC Riemann solver, the WENO5 scheme and the RK3TVD time integration method in a 1D domain of 400 cells have been selected for such simulation. The obtained density and the temperature profiles are compared to the experimental an numerical results from Muntz.

The density profile (Figure 4.6) shows a very good agreement with Muntz's results. It can be observed a correct diffusion of the shock wave caused by the axial gradient. Still, a sharp region can be appreciated in the middle of the channel. This means that the shock wave is not completely diffused yet, whereas Muntz's results predict a complete diffusion (the discontinuity is not appreciated). The reason behind can be found in the output time of the Minitube2D simulation. In Muntz's paper it is stated that experimental measures are carried during almost 30 s. However, this obviously does not mean that the provided profiles are captured at 30 s after the rupture of the diaphragm, since this would provide a completely diffused profiles because of the scales we are dealing with. Therefore, the output time has been estimated to be 4 μs, even though this is just an estimation because the information provided at the paper is not clear regarding this matter. Nonetheless, it is validated the correct diffusion of the shock wave for the 1D N-S simulation.

With regard to the temperature profile (Figure 4.7), results provided by the in-house code show a similar trend to Muntz's perpendicular experimental observation and numerical results (N-S Muntz). Again, differences may arise because of the simulation output time. It is worth to say that several output time have been tested, although very accurate profiles for both the density and the temperature fields could not be reproduced a the same time. For the numerical simulation, Muntz's computes the dynamic viscosity of the flow as $\mu \sim T^{0.647}$what may lead to discrepancies as well since in the Minitube2D code the Sutherland's law is used for such purpose. Altogether might yield to the minor differences that can be appreciated.

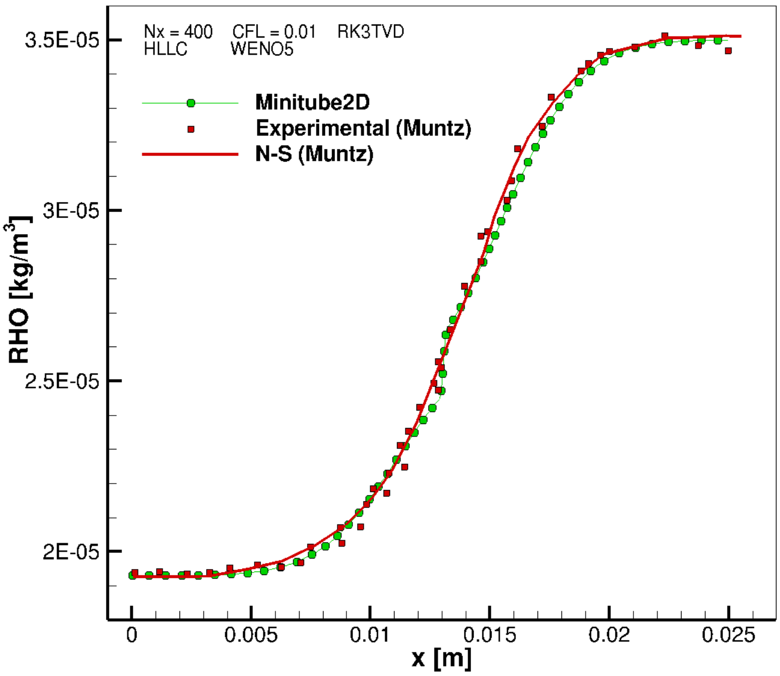

Figure 4.6: Density profile for Muntz's validation case.

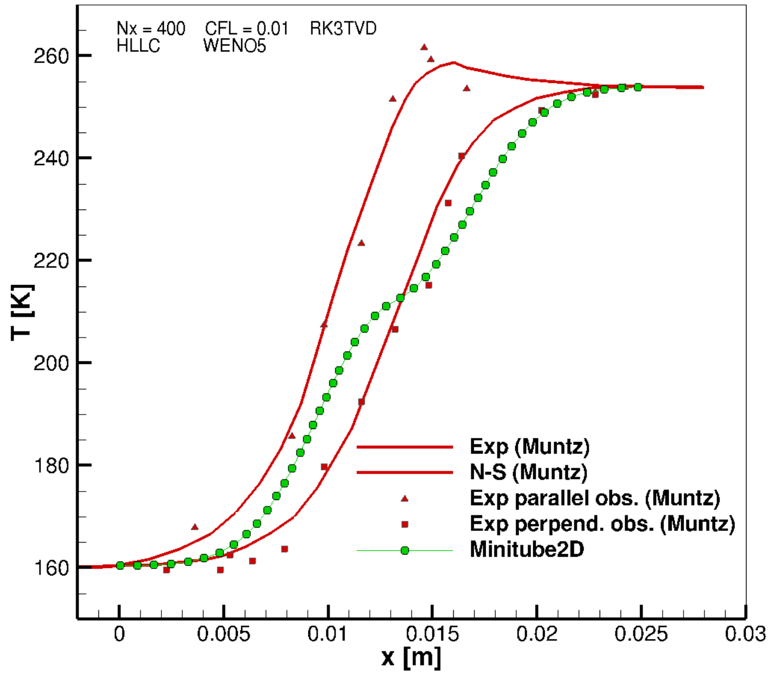

Figure 4.7: Temperature profile for Muntz's validation case.

4.3 Two-Dimensional Navier-Stokes Equations

4.3.1 Cartesian coordinate system

The Navier-Stokes equations in the 2D Cartesian coordinate system have been validated with numerical data provided by D. E. Zeitoun *et al.* in [3]. Zeitoun carried several numerical simulations using different approaches; the N-S equations, the DSMC for the Boltzmann equation, and the Bhatnagar-Gross-Krook equation (kinetic model) with the Shakhov equilibrium distribution function (altogether referred as BGKS). With this, the Minitube2D code can not only be validated with other N-S simulations, but with a kinetic model, being this a preferred option for simulations in the non-continuum regime. Also, Zeitoun uses a similar code to the Minitube2D. High-resolution shock-capturing TVD schemes (the order and the type are not specified) are used to compute the convective fluxes whereas the viscous fluxes are taken into account by a central FDM discretisation.

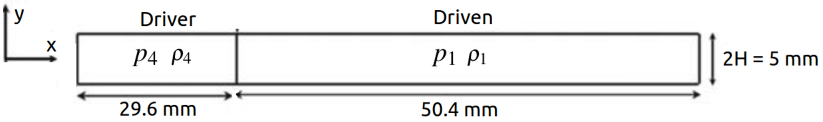

Figure 4.8: Schematic diagram of Zeitoun numerical test case.

Zeitoun provides results for $Kn_1 = 0.05$ (slip regime) and for $Kn_1 = 0.5$ (transitional regime) (note that Kn_1 refers to the Knudsen number computed in the region 1 of the shock tube accounting for half of the channel height (H) as the characteristic length). Important results from Zeitoun shown how the slip/no-slip BC affect the solution as the Knudsen number increases. Therefore, the correct implementation of the Maxwell's slip BC in the in-house code and its applicability limit (highest Kn) can be validated.

For $Kn_1 = 0.05$, the simulation set-up is described in the table below,

	Driver (4)	Driven (1)
Material	Argon	Argon
ρ [kg/m^3]	8.43E-03	7.08E-04
u [m/s]	0.0	0.0
v [m/s]	0.0	0.0
p [Pa]	525.98	44.20
Output time [μs]	80.0	
Dimensions [mm]	80.0×5.0	
Diaphragm position [mm]	29.6	
Walls BC	No-slip/Slip, Isothermal (300 K)	

Table 4.4: Zeitoun simulation set-up for $Kn_1 = 0.05$.

Simulations within the transitional regime, $Kn_1 = 0.5$, are set by modifying the initial pressure and density of both sections, thus maintaining the pressure ratio and the initial shock Mach number. Since $Kn \propto \frac{1}{\sqrt{p\rho}}$, setting $\rho_1 = 7.08E-05$ kg/m^3 and $p_1 = 4.42$ Pa provides the desired Knudsen number. Same procedure is applied to the driver section to keep the shock wave Mach number. The remaining parameters stay the same. The thermodynamic transport properties used for the argon gas are described below,

Specific gas constant, R [J/(kgK)]	208.0
Specific heats ratio, γ [-]	1.67
Specific heat at constant pressure, c_p [J/(kgK)]	532.0
Thermal conductivity, κ [W/(mK)]	0.0172
Sutherland's reference viscosity, μ_0 [kg/(ms)]	2.125E-05
Sutherland's reference temperature, T_0 [K]	273.15
Sutherland's temperature, S [K]	144.4

Table 4.5: Thermodynamic transport properties for Argon.

The HLLC Riemann solver together with the MPWENO11 scheme and the RK3TVD time integration method have been selected in the Minitube2D in-house code to perform this simulation in a 150x25 grid size. Results for the $Kn_1 = 0.05$ case are shown in Figure 4.9. Regarding the density profile, a very good agreement is shown with the results provided by Zeitoun. It can be appreciated that the CS and the SW are captured very accurately. This validates the propagation and the attenuation of these waves under the viscous effects for flows within the slip regime. Note that the BGKS results from Zeitoun are very close to the N-S ones, what points out that rarefaction effects are still not significant enough and therefore the continuum conservation equations can be applied yet.

As displayed in 4.9b, the temperature profile is also correctly suited with Zeitoun's one. The only difference is a tiny over-prediction of the region between the CS and the SW. In this same figure, the profile provided by the temperature transport equation is displayed as well (referred as SCALAR). Again, this profile shows a good match with the reference data, even though not as good as temperature field extracted from the energy equation and the state equation. Nevertheless, considering that this is an entire new and independent equation, the results are consistent enough thus validating the scalar transport equation modified to solve the transport of the temperature field independent from the original temperature field of the system.

The stream-wise velocity profile is again very accurately predicted. This is the expected results once knowing that the CS and SW are correctly propagated. Zeitoun's profile is obtained under the Maxwell's slip condition, so has been done for the Minitube2D code. However, the no-slip condition has been displayed as well in order to observe the differences between them. A reduction of the profile can be appreciated for the no-slip condition. This is because the slip condition helps the SW to propagate through the channel reducing the impact of the viscous dissipation effects. This allows the wave to travel longer distances for the same time and, because of this, this difference is appreciated.

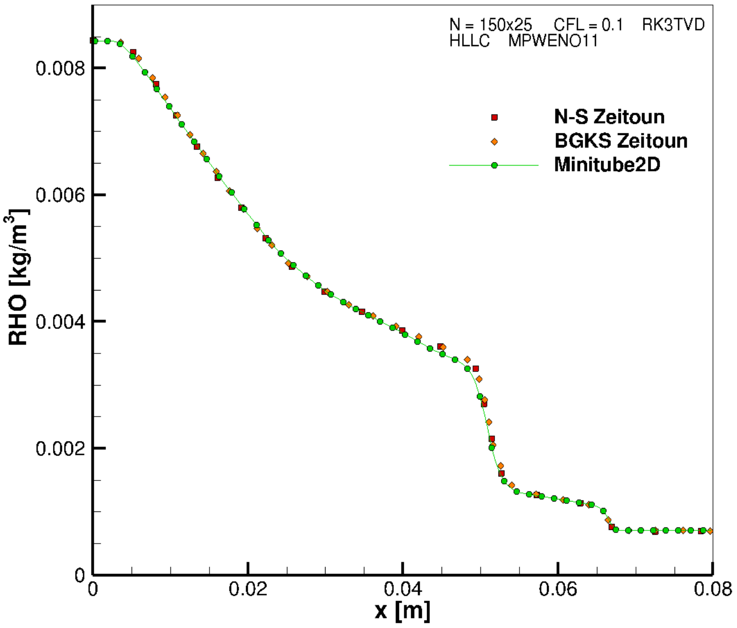

(a)

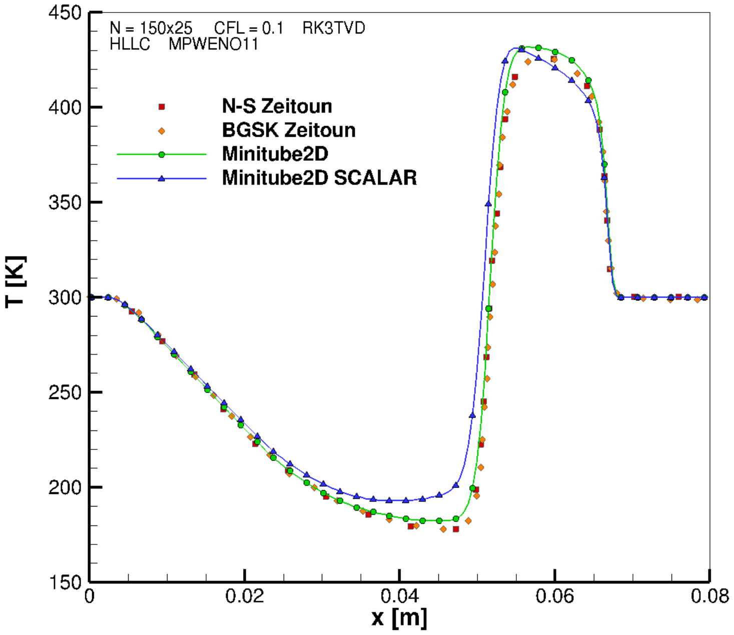

(b)

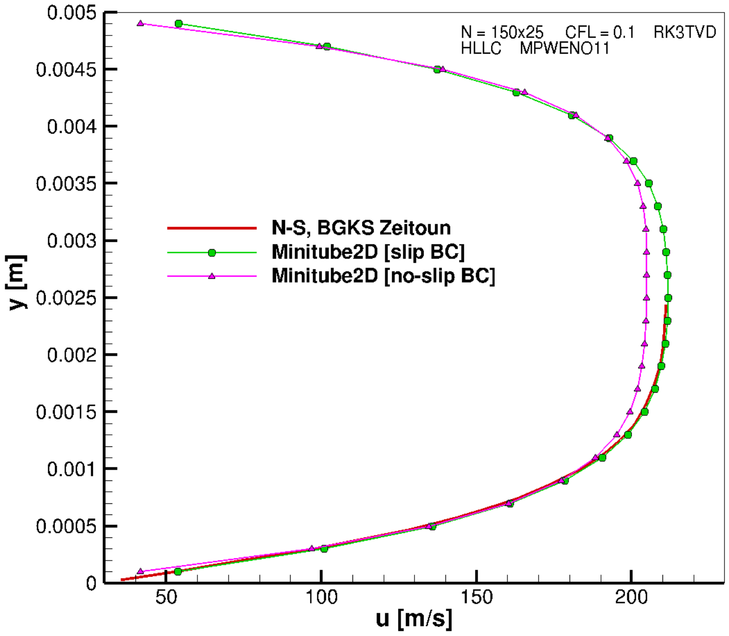

(c)

Figure 4.9: Zeitoun's case results for $Kn_1 = 0.05$. a) Density profile at the centreline. b) Temperature profile at the centreline. c) Stream-wise velocity profile across the channel height at $x = 25$H.

Results for the $Kn_1 = 0.5$ case are shown in Figure 4.10. It is worth to highlight that the CFL required to be reduced for this simulation from 0.1 to 0.004. Regarding the temperature profile, both the temperature field provided by the energy and the state equations, and the temperature field from the scalar transport equation are correctly suited with the N-S results provided by Zeitoun. Because of the strong rarefaction effects present ($Kn_1 = 0.5$, transitional flow), the distributions are now much more dissipated making it hard to be described as a shock propagation, as highlighted by Zeitoun. Even though, the kinetic model results that Zeitoun provides are not far from the ones obtained through the N-S approach. Hence, some flow features for transitional flows can still be predicted using a continuum approach.

With regard to the velocity profile, the distribution predicted by the Minitube2D code has a very similar shape as the one provided by Zeitoun. However, the velocity at the wall (slip velocity) is not suited yielding to a shift of the solution. Zeitoun mentions in his paper that the implementation of the slip BC has been performed in a dimensionless way whereas for the Minitube2D in-house code this is implemented in a dimensional equation. This shall be the main difference that brings to this discrepancy of the slip value. Note that now, at the transitional regime, the kinetic model results for the velocity profile are significantly different that the N-S ones (still this difference is not that big in the temperature profile, as it has been mentioned). The slip value provided by the BGKS kinetic model matches correctly the one predicted in the Minitube2D simulation. Therefore, it is possible that the slip value computed in the Zeitoun N-S approach (given by a dimensionless formulation) is not correct enough since the dimensional computation of the slip value in the Minitube2D code is in good agreement with Zeitoun's kinetic model. This difference arising from the formulation of the slip BC could not be appreciated for the slip regime since the rarefaction effects were not remarkable enough. As a side note, notice that the distribution under the no-slip condition is now totally incorrect thus empathising the need of the slip condition for strongly rarefied flows.

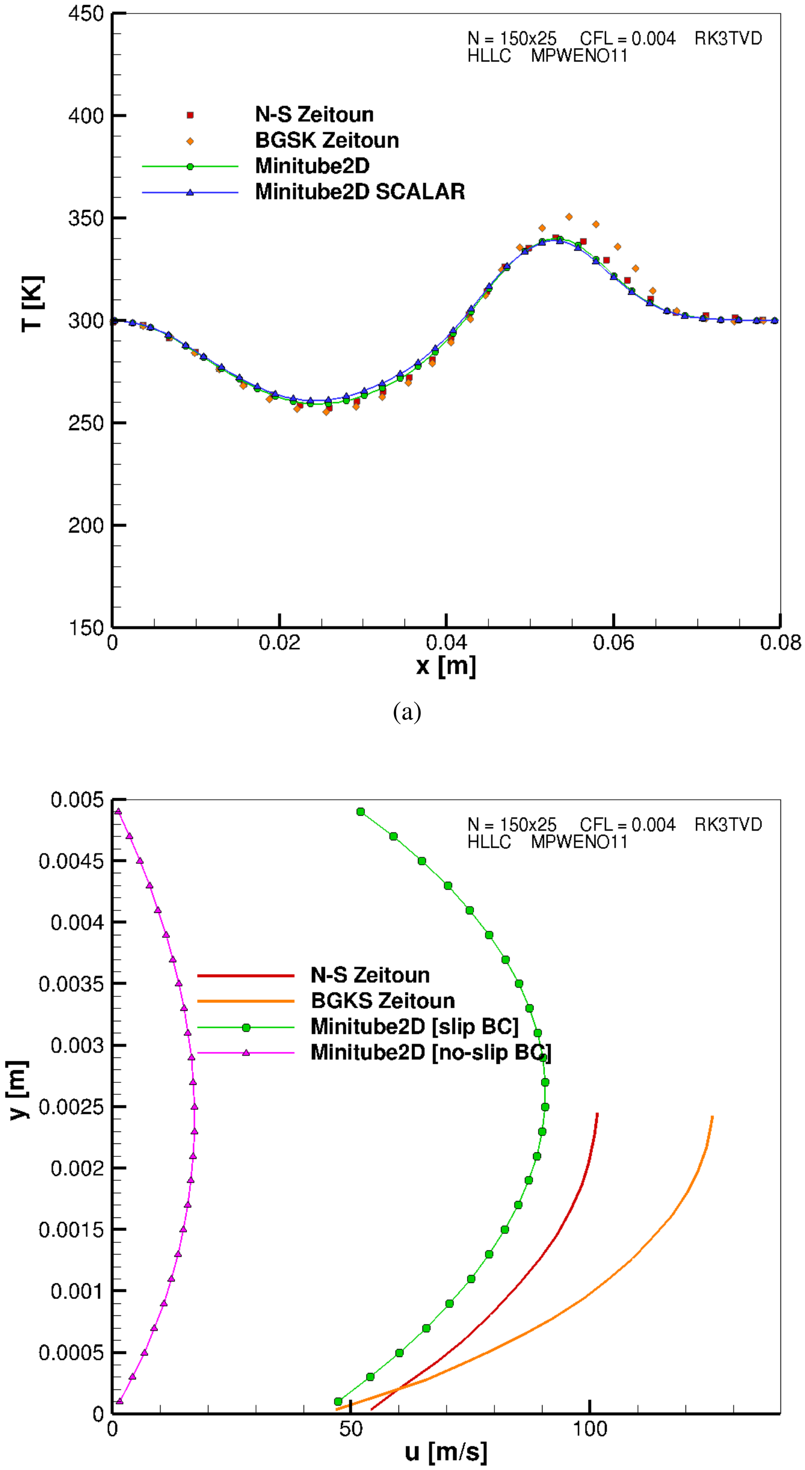

(a)

(b)

Figure 4.10: Zeitoun's case results for $Kn_1 = 0.5$. a) Temperature profile at the centreline. b) Stream-wise velocity profile across the channel height at $x = 22.5$H.

Finally, the temperature and the stream-wise velocity flowfields are displayed for the slip and the transitional flows. Figure 4.11 shows results for $Kn_1 = 0.05$. In the temperature flowfield, a thick boundary layer is appreciated behind the shock wave, especially in the region close to the contact surface. Thus, the maximum temperature values are located in the centreline of the channel indicating that dissipation effects are important indeed. The same trend can be observed in the velocity contour.

With respect to the $Kn_1 = 0.5$ results displayed in Figure 4.12, a much more diffused solution is shown for both the temperature and the velocity profiles, as pointed out before. Remember that to achieve $Kn_1 = 0.5$, the initial pressures and density have been modified, not the ratio between them (so the shock wave Mack number has remained constant). The diffused distributions that can be appreciate take place because of a Reynolds number drop caused by the initial pressures reduction, yielding to higher viscous effects. Other important features that can be observed and that will be discussed in Section 4.4 is that the shock wave propagation distance is reduced and that the shock wave strength is more attenuated for the transitional flow.

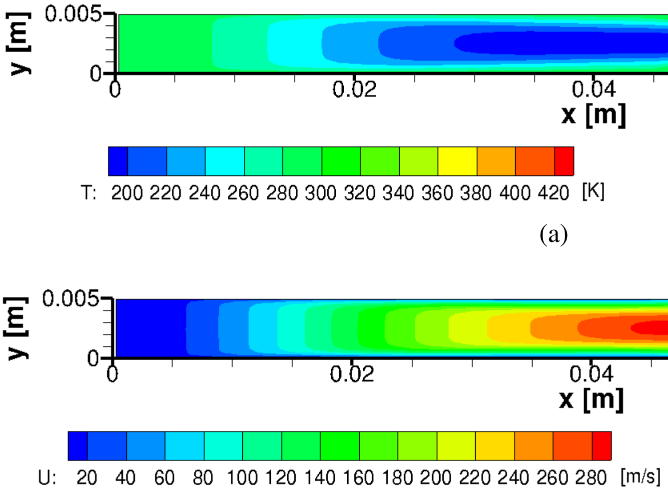

(a)

(b)

Figure 4.11: Zeitoun's case 2D results for $Kn_1 = 0.05$. a) Temperature flowfield b) Stream-wise velocity flowfield.

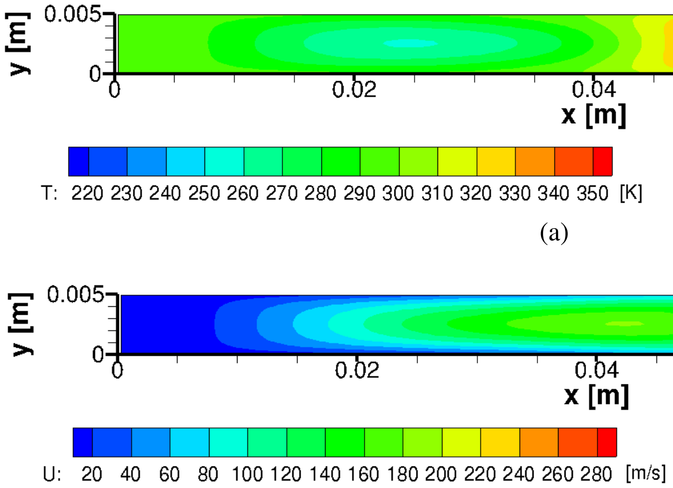

(a)

(b)

Figure 4.12: Zeitoun's case 2D results for $Kn_1 = 0.5$. a) Temperature flowfield b) Stream-wise velocity flowfield.

4.3.2 Axisymmetric coordinate system

A. R. Kumar *et al.* [4] provided numerical results for a 2D axisymmetric shock tube model. In this study several scale effects are studied such as the shock attenuation in function of the initial pressures ratios and the Knudsen number. We are interested in the temperature profile at the symmetry axis displayed in the grid convergence study part of the paper, which will be used as reference data to validate the implementation of the 2D axisymmetric coordinate system in the Minitube2D in-house code. The simulation carried by Kumar is detailed below,

	Driver (4)	Driven (1)
Material	Air	Air
ρ [kg/m^3]	1.16E-01	1.16E-03
u [m/s]	0.0	0.0
v [m/s]	0.0	0.0
p [Pa]	100	10000
Output time [μs]	10.0	
Dimensions [mm]	130.0×3.0	
Diaphragm position [mm]	50.0	
Walls BC	No-slip, Isothermal (300 K)	

Table 4.6: Kumar's simulation set up.

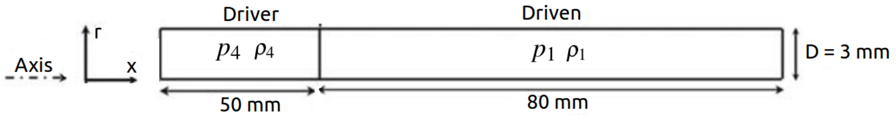

Figure 4.13: Schematic diagram of Kumar's numerical test case.

In Kumar's simulation, ANSYS Fluent commercial solver is used to solve the governing equations set. Turbulence is modelled through the $k-\omega$ SST RANS-based method. The spatial discretisation is performed with a 3$^{\text{rd}}$-order monotonic upwind scheme and the time integration is carried with a 2$^{\text{nd}}$-order implicit scheme. The Minitube2D in-house code does not have a turbulence model, even though not significant differences should be observed since this simulation is performed at a low Reynolds number. The thermodynamic transport properties of the air considered in the in-house code are detailed in Table 4.7.

Specific gas constant, R [J/(kgK)]	287.0
Specific heats ratio, γ [-]	1.4
Specific heat at constant pressure, c_p [J/(kgK)]	see eq. 3.71
Thermal conductivity, κ [W/(mK)]	see eq. 3.72
Sutherland's reference viscosity, μ_0 [kg/(ms)]	1.716E-05
Sutherland's reference temperature, T_0 [K]	273.15
Sutherland's temperature, S [K]	110.4

Table 4.7: Thermodynamic transport properties for dry Air.

Two different schemes have been used in the Minitube2D in-house code for this test case: the MUSCL2 minmod and the MPWENO11. With this, different types of reconstruction schemes can be tested for the axysimmetric coordinate system. These schemes are used together with the HLL Riemann solver and the RK3TVD time integration method. It should be pointed out that, at first instance, the HLLC Riemann solver was used. However, the simulation was not stable enough blowing up at a certain point. In the other hand, the HLL solver performed correctly. So, the HLLC solver is very sensitive to the initial conditions and depending on the test case can yield to unstable simulations. Regarding the boundary conditions of the axisymmetric coordinate system, the only different with respect to the Cartesian one is that the axis of the tube (set in the lower boundary) is treated as a transmissive BC, as explained in Section 3.2.5. With this, 3 different grids are used to check the convergence of the solution as the grid is refined.

Coarse (C)	600×20
Medium (M)	1000×50
Fine (F)	1600×80

Table 4.8: Different axisymmetric grids used for the Kumar test case.

The results for the MUSCL2 minmod and the MPWENO11 schemes are presented in Figure 4.14a and 4.14b respectively. For both schemes, it can be noted that as the grid is refined the temperature profile gets more centred to the one provided by Kumar. Also, the slopes of the SW and the CS are sharper for the most refined grid. In Figure 4.15 both schemes can be observed for the finest grid. The main difference can be noted in the slope of the CS, where the MPWENO11 provides a less diffused profile than the MUSCL2 scheme. Furthermore, the region between the SW and the CS is again better predicted by the MPWENO11, matching in a more correct way the shape provided by Kumar. Nevertheless, both schemes present an over-predicted profile (offset) with respect to Kumar's results, even though the shape of the profile is in very good agreement. This offset probably takes place because of the turbulence model used by Kumar. Since a

RANS turbulence models is employed, turbulence is accounted by means of an extra term in the N-S equations that introduces additional numerical diffusion to the system yielding to more attenuated profiles. In regard to the spatial discretisation scheme used by Kumar, significant differences should not be observed because of the scheme (even though it is just 3rd-order accurate) since the discrepancy between the MUSCL2 and the MPWENO11 scheme performed with the Minitube2D in-house code is not critical.

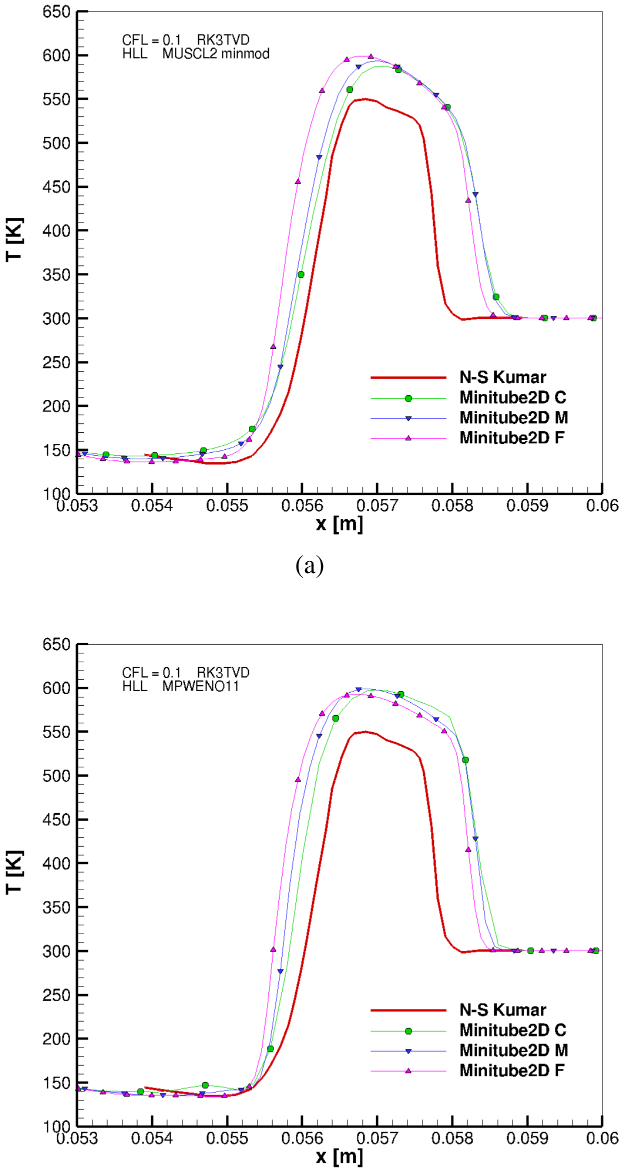

(a)

(b)

Figure 4.14: Temperature profile at the symmetry axis for different grid sizes. a) MUSCL2 minmod. b) MPWENO11.

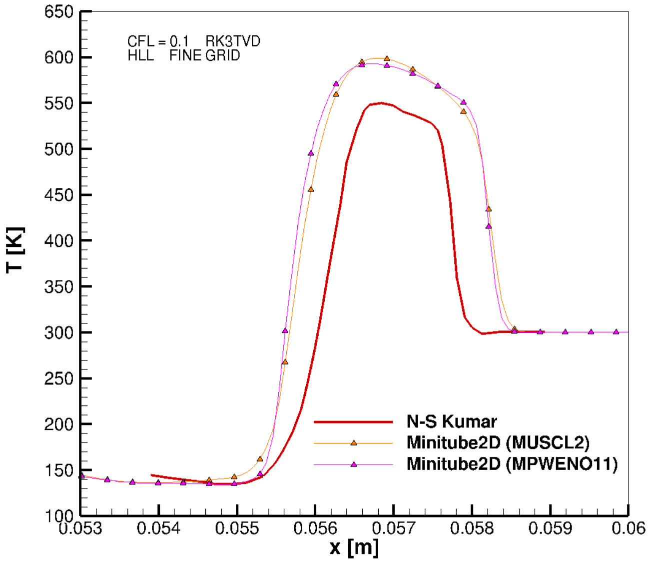

Figure 4.15: Temperature profile at the symmetry axis comparison between MUSCL2 minmod and MPWENO11 schemes for the fine grid.

4.4 Scale Effects Study

Scale effects (or rarefaction effects) related to micro-shock tubes are studied in this section. The Zeitoun test case is used as baseline for different computations. The shock wave propagation along the channel is investigated under different conditions. The influence of the Knudsen number and the initial pressures ratio is discussed and explained from a physical point of view. The Knudsen number can be modified either by varying the initial pressures or the channel diameter.

4.4.1 Influence of the Knudsen number

Different Kn_1values have been investigated for both the slip and the no-slip BCs by varying the initial pressures of the shock tube as performed in Section 4.3.1. Figures 4.16 and 4.17 show the normalised shock wave propagation distance, where x_s is the shock position, x_0 is the location of the diaphragm and ζ is the pseudo-time. The shock position is considered at the point where $\rho = 1.05\rho_1$ (which is the same criteria as applied by Zeitoun in [3]). The pseudo-time is computed as

$$\zeta = H/a_1, \quad a_1 = \sqrt{\gamma R T_1}. \tag{4.2}$$

The black dashed line displayed on the figures represents the theoretical propagation of the shock wave for a given Mach number M_{th}, so without the presence of viscous terms (ideal theory). The general trend observed in both figures is that as the Knudsen number increases, the shock propagation distance is reduced. This phenomenon is more emphasised for the no-slip condition case. When the initial pressures are reduced, the flow is pushed under stronger rarefaction conditions (Kn increase). As the initial pressures decrease, the Reynolds number decreases as well. This makes the dissipation effects more important because of a thicker boundary layers developing behind the shock wave, thus reducing the shock wave propagation. The slip condition helps to mitigate this effect, although the tendency still remains. For the no-slip condition, increasing Kn results into a drastic fall of the shock propagation distance.

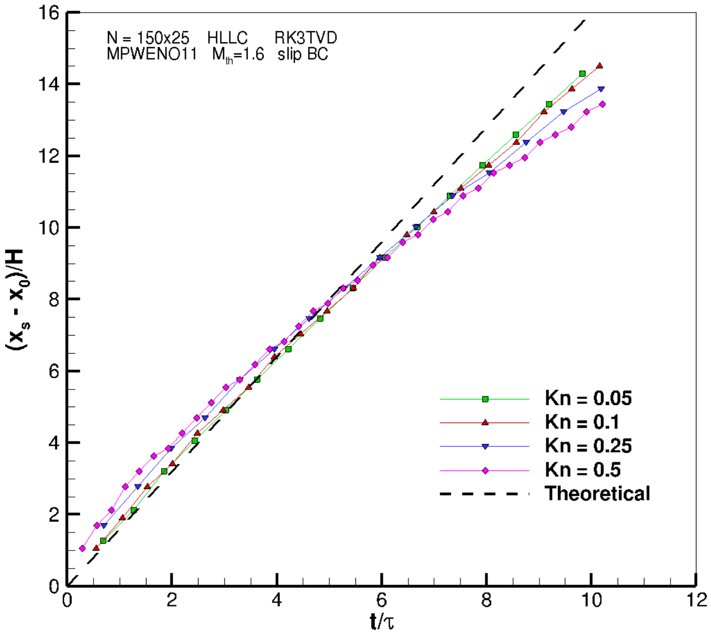

Figure 4.16: Shock wave propagation distance for different Knudsen numbers under the slip BC.

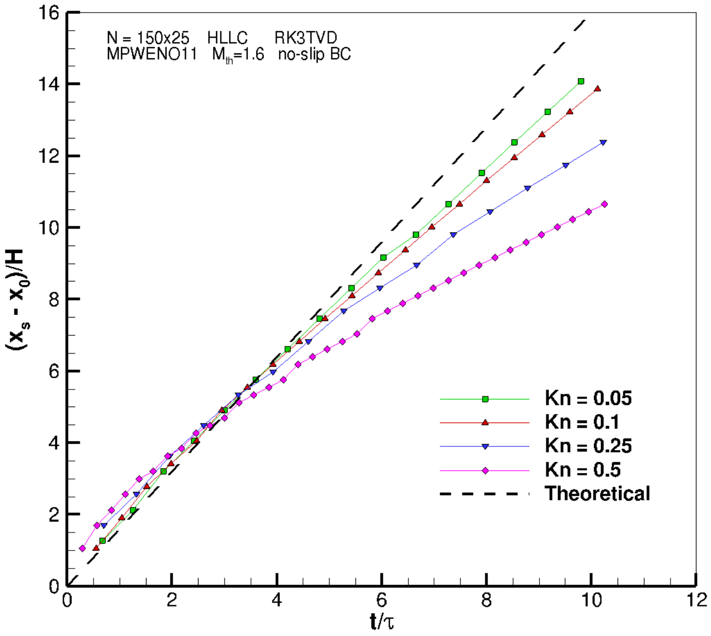

Figure 4.17: Shock wave propagation distance for different Knudsen numbers under the no-slip BC.

The evolution of the shock strength is more complicated to post-process since for rarefied flows shock waves get very dissipated, as it has been already pointed out. However, through the density distribution at the centreline for different output times, the shock wave strength can be analysed. In Figure 4.18a and Figure 4.18b the density profiles for $Kn_1 = 0.05$ and $Kn_1 = 0.1$ can be respectively observed.

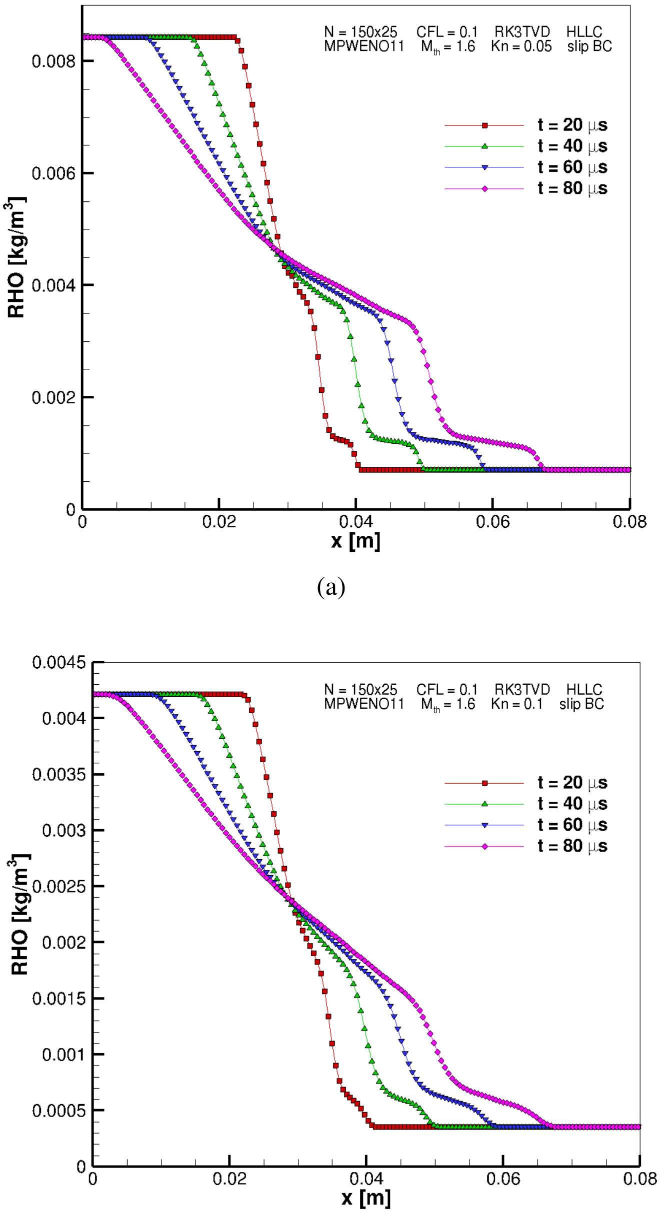

(a)

(b)

Figure 4.18: Density distribution at the centreline at different output times under the slip BC. a) $Kn_1 = 0.05$ b) $Kn_1 = 0.1$.

In figures 4.18a and 4.18b it is appreciated how the shock strength gets more attenuated as the shock wave propagates and this effect increases with rarefaction. So, for the $Kn_1 = 0.1$ case, the shock strength decays faster than for $Kn_1 = 0.05$. This attenuation can be noticed by observing the density jump evolution for both cases at different output times. In fact, the shock wave strength M_s for a normal shock wave can be obtained from the following relation

$$\frac{\rho_4}{\rho_3} = \frac{(\gamma+1)M_s^2}{(\gamma-1)M_s^2+2}. \tag{4.3}$$

For $Kn_1 = 0.05$, the shock wave strength decay could be computed using the previous relation since the shock is not as diffused as for more rarefied flows. In Figure 4.19 this attenuation is clearly appreciated showing an exponential decay of the shock strength.

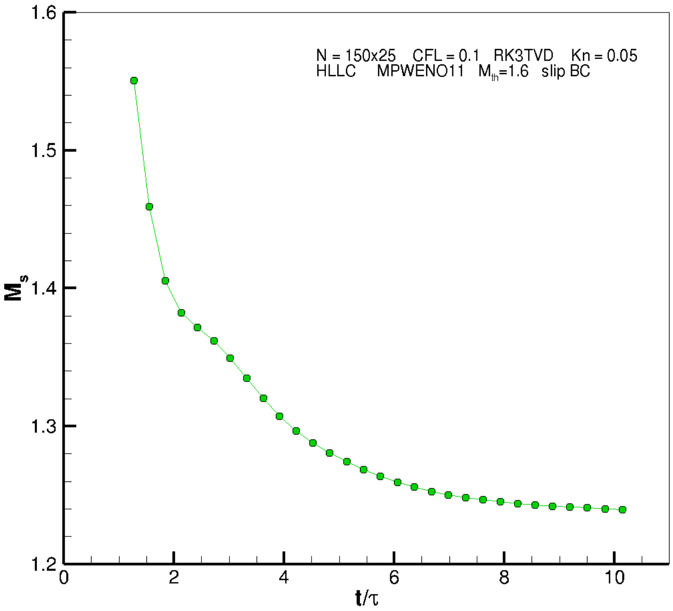

Figure 4.19: Shock wave attenuation for $Kn_1 = 0.05$ under the slip BC.

Next, the Knudsen number is modified by varying the channel height. In Figure 4.20 it is shown the shock propagation distance for 5 mm, 2.5 mm and 1 mm channel heights, what is equivalent to a Knudsen number of 0.05, 0.1 and 0.25 respectively. As the channel height is reduced, the shock wave propagation distance decays emphasising this trend for shorter channel heights. Reducing the height of the channel turns into an smaller Reynolds number. Again, this triggers severe viscous dissipation effects that weakens the shock wave propagation. So, increasing the Knudsen number by either reducing the initial pressures or reducing the channel height results into an stronger attenuation of the shock wave propagation. Therefore, the Knudsen number can be treated as a single parameter that takes into account the initial pressure conditions and the geometrical characteristics, as pointed out by A. R. Kumar in [4].

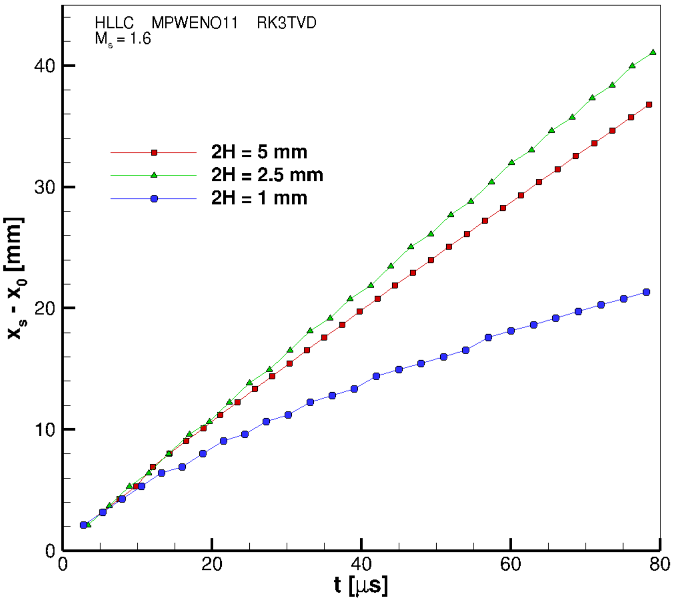

Figure 4.20: Shock wave propagation distance for different channel heights.

4.4.2 Influence of the Pressure Ratio

The influence of the pressure ratio (p_{41}) between the driver and the driven section of the shock tube is discussed. As given by eq. 2.1, a certain pressure ratio provides a theoretical Mach number at which the shock wave propagates. Figure 4.21 shows the shock wave propagation distance for $M_{th} = 1.6$ and $M_{th} = 1.8$, or what is equivalent, $p_{41} = 11.9$ and $p_{41} = 24.6$ respectively. The slip and no-slip BCs are also considered. It can be observed that, obviously, the shock wave propagation velocity is higher as the pressure ratio increases because of an increment of the shock wave strength. Again, under the slip condition the shock wave propagates faster. The shock wave propagation decays faster for lower pressure ratios. As it is mentioned in other works as Zeitoun's [3] and Kumar's [55, 4], for sufficiently low pressure ratio the shock wave eventually becomes a compression wave ($M_s < 1$).

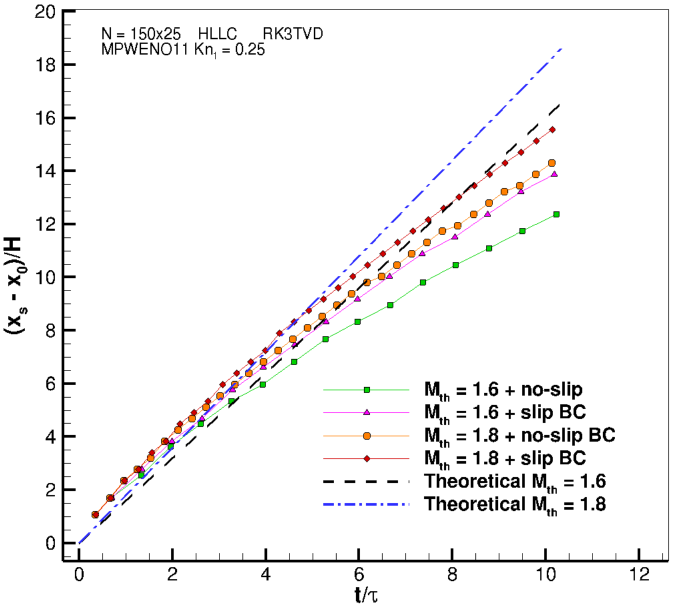

Figure 4.21: Shock wave propagation distance at different pressure ratios for $Kn_1 = 0.25$.

Chapter 5

Summary and Conclusions

The shock wave propagation in small-scale shock tubes has been investigated. At these length scales, non-continuum effects and wall effects dominate the flow physics associated to the shock wave propagation phenomena. The Minitube2D FORTRAN in-house code has been further developed to solve the fully compressible Navier-Stokes (N-S) equations in different coordinate systems. The advective fluxes are computed using (very) high-order shock wave-capturing schemes together with approximate Riemann solvers under the Godunov-type methods umbrella with a cell- centred FVM approach. The viscous fluxes are computed using a forwards-backwards FDM discretisation. Different high-order Runge-Kutta (RK) time integration methods are considered as well. The Maxwell's slip and the temperature jump boundary conditions have been implemented to account for the rarefaction effects present in small-scale problems.

5.1 Conclusions of the Thesis

The Sod shock tube test case has been considered in order to assess the implementation of the numerical schemes that solve the advective fluxes (the Euler equations). On one hand, the Rusanov Riemann solver has proved to be the most dissipative one and, on the other hand, the HLLC solver has presented the best performance on capturing the CS, as expected. It has been shown that TVD schemes are required to obtain very accurate solutions free of spurious oscillations. However, the MPWENO schemes become a bit oscillatory at very high orders (9^{th} and 11^{th}) as observed by other authors [73, p. 110]. The fact that the reconstruction procedure is performed using the conservative variables instead of the primitives variables might have an impact in this sense as well, as pointed out in [66]. To reduce this effect, different high order TVD RK methods have been validated together with MPWENO schemes obtaining smoother and more accurate profiles.

The 1D Navier-Stokes equations have been validated using the experimental and numerical results provided by E. P. Muntz *et al.* [2]. Even though some information regarding the experiment and the numerical computations of Muntz was lacking, the Minitube2D in-house code using the HLLC solver, the WENO5 reconstruction scheme and the RK3TVD time integration method showed a general good agreement with Muntz's results. Some of the discrepancies might arise from the output time of the solution and the calculation of the dynamic viscosity, which is different in Muntz's model. Nevertheless, a correct dissipation of the shock wave could be observed. This provides important information before extending the viscous computation into a 2D domain.

The 2D Navier-Stokes equations in the Cartesian coordinate system have been validated with D. E. Zeitoun *et al.* [3] numerical results. Zeitoun's results are provided for the N-S approach as well as for two different kinetic models. Therefore, the applicability limit of the Minitube2D in-code in terms of flow regime (that solves the N-S equations) is tested showing a good agreement up to $Kn = 0.5$ (transitional regime). The simulation is carried using the HLLC solver, the MPWENO11 scheme and the RK3TVD time integration method. For the slip regime case ($Kn = 0.05$), the density and the temperature distributions along the centreline of the channel match very closely to Zeitoun's results. Also, the velocity profile across the channel height is in very good agreement. The temperature field obtained by the temperature transport equation is shown and compared to the temperature field obtained through the energy equation and the equation of state. Both curves are accurately suited, thus validating the implementation of an independent scalar transport equation. The effect of using the no-slip condition instead of the slip one is also displayed. It can be seen that the no-slip condition provides incorrect profiles being this effect more important for the transitional regime. Therefore, the Maxwell's slip condition is required as rarefaction effects increase.

The 2D Navier-Stokes equations in the axisymmetric coordinate system have been validated with the numerical data from A. R. Kumar *et al.* [4]. The Minitube2D code has been set with the HLL solver, the MPWENO11 and MUSCL2 schemes, and the RK3TVD time integration method. Three different grids are accounted for this simulation. It is worth to point out that the HLL solver was used instead of the HLLC solver since the latter is very sensitive to the initial conditions and, because of this, it was not stable enough to perform this simulation. The temperature profile in the symmetry axis is compared to the one obtained by Kumar and it can be seen that, for both schemes, the distribution provided by the in-house code shows a good agreement with the reference data as the grid is refined. However, the profile is over-predicted yielding to a notably offset. The reason behind these results might reside in the fact that Kumar is using an extra term in the N-S equations to account for the turbulence. In Kumar's simulation, turbulence is considered through the $k-\omega$ SST RANS model. This introduces additional numerical diffusion that could yield to more attenuated profiles.

Finally, the scale effects have been investigated using Zeitoun's simulation as a baseline case. The influence of the Knudsen number is analysed by varying the initial pressures of the shock tube (maintaining the pressure ratio) and the channel height. Lower pressures yield to a lower Reynolds number, what makes the viscous dissipation effects more important. Thus, a thicker boundary layer develops behind the shock wave and the shock propagation distance severely decays. Under the slip condition, the shock wave propagation distance is larger if compered to the no-slip one. The slip condition reduces the viscous effects at the wall helping the flow to keep the momentum. The shock wave propagation decay effect is emphasised as the flow is more rarefied. An attenuation of the shock wave strength can also be observed for lower initial pressures. All the previous effects are also visible when the channel height is reduced. Both actions (reducing the initial pressures or reducing the channel height) are actually increasing the Knudsen number, hence making the rarefaction effects more important. So, the Knudsen number can be considered a general case parameter accounting for both the initial pressure conditions and the geometrical characteristics. The influence of the initial pressure ratio is also considered. High pressure ratios generate faster shock waves. Hence, the shock propagation attenuation (eventually becoming a compression wave) is more important for low pressure ratios.

5.2 Future Work

The extension of the Minitube2D in-house code to the 3D Cartesian and cylindrical coordinate system might be a valuable work in order to compare the scale effects between different shapes since, at the moment, the 2D channel is the only option available.

Regarding the numerical schemes, higher order MUSCL schemes could be tested as well as more accurate slope limiters to check if the same oscillatory trend that appears in the MPWENO schemes takes place for the MUSCL schemes too.

The axisymmetric coordinate system could be further validated with other test cases to ensure that the over-predicted profile is not an issue of the developed code.

The implementation and validation of high-order Maxwell's slip and temperature jump boundary conditions could also be a good investigation line. Actually, this has not been performed in the present work since no numerical data of high-order boundary conditions was found. However, the effect of high-order BCs could be tested and compared with experimental results of strongly rarefied flows. Including these type of boundary conditions could extend the applicability of the Minitube2D code to higher Knudsen numbers flows.

Several micro shock tubes including different gases for the driver and the driven sections have been found in the literature. Therefore, adapting the Minitube2D for such purpose would further generalise the in-house code being able to simulate a wider range of micro shock tube applications.

A change of the code data structure would be worth to study as well. Storing the primitive variables instead of the conservative variables would allow an easier application of the boundary conditions as well as a more robust reconstruction procedure.

The finest future work must be to resolve (or model) turbulence at small length scales with the presence of shock waves. Since the core of the Minitube2D code is a Godunov-type shock-capturing method, an Implicit Large Eddy Simulation (ILES) technique could be incorporated to the in-house code. Thus, the sub-grid scales (SGS) of turbulence would be implicitly modelled by the Godunov method and micro shock tubes could be simulated for high Reynolds number flows, where a turbulent boundary layer develops behind the propagated shock wave.

Finally, regarding the flow physics, it would be interesting to investigate the flow duration time at different rarefaction levels and to compute the shock wave strength for transitional flows. This means to introduce a wider post-processing build in the code that would definitely allow the user to explore multiple flow physics required for the design of micro-applications.

Bibliography

[1] G. M. Whitesides. The Origins and the Future of Microfluidics. *Nature*, 442:368–373, 2006.

[2] E. P. Muntz and L. N. Harnett. Molecular Velocity Distribution Function Measurements in a Normal Shock Wave. *Physics of FLuids*, 12(10):2027–2035, 1969.

[3] D. E. Zeitoun, Y. Burtshell, and I. A. Graur. Numerical Simulation of Shock Wave Propagation in Micro Channels using Continuum and Kinetic Approaches. *Shock Waves*, 19:307–316, 2009.

[4] A. R. Kumar, H. D. Kim, and T. Setoguchi. Computational Analysis of the Wave Motions in Micro-Shock Tube Flow. *Journal of Aerospace Engineering*, 228(4):594–610, 2013.

[5] G. Karniadakis, A. Beskok, and N. Aluru. Microflows and Nanoflows. *Springer-Verlag, New York*, 2005.

[6] E. F. Toro. Riemann Solvers and Numerical Methods for Fluid Dynamics. *Springer-Verlag, New York*, 1997.

[7] G. Mirsheraki and M. Brouillette. One-Dimensional Model for Microscale Shock Tube Flow. *Shock Waves*, 19(1):25–38, 2009.

[8] D. Drikakis and W. Rider. High Resolution Methods for Incrompressible and Low-Speed Flows (Computational Fluid and Solid Mechanics). *Springer-Verlag, Berlin*, 2004.

[9] X. Zheng. A General Approach to Enhance Slope Limiters on Non-Uniform Rectilinear Grids. *Lecture Notes from the Cornell University, Numerical Analysis*, 2014.

[10] M. Gad el Hak. Use of Continuum and Molecular Approaches in Microfluidics. *AIAA, 3rd Theoretical Fluid Mechanics Meeting*, 2868, 2002.

[11] N.-T. Nguyen and S. T. Wereley. Fundamentals and Applications of Microfluidics (2nd edition). *Artech House, London*, 2006.

[12] S. G. Kandlikar, S. Garimella, D. Li, S. Colin, and M. R. King. Heat Transfer and Fluid Flown in Minichannels and Microchannels. *Elsevier Science, Amsterdam*, 2005.

[13] E. B. Arkilic, M. A. Schmidt, and K. S. Breuer. Gaseous Slip Flow in Long Microchannels. *Journal of Microelectromechanical systems*, 6(12), 1997.

[14] W.-M. Zhang, G. Meng, and X. Wei. A Review on Slip Models for Gas Microflows. *Microfluid Nanofluid, Springer-Verlag*, 2012.

[15] S. Janardhanraj and G. Jagadeesh. Studies on Shock Wave Attenuation in Small Tubes. *28th International Symposium on Shock Waves. AIP Conference Proceedings*, pages 569–574, 2012.

[16] J. Giordano, J. D. Parisse, L. Biamino, J. Devesvre, and P. Perrier. Experimental and Numerical Study of Weak Shock Wave Transmissions through Minitubes. *Physics of Fluids*, 22(061703), 2010.

[17] R. Courant and K. O. Friedrichs. Supersonic Flow and Shock Waves. *Interscience Publishers, New York*, 1948.

[18] P. O. K. Krehl. History of Shock Waves, Explosions and Impact: A Chronological and Biographical Reference. *Springer-Verlag, Berlin*, 2004.

[19] J. Naber. Building Your Own Shock Tube. *Modelling, Analysis and Simulation [MAS]*, (MAS-E 0502):1–88, 2005.

[20] G. A. Sod. A Survey of Several Finite Difference Methods for Systems of Nonlinear Hyperbolic Conservation Laws. *Journal of Computational Physics*, 27:1–31, 1978.

[21] S. K. Godunov. A Finite-Difference Method for the Numerical Computation and Discontinuous Solutions of the Equations of Fluid Dynamics. *Matematicheskii Sbornik*, 47:271–306, 1959.

[22] V. A. Titarev and E. F. Toro. Weno Scheme based on Upwind and Centred TVD Fluxes. *Computers & Fluids*, 34:705–720, 2005.

[23] B. van Leer. Towards the Ultimate Conservative Difference Sheme I. The Quest of Monotonicity. *Lecture Notes in Physics, University Observatory, Leiden*, 18:163–168, 1973.

[24] B. van Leer. Towards the Ultimate Conservative Difference Sheme II. Monotonicity and Conservation Combined in a Second Order Scheme. *Journal of Computational Physics*, 14:361–370, 1974.

[25] B. van Leer. Towards the Ultimate Conservative Difference Sheme III. Upstream-Centered Finite Difference Schemes for Ideal Compressible Flows. *Journal of Computational Physics*, 23:263–275, 1977.

[26] B. van Leer. Towards the Ultimate Conservative Difference Sheme IV. A New Approach to Numerical Convection. *Journal of Computational Physics*, 14:159–179, 1977.

[27] B. van Leer. Towards the Ultimate Conservative Difference Sheme V. A Second-Order Sequel to Godunov's Method. *Journal of Computational Physics*, 32:101–136, 1977.

[28] P. Colella. A Direct Eulerian MUSCL Scheme for Gas Dynamics. *SIAM Journal on Scientific and Statistical Computing*, 6:104–117, 1985.

[29] P. Colella and P. R. Woodward. The Piecewise-Parabolic Method (PPM) for Gas-Dynamical Simulations. *Journal of Computational Physics*, 54:174–201, 1984.

[30] J. P. Boris. A Fluid-Transport Algorithm that Works. *Computing as a Language of Physics*, pages 171–189, 1971.

[31] J. P. Boris and D. L. Book. Flux-Corrected Transport I: SHASTA, A Fluid-Transport Algorithm that Works. *Journal of Computational Physics*, 11:38–69, 1973.

[32] J. P. Boris and D. L. Book. Flux-Corrected Transport II: Generalization of the Method. *Journal of Computational Physics*, 18:248–283, 1975.

[33] J. P. Boris and D. L. Book. Flux-Corrected Transport III: Minimal Error FCT Method. *Journal of Computational Physics*, 20:397–431, 1976.

[34] A. Harten. High Resolution Schemes for Hyperbolic Conservations Laws. *Journal of Computational Physics*, 49:357–393, 1983.

[35] J. B. Goodman and R. J. LeVeque. On the Accuracy of Stable Schemes for 2D Conservation Laws. *Mathematics of Computation*, 45:15–21, 1985.

[36] V. Daru and C. Tenaud. Numerical Simulation of the Viscous Shock Tube Problem by using a High Resolution Monotonicity-Preserving Scheme. *Computers & Fluids*, 38:664–676, 2009.

[37] B. van Leer. Upwind and High-Resolution Methods for Compressible Flow: From Donor Cell to Residual-Distribution Schemes. *16th AIAA Computational Fluid Dynamics Conference*, 2003.

[38] P. Batten, N. Clarke, C. Lambert, and D. M. Causon. On the Choice of Wavespeed for the HLLC Riemann Solver. *SIAM Journal on Scientific Computing*, 18(6):1553–1570, 1997.

[39] A. Harten, P. D. Lax, and B. Van Leer. On Upstream Differencing and Godunov-type Schemes for Hyperbolic Conservation Laws. *SIAM Journal on Scientific Computing*, 25:35–61, 1983.

[40] E. F. Toro, M. Spruce, and W. Speares. Restoration of the Contact Surface in the HLL Riemann Solver. *Shock Waves*, 4:25–34, 1994.

[41] H. Mirels. Test Time in Low-Pressure Shock Tubes. *Physics of Fluids*, 6(9):1201–1214, 1963.

[42] W. Garen, B. Meyerer, S. Udagawa, and K. Maeno. Shock Waves in Mini-Tubes: Influence of the Scaling Parameter S. *Proceedings of 26th International Symposium on Shock Waves*, pages 1473–1478, 2009.

[43] R. E. Duff. Shock-Tube Performance at Low Initial Pressure. *Physics of Fluids*, 2(2):207–216, 1959.

[44] A. Roshko. On Flow Duration in Low-Pressure Shock Tubes. *Physics of Fluids*, 3(6):835–842, 1960.

[45] M. Brouillette. Shock Waves at Microscales. *Shock Waves*, 13(1):3–12, 2003.

[46] D. E. Zeitoun and Y. Burtshell. Navier-Stokes Computations in Micro Shock Tubes. *Shock Waves*, 15:241–246, 2006.

[47] Y. Burtshell, D. E. Zeitoun, and Y. Cardoso. Numerical Analysis of Reducing Driver Gas Contamination in Impulse Shock Tunnels. *AIAA Journal*, 39(12):2357–2365, 2001.

[48] G. N. Markelov, A. N. Kudryavstev, and M. S. Ivanov. Continuum and Kinetic Simulation of Laminar Separated Flow at Hypersonic Speeds. *Journal of Spacecraft and Rockets*, 37:499–506, 2000.

[49] J. Giordano, J. D. Parisse, and P. Perrier. Numerical Study of an Original Device to Generate Compressible Flow in Microchannels. *Physics of Fluids*, 20(096101), 2008.

[50] D. Ngomo, A. Chaudhuri, A. Chinnayya, and A. Hadjadj. Numerical Study of Shock Propagation and Attenuation in Narrow Tubes Including Friction and Heat Losses. *Computers & Fluids*, 39:1711–1721, 2010.

[51] J. D. Parisse, J. Giordano, P. Perrier, Y. Burtshell, and I. A. Graur. Numerical Investigation of Micro Shock Waves Generation. *Microfluidics and Nanofluidics*, 6(5):699–709, 2009.

[52] G. V. Shoev, Ye. A. Bondar, D. V. Khotyanovsky, A. N. Kudryavtsev, G. Mirsheraki, M. Brouillette, and M. S. Ivanov. Numerical Study of the Shock Wave Propagation in a Micron-Scale Contracting Channel. *27th International Symposium on Shock Waves. AIP Conference Proceedings*, 1333:778–783, 2011.

[53] D. S. Watvisave, U. V. Bhandarkar, and B. P. Puranik. Numerical Investigation of Shock Tube Flow under Rarefied Conditions. *27th International Symposium on Shock Waves. AIP Conference Proceedings*, 1333:372–377, 2011.

[54] A. R. Kumar, H. D. Kim, and T. Setoguchi. Computational Study of Shock Wave Propagation and Reflection in a Micro Shock Tube. *9th International Conference on Heat Transfer, Fluid Mechanics and Thermodynamics*, 2012.

[55] A. R. Kumar and H. D. Kim. Computational Study of the Unsteady Flow Characteristics of a Micro Shock Tube. *Journal of Mechanical Science and Technology*, 27(2):451–459, 2013.

[56] G. Mirsheraki, M. Brouillette, J. Giordano, C. Hebert, J. D. Parisse, and P. Perrier. Shock Waves in Microchannels. *Journal of Fluid Mechanics*, 724:259–283, 2013.

[57] G. Zhang and H. D. Kim. Numerical Simulation of Shock Wave and Contact Surface Propagation in Micro Shock Tubes. *Journal of Mechanical Science and Technology*, 29(4):1689–1696, 2015.

[58] J. M. Austin and D. J. Bodony. Wave Propagation in Gaseous Small-Scale Channel Flows. *Shock Waves*, 21:547–557, 2011.

[59] M. S. Hariharan, S. Janardhanraj, S. Saravanan, and G. Jagadeesh. Diaphragmless Shock Wave Generators for Industrial Applications of Shock Waves. *Shock Waves*, 21:301–306, 2011.

[60] L. Könözsy. The Set of Governing Equations for Viscous Compressible Flows in the Cylindrical Coordinate System. *Manuscript, Fluid Mechanics and Computational Science, Cranfield University*, 2015.

[61] E. B. Arkilic. Measurement of the Mass Flow and Tangential Momentum Accommodation Coeficient in Silicon Micromachined Channels. *Massachusetts Institute of Technology*, 1997.

[62] M. H. Khadem, M. Shams, and S. Hossainpour. Effects of Rarefaction and Compressibility on Fluid Flow at Slip Flow Regime by Direct Simulation of Roughness. *World Academy of Science, Engineering and Technology*, 2(10248), 2008.

[63] Formulario para la Realizacion de Ejercicios de Transferencia de Calor y Masa (in Spanish). *Centre Tecnologic de Transferencia de Calor (CTTC-UPC)*, 2013.

[64] O. Zanotti and G. M. Manca. A Very Short Introduction to the Godunov Methods. *Lecture Notes for the COMPSTAR School on Computational Astrophysics*, 2010.

[65] E. Shapiro and D. Drikakis. Artificial Compressibility, Characteristics-Based Schemes for Variable Density, Incompressible, Multi-Species Flows. Part I. Derivation of Different Formulations and Constant Density Limit. *Journal of Computational Physics*, 210:584–607, 2005.

[66] D. S. Balsara and C.-W. Shu. Monotonicity Preserving Weighted Essential Non-Oscillatory Schemes with Increasingly High Order of Accuracy. *Journal of Computational Physics*, 160:405–452, 2000.

[67] A. Suresh and H. T. Huynh. Accurate Monotonicity Preserving Scheme with Runge-Kutta Time-Stepping. *Journal of Computational Physics*, 136(83), 1997.

[68] L. Könözsy. Non-Linear Diffusive Term in the Three-Dimensional (Cartesian) Rectangular Coordinate System. *Manuscript, Fluid Mechanics and Computational Science, Cranfield University*, 2012.

[69] S. Gottlieb and C.-W. Shu. Total Variation Diminishing Runge-Kutta Schemes. *Mathematics of Computation*, 67(221):73–85, 1998.

[70] S. Gottlieb, C.-W. Shu, and E. Tadmor. Strong Stability-Preserving High-Order Time Discretization Methods. *SIAM Review. Society for Industrial and Applied Mathematics*, 43(1):89–112, 2001.

[71] Nonlinear Conservation Laws -TV Stable Schemes. *Lecture Notes from the Iowa State University, Mathematics Department.*

[72] S. Gottlieb. Strong Stability Preserving Runge-Kutta & Multi-Step Time Discretizations. *SAMSI workshop, University of Massachusetts Dartmouth*, 2007.

[73] L. Könözsy. Multiphysics CFD Modelling of Incompressible Flows at Low and Moderate Reynolds Numbers. *PhD Thesis, Fluid Mechanics and Computational Science, Cranfield University*, 2012.

Appendix A. Additional Mathematical Derivations

A.1 Forwards-Backwards Finite Difference Discretisation of the Navier-Stokes Viscous Terms

Viscous terms of the momentum equations:

$$\frac{\partial \tau_{xx}}{\partial x} = \frac{\partial}{\partial x}\left[2\mu\frac{\partial u}{\partial x} - \frac{2}{3}\mu\left(\frac{\partial u}{\partial x} + \frac{\partial v}{\partial y}\right)\right] = \frac{\partial}{\partial x}\left(\mu\frac{\partial u}{\partial x}\right) - \frac{2}{3}\frac{\partial}{\partial x}\left[\mu\left(\frac{\partial u}{\partial x} + \frac{\partial v}{\partial y}\right)\right] \approx$$

$$\approx 2\frac{\mu_{i+1,j}\frac{u_{i+1,j}-u_{ij}}{\Delta x} - \mu_{i-1,j}\frac{u_{ij}-u_{i-1,j}}{\Delta x}}{\Delta x} - \frac{2}{3}\left[\frac{\mu_{i+1,j}\frac{u_{i+1,j}-u_{ij}}{\Delta x} - \mu_{i-1,j}\frac{u_{ij}-u_{i-1,j}}{\Delta x}}{\Delta x} + \right.$$

$$\left. + \frac{\mu_{i+1,j}\frac{v_{i+1,j+1}-v_{i+1,j}}{\Delta y} - \mu_{i-1,j}\frac{v_{i-1,j}-v_{i-1,j-1}}{\Delta y}}{\Delta x}\right] =$$

$$= \frac{4}{3}\frac{\mu_{i+1,j}\left(u_{i+1,j} - u_{ij}\right) - \mu_{i-1,j}\left(u_{ij} - u_{i-1,j}\right)}{\Delta x^2} -$$

$$- \frac{2}{3}\frac{\mu_{i+1,j}\left(v_{i+1,j+1} - v_{i+1,j}\right) - \mu_{i-1,j}\left(v_{i-1,j} - v_{i-1,j-1}\right)}{\Delta x \Delta y}, \tag{1}$$

$$\frac{\partial \tau_{yx}}{\partial y} = \frac{\partial}{\partial y}\left[\mu\left(\frac{\partial u}{\partial y} + \frac{\partial v}{\partial x}\right)\right] = \frac{\partial}{\partial y}\left(\mu\frac{\partial u}{\partial y}\right) + \frac{\partial}{\partial y}\left(\mu\frac{\partial v}{\partial x}\right) \approx$$

$$\approx \frac{\mu_{i,j+1}\frac{u_{i,j+1}-u_{ij}}{\Delta y} - \mu_{i,j-1}\frac{u_{ij}-u_{i,j-1}}{\Delta y}}{\Delta y} + \frac{\mu_{i,j+1}\frac{v_{i+1,j+1}-v_{i,j+1}}{\Delta x} - \mu_{i,j-1}\frac{v_{i,j-1}-v_{i-1,j-1}}{\Delta x}}{\Delta y} =$$

$$= \frac{\mu_{i,j+1}\left(u_{i,j+1}-u_{ij}\right)-\mu_{i,j-1}\left(u_{ij}-u_{i,j-1}\right)}{\Delta y^2}+$$

$$+\frac{\mu_{i,j+1}\left(v_{i+1,j+1}-v_{i,j+1}\right)-\mu_{i,j-1}\left(v_{i,j-1}-v_{i-1,j-1}\right)}{\Delta x\Delta y}, \tag{2}$$

$$\frac{\partial\tau_{xy}}{\partial x}=\frac{\partial}{\partial x}\left[\mu\left(\frac{\partial u}{\partial y}+\frac{\partial v}{\partial x}\right)\right]=\frac{\partial}{\partial x}\left(\mu\frac{\partial u}{\partial y}\right)+\frac{\partial}{\partial x}\left(\mu\frac{\partial v}{\partial x}\right)\approx$$

$$\approx\frac{\mu_{i+1,j}\frac{u_{i+1,j+1}-u_{i+1,j}}{\Delta y}-\mu_{i-1,j}\frac{u_{i-1,j}-u_{i-1,j-1}}{\Delta y}}{\Delta x}+\frac{\mu_{i+1,j}\frac{v_{i+1,j}-v_{ij}}{\Delta x}-\mu_{i-1,j}\frac{v_{ij}-v_{i-1,j}}{\Delta x}}{\Delta x}=$$

$$=\frac{\mu_{i+1,j}\left(u_{i+1,j+1}-u_{i+1,j}\right)-\mu_{i-1,j}\left(u_{i-1,j}-u_{i-1,j-1}\right)}{\Delta x\Delta y}+$$

$$+\frac{\mu_{i+1,j}\left(v_{i+1,j}-v_{ij}\right)-\mu_{i-1,j}\left(v_{ij}-v_{i-1,j}\right)}{\Delta x^2}, \tag{3}$$

$$\frac{\partial\tau_{yy}}{\partial y}=\frac{\partial}{\partial y}\left[2\mu\frac{\partial v}{\partial y}-\frac{2}{3}\mu\left(\frac{\partial u}{\partial x}+\frac{\partial v}{\partial y}\right)\right]=\frac{\partial}{\partial y}\left(\mu\frac{\partial v}{\partial y}\right)-\frac{2}{3}\frac{\partial}{\partial y}\left[\mu\left(\frac{\partial u}{\partial x}+\frac{\partial v}{\partial y}\right)\right]\approx$$

$$\approx 2\frac{\mu_{i,j+1}\frac{v_{i,j+1}-v_{ij}}{\Delta y}-\mu_{i,j-1}\frac{v_{ij}-v_{i,j-1}}{\Delta y}}{\Delta y}-\frac{2}{3}\left[\frac{\mu_{i,j+1}\frac{u_{i+1,j+1}-u_{i,j+1}}{\Delta x}-\mu_{i,j-1}\frac{u_{i,j-1}-u_{i-1,j-1}}{\Delta x}}{\Delta y}+\right.$$

$$\left.+\frac{\mu_{i,j+1}\frac{v_{i,j+1}-v_{ij}}{\Delta y}-\mu_{i,j-1}\frac{v_{ij}-v_{i,j-1}}{\Delta y}}{\Delta y}\right]=$$

$$=\frac{4}{3}\frac{\mu_{i,j+1}\left(v_{i,j+1}-v_{ij}\right)-\mu_{i,j-1}\left(v_{ij}-v_{i,j-1}\right)}{\Delta y^2}-$$

$$-\frac{2}{3}\frac{\mu_{i,j+1}\left(u_{i+1,j+1}-u_{i,j+1}\right)-\mu_{i,j-1}\left(u_{i,j-1}-u_{i-1,j-1}\right)}{\Delta x\Delta y}. \tag{4}$$

To compute the viscous terms of the energy equation related tot the viscous stress tensor, $\mathbf{u}\cdot\left(\nabla\cdot\underline{\underline{\tau}}\right)$ and $\underline{\underline{\tau}}:\nabla\otimes\mathbf{u}$, only the 1st-order derivative of the velocity field components is required (see eq. [3.21,3.45] and 3.46 respectively). The 2nd-order centred differentiation is written as

$$\frac{\partial u}{\partial x}\approx\frac{u_{i+1,j}-u_{i-1,j}}{2\Delta x}, \tag{5}$$

$$\frac{\partial u}{\partial y} \approx \frac{u_{i,j+1} - u_{i,j-1}}{2\Delta y}, \tag{6}$$

$$\frac{\partial v}{\partial x} \approx \frac{v_{i+1,j} - v_{i-1,j}}{2\Delta x}, \tag{7}$$

$$\frac{\partial v}{\partial y} \approx \frac{v_{i,j+1} - v_{i,j-1}}{2\Delta y}. \tag{8}$$

The dissipation effects associated to the heat transfer by thermal conduction are discretised again using the forwards-backwards differentiation and they can be expressed as

$$\frac{\partial}{\partial x}\left(\kappa \frac{\partial T}{\partial x}\right) \approx \frac{\kappa_{i+1,j}\frac{T_{i+1,j}-T_{ij}}{\Delta x} - \kappa_{i-1,j}\frac{T_{ij}-T_{i-1,j}}{\Delta x}}{\Delta x} = \frac{\kappa_{i+1,j}\left(T_{i+1,j} - T_{ij}\right) - \kappa_{i-1,j}\left(T_{ij} - T_{i-1,j}\right)}{\Delta x^2}, \tag{9}$$

$$\frac{\partial}{\partial y}\left(\kappa \frac{\partial T}{\partial y}\right) \approx \frac{\kappa_{i,j+1}\frac{T_{i,j+1}-T_{ij}}{\Delta y} - \kappa_{i,j-1}\frac{T_{ij}-T_{i,j-1}}{\Delta y}}{\Delta y} = \frac{\kappa_{i,j+1}\left(T_{i,j+1} - T_{ij}\right) - \kappa_{i,j-1}\left(T_{ij} - T_{i,j-1}\right)}{\Delta y^2}. \tag{10}$$

A.2 Computing the $u^R_{i-1/2}$ Value for the MPWENO7 Scheme

To compute the $u^R_{i-1/2}$ value of a MPWENO7 scheme (and any WENO scheme in general), a symmetric procedure is developed and the same equations as described in Section 3.2.2.2 are used. Also, the same smooth indicators as for the $u^L_{i+1/2}$ value apply. Only the optimal weights $C^{(r)}_k$ and the coefficients of the stencil terms $a^{(r)}_{k,n}$ are modified as follows

$$C^{(4)}_0 = \frac{4}{35}, \quad C^{(4)}_1 = \frac{18}{35}, \quad C^{(4)}_2 = \frac{12}{35}, \quad C^{(4)}_3 = \frac{1}{35}. \tag{11}$$

$a^{(4)}_{k,n}$	$n = 1$	$n = 2$	$n = 3$	$n = 4$
$k = 0$	1/12	-5/12	13/12	1/4
$k = 1$	-1/12	7/12	7/12	-1/12
$k = 2$	1/4	13/12	-5/12	1/12
$k = 3$	25/12	-23/12	13/12	-1/4

Table A.1: $a^{(r)}_{k,n}$ coefficients for $r = 4$.